

# Model-independent cosmology with joint observations of gravitational waves and $\gamma$ -ray bursts

Andrea Cozzumbo<sup>1,2</sup>, Ulyana Dupletsa<sup>1,2</sup>, Rodrigo Calderón<sup>3,4</sup>, Riccardo Murgia<sup>5,1</sup>, Gor Oganesyan<sup>1,2</sup>, Marica Branchesi<sup>1,2</sup>

<sup>1</sup>Gran Sasso Science Institute (GSSI), Viale F. Crispi 7, L'Aquila (AQ), I-67100, Italy

<sup>2</sup>INFN - Laboratori Nazionali del Gran Sasso (LNGS), L'Aquila (AQ), I-67100, Italy

<sup>3</sup>Korea Astronomy and Space Science Institute, Daejeon 34055, Korea

<sup>4</sup>CEICO, Institute of Physics of the Czech Academy of Sciences, Na Slovance 1999/2, 182 21, Prague, Czech Republic

<sup>5</sup>Dipartimento di Fisica, Università degli Studi di Cagliari, Cittadella Universitaria, 09042 Monserrato (CA), Italy

E-mail: [andrea.cozzumbo@gssi.it](mailto:andrea.cozzumbo@gssi.it), [ulyana.dupletsa@gssi.it](mailto:ulyana.dupletsa@gssi.it), [calderon@fzu.cz](mailto:calderon@fzu.cz), [riccardo.murgia89@unica.it](mailto:riccardo.murgia89@unica.it)

**Abstract.** Multi-messenger (MM) observations of binary neutron star (BNS) mergers provide a promising approach to trace the distance-redshift relation, crucial for understanding the expansion history of the Universe and, consequently, testing the nature of Dark Energy (DE). While the gravitational wave (GW) signal offers a direct measure of the distance to the source, high-energy observatories can detect the electromagnetic counterpart and drive the optical follow-up providing the redshift of the host galaxy. In this work, we exploit up-to-date catalogs of  $\gamma$ -ray bursts (GRBs) supposedly coming from BNS mergers observed by the Fermi  $\gamma$ -ray Space Telescope and the Neil Gehrels Swift Observatory, to construct a large set of mock MM data. We explore how combinations of current and future generations of GW observatories operating under various underlying cosmological models would be able to detect GW signals from these GRBs. We achieve the reconstruction of the GW parameters by means of a novel prior-informed Fisher matrix approach. We then use these mock data to perform an agnostic reconstruction of the DE phenomenology, thanks to a machine learning method based on forward modeling and Gaussian Processes (GP). Our study highlights the paramount importance of observatories capable of detecting GRBs and identifying their redshift. In the best-case scenario, the GP constraints are 1.5 times more precise than those produced by classical parametrizations of the DE evolution. We show that, in combination with forthcoming cosmological surveys, fewer than 40 GW-GRB detections will enable unprecedented precision on  $H_0$  and  $\Omega_m$ , and accurately reconstruct the DE density evolution.

---

## Contents

<b>1</b>	<b>Introduction</b>	<b>2</b>
<b>2</b>	<b>Data and methods</b>	<b>4</b>
2.1	GRB data selection: redshift measurements	5
2.2	GW parameter reconstruction: luminosity distance estimates	6
2.3	GW detector configurations	8
2.4	Mock MM data with different underlying cosmologies	10
2.5	Non-parametric modeling of DE beyond $\Lambda$	11
<b>3</b>	<b>Cosmological constraints</b>	<b>12</b>
3.1	Comparison between 2G and 3G GW detectors	15
3.2	Comparison among different 3G GW detectors	16
3.3	Model-independent reconstruction of a $\Lambda$ CDM Universe (MOD1)	19
3.4	Model-independent reconstruction of a PEDE Universe (MOD2)	21
3.5	Future prospects	24
<b>4</b>	<b>Summary and conclusions</b>	<b>25</b>
<b>A</b>	<b>Full catalog of merger-driven GRBs with known redshift (circa 2024)</b>	<b>28</b>
<b>B</b>	<b>Full comparison among GW detector configurations</b>	<b>31</b>
<b>C</b>	<b>Further tables and plots</b>	<b>35</b>

---

# 1 Introduction

Current constraints on the late-time expansion history of the Universe mostly come from observations of luminosity distance - redshift  $\{d_L, z\}$ -relation of type Ia Supernovae (SNIa) [1–3] together with measurements of Baryon Acoustic Oscillations (BAO) [4–6]. However, these measurements do not extend above redshift  $z \approx 2$ . Moreover, even within this redshift range, as the value of  $z$  increases, so does the statistical uncertainty, making the distinct impact of many cosmological models, alternative to the  $\Lambda$  Cold Dark Matter ( $\Lambda$ CDM), indistinguishable. Both the BAO and SNIa methods have intrinsic limitations that cannot be completely overcome. Distance measurements from BAO are related to the sound horizon scale,  $r_d = r_s(z_{\text{drag}})$ . This is the maximum distance that acoustic waves could travel in the early Universe before recombination, which today imprinted in the spatial distribution of galaxies. It is only possible to constrain the “shape” of the expansion history  $h(z) = H(z)/H_0$  up to some absolute scaling given by the degenerate combination  $H_0 r_d$ . In other words, we can measure how the expansion rate  $H(z)$  varies with redshift  $z$  but the exact values depend on an uncertain scaling factor, which is the combined product of  $H_0$  and  $r_d$ , making it impossible to determine  $H_0$  or  $r_d$  independently without additional data. This implies that a calibration is needed [7]. Similarly, (uncalibrated) SNIa measurements can only constrain distances up to an additive constant,  $\mathcal{M} = M_B + 5 \log_{10} \left( \frac{c}{H_0} \right) + 25$ <sup>1</sup>. Thus, extracting information on  $H_0$  from either BAO or SNIa requires distances to be calibrated, *i.e.*, the inferred  $H(z)$  and  $\mu(z)$  need to be “anchored” at low redshift [8, 9]. This is usually achieved by imposing an informative prior on the sound horizon  $r_d$  or the absolute magnitude  $M_B$ , or by including external data sets such as Cosmic Microwave Background (CMB), or measurements of the baryon density  $\omega_b = \Omega_b h^2$  from Big-Bang Nucleosynthesis (BBN) [10]. However, the latter approach often assumes a  $\Lambda$ CDM-like expansion history at early times, which could be an obvious source of systematic in case the latter is not the model that better describes our Universe [11].

Recently, thanks to the discovery of gravitational waves (GWs) [12] from the merger of binary compact objects, we have access to an alternative, self-calibrated<sup>2</sup> way to measure luminosity distances [13]. Although GWs qualify as standard rulers, they do not provide any direct redshift measurement, which has to be inferred relying either on the identification of the host galaxy [14, 15] or on statistical methods [16, 17]. There are, in fact, two primary methods to exploit GW data for cosmological inference: one involves the presence of the electromagnetic counterpart of the gravitational event (bright sirens), and the other does not (dark sirens). An example of the first category is the GW signals from binary neutron star (BNS) mergers, which, when jointly detected with their electromagnetic counterpart, provide an independent and self-calibrated tool to trace the late-time Universe expansion history [18]. In the second case, such as with binary black hole (BBH) mergers, cosmological information can still be obtained by using various statistical methods, referred to the BBH population, to estimate the redshift of the events [19–40].

Another intriguing opportunity lies in exploring alternative classes of standard sirens such as, for instance, mergers of binary white dwarfs [41] and supermassive black hole binaries [42]. The prospects for accessing cosmological parameters using different classes of GW sources will be dramatically improved by the advent of new and innovative observato-

---

<sup>1</sup>Taking the distance modulus  $\mu(z) \equiv m_B(z) - M_B$ , one gets  $m_B(z) = 5 \log_{10} \left( \frac{d_L(z)}{\text{Mpc}} \right) + 25 + M_B = 5 \log_{10} \left( \frac{H_0}{c} d_L(z) \right) + \mathcal{M}$ , having defined  $\mathcal{M} \equiv M_B + 5 \log_{10} \left( \frac{c}{H_0} \right) + 25$

<sup>2</sup>Luminosity distance measurements from GWs can also be affected by systematics, for instance due to the waveform modeling. However, they are completely negligible in the context of this work.

ries, such as the next generation of ground-based GW observatories [43], Einstein Telescope (ET) [44] and Cosmic Explorer (CE) [45], as well as moon- and space- based observatories probing the deci-, milli-, and nano-Hertz bands, such as the Lunar Gravitational Wave Antenna (LGWA) [46, 47], the Laser Interferometer Space Antenna (LISA) [48] and the Pulsar Timing Array facilities [49, 50].

In this work we focus on the bright siren science case, exploring both current and future GW detector capabilities. The joint detection of GW170817 [14], with its associated EM emission [51–53], enabled us to determine the current expansion rate of the Universe (although still with a large level of uncertainty). This was done by measuring the luminosity distance to the source from the GW signal and the redshift from the host galaxy observations. The almost simultaneous detection of the GRB170817A by *Fermi*-GBM after the coalescence provided the first direct evidence that BNS mergers are progenitors of short GRBs [54]. In addition, GW170817 taught us that GRBs can occur simultaneously with a kilonova (KN) emission. KNs are considered to be the furnaces of heavy nuclei, produced by rapid neutron capture. The peculiar features of the light-curve of the KN isotropic optical emission is a sign of the presence of such processes.

GRBs are usually classified according to their  $T_{90}$ , that is the time at which we measure 90% of the incoming signal. Short GRBs ( $T_{90} \lesssim 2$  s) are associated to BNS mergers [55–57], while long GRBs ( $T_{90} \gtrsim 2$  s) are associated to the collapse of massive stars [58, 59]. However, observations have been recently pointed out that such a standard assumption may result in an oversimplified classification [60–65]. That is why, in this work, we base our analyses on those GRBs (either short or long) that are most likely driven by a BNS merger [66]. Operating in synergy with electromagnetic observatories, the next generation GW observatories like ET are expected to detect GW signals associated to almost each observed  $\gamma$ -ray burst (GRB) produced by a BNS merger up to  $z \approx 3$  [44, 67]. These multi-messenger (MM) events will provide a valuable method that will complement existing and upcoming constraints from other cosmological probes. In addition, several electromagnetic surveys, such as the Dark Energy Spectroscopic Instrument (DESI) [68], Euclid [69] and the James Webb Space Telescope [70], in the optical band, and the Square Kilometer Array Observatory (SKAO) [71], in the radio band, will further provide data of unprecedented precision. Given the improved sensitivity, as well as the complementarity of scale and redshift regimes probed with respect to currently available data, establishing efficient synergies among GW and EM observations represents an important frontier for cosmology [44, 72].

Over the years, a plethora of alternative theoretical models have been proposed to provide a more comprehensive fit to current cosmological data than the standard  $\Lambda$ CDM scenario [73–79]. In fact, despite the remarkable success of the latter, the persistence of cosmic tensions seems to hint at an inconsistency between some of the cosmological parameters inferred from early Universe observations, and late-time astrophysical data [7, 11]. However, given the excellent fit to Cosmic Microwave Background (CMB) data provided by the  $\Lambda$ CDM model, any alternative scenario should only induce limited departures in order to improve the fit to post-recombination data without spoiling the CMB predictions. It is thus essential to develop agnostic methods covering the phenomenology induced by broad classes of theoretical models. In this work we exploit a model-independent, non-parametric, data-driven approach based on Machine Learning (ML) techniques [80]. Aiming at covering any model inducing deviations from the  $\Lambda$ CDM expansion history still allowed by current data – yet expected to leave a distinct imprint in forthcoming observations – we devised a new pipeline, interfaced with the widely used numerical Einstein-Boltzmann solver CLASS [81, 82]. We stick to General

Relativity (GR) in the present work, but the same method is also suitable to test modified gravity (MG) theories [83]. We leave this task for future work.

To generate the mock MM data needed for inferring the expansion history, we make use of the most updated catalogs of GRBs from BNS mergers, as measured by currently operating high-energy satellites (*Fermi*-GBM and *Swift*-BAT/XRT). We assume that ET, as well as other combinations of both current (dubbed 2G) and future (3G) GW interferometers, was operating simultaneously to catch the corresponding GW counterparts. We leave for a follow-up work a joint analysis with future high-energy satellites [67, 84].

We generate our data sets assuming two cosmologies, both of which are in very good agreement with current observations. The accuracy of the  $d_L$  estimate is governed by the GW detector networks that we employ. We then make use this mock MM data in two steps. To begin with, we perform a MCMC analysis on the data to estimate the cosmological parameters in a model-dependent manner, *i.e.*, by assuming a parametric model for the dark energy (DE) sector. Finally, we adopt a model-independent approach to reconstruct the DE phenomenology without assuming any specific parametric form for its Equation of State (EoS). As a promising alternative to the standard  $\Lambda$ CDM concordance model, to generate the mock data, we focus on the so-called Phenomenological Emergent Dark Energy (PEDE) [85, 86] scenario. This model features the same number of free parameters as  $\Lambda$ CDM but predicts an emergent component of DE in the late Universe. Such a phenomenology has recently garnered significant interest following the first data release by the DESI collaboration [87, 88]. We compare the theoretical predictions of the  $\{d_L, z\}$ -relation, generated using a modified version of CLASS, with the previously described mock data. This enhanced version of CLASS allows us to implement non-standard cosmologies and apply Gaussian Process (GP) evolution to model DE phenomenology [80].

Upon publication of this paper, the devised software will be publicly released, as a `python`-based likelihood for the publicly available MCMC samplers for cosmological inference `MontePython` [89, 90] and `cobaya` [91]. Our likelihood can be used in joint analyses with all main complementary cosmological probes. Alongside with this likelihood we will make public all the data catalogs used in this paper.

This paper is structured as follows: in Section 2 we present the data sets and methods used to produce the joint GRB-GW mock data. We also explain the rationale behind using both parametric and non-parametric approaches for cosmological inference. In Section 3 we present the cosmological constraints obtained with the two approaches and we discuss the analyses performed with future GW and BAO surveys. Section 4 provides summary and conclusions.

## 2 Data and methods

As outlined in the Introduction, our study follows a three-step procedure: *(i)* the selection of the most up-to-date catalogs of GRBs from BNS mergers from almost 20 years of observations by ongoing high-energy surveys, *i.e.*, from *Fermi*-GBM and *Swift*-BAT/XRT (Subsection 2.1); *(ii)* the production of a set of mock MM data by injecting a GW signal per each GRB and the reconstruction of their parameters by means of a prior-informed Fisher matrix analysis [92], assuming different combination of current and future generation of GW detectors, under various underlying cosmologies (Subsection 2.2); *(iii)* the use of the mock data to perform a model-dependent inference of the cosmological constraints and, finally, an agnos-

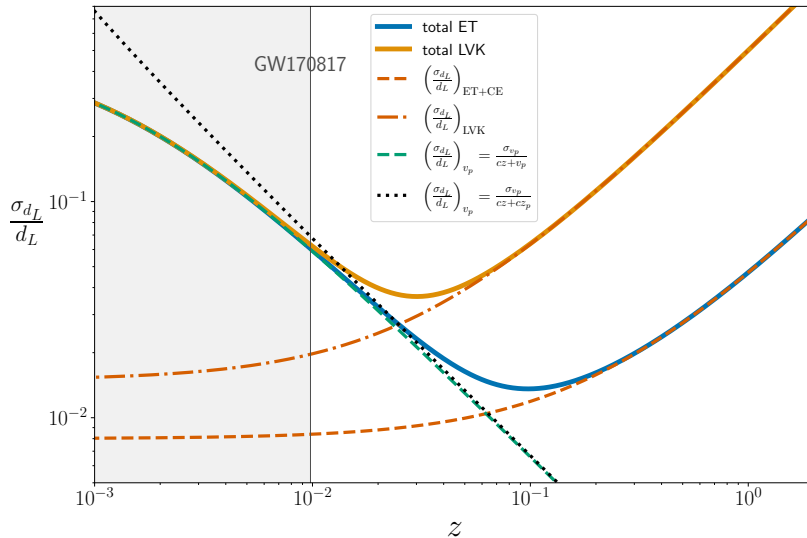


**Figure 1.** Impact of the peculiar velocity on the  $d_L$  relative uncertainty. The orange curves show the LVK (dashed-dotted) and ET $\Delta$ +CE (dashed) relative uncertainty. They are obtained by fitting the estimated uncertainty (without correcting for  $v_p$ ) with a power-law [95, 96]. The green dashed curve is the peculiar velocity contribution to the  $d_L$  uncertainty for  $v_p = 400 \text{ km s}^{-1}$  and  $\sigma_{v_p} = 200 \text{ km s}^{-1}$ . The more precise is the estimation on  $d_L$  given by the GW detectors, the more the peculiar velocity contribution is important. The dotted black curve shows the peculiar velocity contribution computed adopting the prescription of Ref. [97]. The vertical line is the corresponds to the redshift of GW170817.

tic, model-independent reconstruction of the DE phenomenology, thanks to GP techniques (Subsection 2.4 and 2.5).

## 2.1 GRB data selection: redshift measurements

The starting point of this work is an extensive analysis of the most updated catalogs of GRB data collected by *Fermi*-GBM and *Swift*-BAT/XRT from 2005 to 2023. The catalog is presented in Appendix A (Table 2), alongside with further details on the selection procedure. The aim is to identify all events – associated to a BNS merger with high probability – whose host galaxy has a redshift determined with less than 10% uncertainty. To begin with, we focused on well-localized (XRT radius  $\leq 5''$ ) short GRBs ( $T_{90} \lesssim 2 \text{ s}$ ) [66]. Following Ref. [66], we also considered as merger-driven GRBs those events with  $T_{90} \gg 2 \text{ s}$  due to their extended emission<sup>3</sup>. In addition, we included to the resulting catalog of merger-driven GRBs, the event GRB230307A, as it has been associated to a KN explosion [93], as well as the event GRB191019A and GRB211211A, interpreted as compact object mergers [60, 61, 94]. For each event we took into account its probability to be associated to the actual host galaxy, by accounting for the probability of chance coincidence,  $P_{cc}$ , as evaluated in Ref. [66]. The full catalog of GRB events that we have considered for our analyses, classified according the their  $P_{cc}$ , is reported in Appendix A. Hereafter, we refer to a *fiducial* catalog (containing only those events with  $P_{cc} \leq 0.02$ ), an *extended* catalog (events with  $P_{cc} \leq 0.10$ ), and a *very extended* catalog ( $P_{cc} \leq 0.20$ ).

<sup>3</sup>the extended emission in a GRB refers to a prolonged phase of lower-intensity  $\gamma$ -ray radiation that follows the initial, intense burst of energy, lasting from seconds to several minutes.

One key difference compared to previous works is that our results do not depend on BNS population synthesis simulations [44, 67, 72, 98–100] as our GW parameter estimation code is based on actually *observed* GRB data. Typically, the BNS merger rate density as a function of redshift of synthetic populations depends on assumptions about common envelope, core-collapse SN model, star formation and metallicity evolution [101]. In contrast, our approach provides a realistic redshift distribution of BNS mergers because it relies directly on observed data. This is particularly important because our data actually trace the redshift distribution of BNS, which plays a key role in constraining the evolution of DE.

It is crucial to emphasize that predicting the rate of well-localized events or those with a known redshift in MM observations is highly challenging, due to numerous uncertainties related to the instruments and the observational strategies. For this reason, we have chosen to base our work on the two decades of experience from *Swift* and *Fermi*. We can reasonably consider the results presented in this work as a lower bound of the constraining power from GRB-GW data provided by future high energy surveys [102].

## 2.2 GW parameter reconstruction: luminosity distance estimates

We used the BNS merger-driven GRB catalog presented in Subsection 2.1 to produce fast and accurate forecasts on the detection capabilities of their GW counterpart, assuming different observational configurations, by means of the GW detector simulation code **GWFish** [103]. **GWFish** is capable to perform parameter estimation for an individual GW event in a few seconds. However, this comes at the cost of approximating the likelihood  $\mathcal{L}(d|\theta)$  with a multivariate normal distribution, *i.e.* the Fisher matrix

$$\mathcal{F}_{ij} = \mathcal{C}_{ij}^{-1} = - \left\langle \frac{\partial}{\partial_i \partial_j} \ln \mathcal{L}(d|\theta) \right\rangle \Bigg|_{\theta=\theta_{\text{inj}}} = \left( \frac{\partial h}{\partial \theta_i} \Big| \frac{\partial h}{\partial \theta_j} \right) \equiv 4\Re \int_0^\infty df \frac{1}{S_n(f)} \frac{\partial h}{\partial \theta_i} \frac{\partial h^*}{\partial \theta_j}, \quad (2.1)$$

where the data stream is defined as  $d(t) = h(t) + n(t)$ ,  $h(t)$  is the GW signal,  $\theta$  is an array containing all the GW signal parameters,  $\theta_{\text{inj}}$  are the fiducial injected values,  $\mathcal{F}_{ij}$  is the Fisher information matrix, that is the inverse of the covariance matrix  $\mathcal{C}_{ij}$ . The average in the above expression of Eq. (2.1) is taken over all the noise realizations. The function  $S_n(f)$  is the detector power spectral density (PSD), encoding the sensitivity of the detector configuration. In our treatment we use the IMRPhenomHM waveform approximant [104]. The full set of GW parameters is  $\theta = \{m_1, m_2, d_L, \alpha, \delta, \iota, \psi, t_c, \Phi_c\}$  where  $m_1$  and  $m_2$  are the detector frame masses of the two compact objects,  $d_L$  is the luminosity distance to the merger event,  $\alpha$  and  $\delta$  are the right ascension (R.A.) and declination (dec.) angles,  $\iota$  is the inclination angle between the line of sight vector and the orbital angular momentum of the binary,  $\psi$  is the polarization angle,  $t_c$  and  $\Phi_c$  are the time and phase at coalescence, respectively.

In the analyses presented in this paper, the sky localization of the event ( $\alpha, \delta$ ) and the time of coalescence  $\Phi_c$  are fixed, as they are given by the GRB detection. The redshift  $z$  is fixed too, as it is given by the host galaxy association (see Subsection 2.1). The values of the masses and polarization angle are drawn from the following uniform intervals:  $m_1, m_2 \in [1.1, 2.1] M_\odot$ ;  $\psi \in [0, 2\pi]$  [105, 106]. The viewing angle  $\iota$  is generated uniform in cosine in the range  $\iota \in [0, 5/180\pi] \cup [175/180\pi, \pi]$ . The luminosity distance is set by Eq. (3.1) once the redshift and the cosmology are chosen. We have verified that our results are almost insensitive to the NS mass distribution, be it Gaussian, uniform or considering BNS systems characterised by high and low total mass or mass ratio. In Appendix C, Figure 31 we show the comparison between Gaussian and uniform mass sampling.

As already discussed, for the purposes of this work we are mostly interested in the uncertainties on the luminosity distance  $d_L$ . The standard Fisher matrix approach provides the uncertainties as the square root of the corresponding diagonal elements of the covariance matrix. Here we adopt an improved, novel approach capable to provide prior-informed Fisher matrix reconstruction of  $d_L$  and the other GW parameters [92].

The procedure we use to produce mock data can be summarized as follows. Initially, we obtain a Gaussian posterior as output of `GWFish` analysis. We sample from this distribution by first imposing truncation based on the physical bounds [92]. This ensures a faster sampling process by preventing the generation of numerous samples with null priors that would need to be discarded. For instance, we avoid negative values of  $d_L$  that do not have any physical meaning. Finally, we sample again from this truncated multivariate Gaussian and for each realization of this likelihood we evaluate the prior probability. Therefore, for each event, we finally obtain a prior-informed probability density of the  $d_L$ , among all the GW parameters.

We now describe how we take into account the main potential sources of uncertainty on  $d_L$  estimation from GW signals, besides the systematic uncertainties associated to the GW measurement [107]. The first source of uncertainty that we address for what concerns the association to the host galaxy is the treatment of its peculiar velocity  $v_p$  [108, 109]. For nearby events the peculiar velocity correction to the pure Hubble flow contribution can be dominant. This accounts for the peculiar motion of the host galaxy with respect to the observer and it is mainly induced by the large-scale matter distribution, whereas in the relatively close Universe, the peculiar velocities are dominated by nearby galaxies. We provide further details on the comparison between accounting or not this correction in Appendix C. The peculiar velocity contributes to the overall uncertainty on  $d_L$  as follows:

$$\frac{\sigma_{d_L}}{d_L} = \sqrt{\left(\frac{\sigma_{d_L}}{d_L}\right)_{v_p}^2 + \left(\frac{\sigma_{d_L}}{d_L}\right)_{\text{GW}}^2} \quad (2.2)$$

where the label GW refers to the uncertainty given by the interferometer network parameter estimation. The other component, due to  $v_p$ , can be expressed as  $\sigma_{d_L} = d_L \sigma_{v_p} / (cz + v_p)$ . This treatment can be further refined according to the guidelines provided in Ref. [97]. Note that with this expression, we are performing a Gaussian approximation of the GW  $d_L$  posteriors. This procedure is useful for illustrating the relative contribution of the two uncertainties. However, in the mock data set presented later, this is done in a more refined manner. In Figure 1 we show the relative impact of the two contributions for the case of LVK(O5) and ET $\Delta$ +CE (see Subsection 2.3 for the description of the adopted detector configurations). We notice that the more constraining is the GW detector, the more important becomes the peculiar velocity contribution. The green dashed line represents the peculiar velocity uncertainty estimation used in this work. For events at redshifts higher than the closest event in our dataset (i.e., GW170817), we do not observe any significant differences between the peculiar velocity treatment from Ref. [97] (black dotted line) and the other, less refined approach. From the considerations made using Figure 1, we can safely assume the peculiar velocity contribution to be relevant only for  $z \leq 0.15$  (see Figure 30 in Appendix C for the choice of this value). For events falling into this category, we account for this source of uncertainty by generating random Gaussian-distributed values of  $v_p$  and  $\sigma_{v_p}$ .

The last source of uncertainty that we considered is the GW weak lensing noise, that we parameterize as in Refs. [24, 110, 111]. This phenomenon is particularly important at high redshift, due to the larger distance travelled by the signal. We evaluated that the effect is



subdominant for all the events, even in our most constraining configuration, thus we will not report any corrections due to weak lensing.

The posterior distribution of the luminosity distance is thus characterized either by the GW contribution alone coming from the Fisher analysis or by a combination of both GW and peculiar velocity contributions at  $z \leq 0.15$ . The GW posterior is interpolated with a Kernel Density Estimator (KDE), allowing to capture all the non-Gaussian features of the distribution. The result of this process serves as the input for our newly devised likelihood for cosmological inference. Within the likelihood, if the event falls below the redshift limit for the peculiar velocity correction, we convolve the input KDE with the Gaussian distribution of the  $d_L$  uncertainty due to peculiar velocity. The resulting probability density is then fit again using a KDE interpolation.

We want to stress that the pipeline we developed is versatile enough to accommodate any  $d_L$  posterior distributions from any distance tracer. In our work we relied on the Fisher matrix approximation for the GW  $d_L$  posterior as presently a Bayesian analysis tool, capable of processing BNS signals with the future GW detectors, is still in the developing process<sup>4</sup>.

### 2.3 GW detector configurations

In what follows we describe the GW detector configurations used in our analyses:

- LVK stands for the LIGO Hanford, LIGO Livingston, Virgo, KAGRA network [113–115]. For the LVK network we use both the so-called O5 (more optimistic) PSDs [116] and the A<sup>#</sup> one [117]. The A<sup>#</sup> refers to the potential upgrade of LIGO following the O5 data collection run. In the latter, we are adding to the network the LIGO India detector (LVKI). The A<sup>#</sup> PSD is used for the LIGO detectors (Hanford, Livingston and India) alone. Virgo and KAGRA are using O5 sensitivity in both configurations.
- ET $\Delta$  is the Einstein Telescope baseline configuration, corresponding to three nested detectors with arm length and aperture of, 10 km and 60°, respectively. Each of them is composed according to the so-called xylophone concept, *i.e.*, by two different co-located interferometers: one optimized for the low frequency (LF) and one for the high frequency (HF). We dub ET HF  $\Delta$  a configuration where the cryogenic LF detector is not included [44]. The location of the detector is assumed to be at the ET Sardinian candidate site (Sos Enathos mine).
- ET2L is a xylophone configuration with 15 km arm length, and aperture of 90°. We use the 45° misaligned configuration. It corresponds to two separated detectors, one in the Sardinian site, and one in the Meuse-Rhine candidate site (Netherlands). As in the ET $\Delta$  case, we dub as ET HF 2L a configuration where the cryogenic LF detector is not included [44].
- ET X + CE configuration, with  $X \in \{\Delta, 2L\}$ , that refers to a detector network composed of the ET X and the Cosmic Explorer (CE). We consider a single CE detector positioned in the LIGO Hanford site, with an arm aperture of 90° and a 40 km arm length<sup>5</sup>.

---

<sup>4</sup>One major issue in analysing the BNS signals comes from their long duration in 3G detectors band ( $\sim$  hours). This implies a high computational cost, on top of the fact that it requires to consider the effects of Earth rotation. In `GWFish` these effects are implemented while they are not present in currently used GW Bayesian analysis software, such as `bilby` [112].

<sup>5</sup>The PSD of CE can be found [here](#).

**Table 1.** Summary of the number of events observed by all GW detector configurations considered in this work. From left to right we report the detector configuration, the fiducial catalog (containing 38 GRB events), the extended catalog (containing 54 GRB events) and the very extended catalog (containing 61 GRB events). For each configuration we also report the redshift of the furthest event detected. The detection threshold is set to  $\text{SNR} \geq 8$ . The results listed in this table are the same for both the mock data catalogs that we have produced, assuming as underlying cosmology either  $\Lambda\text{CDM}$  (MOD1) or PEDE (MOD2). See the main text for further details.

Detector	Fiducial (38 ev.)		Extended (54 ev.)		Very extended (61 ev.)	
	$z_{\text{max}}$	N. events	$z_{\text{max}}$	N. events	$z_{\text{max}}$	N. events
LVK (O5)	0.248	8	0.248	10	0.248	10
LVKI A <sup>#</sup>	0.46	16	0.46	20	0.46	21
ET HF $\Delta$	1.370	30	1.465	40	1.465	43
ET $\Delta$	1.754	36	2.58	48	2.58	55
ET $\Delta$ +CE	2.609	38	2.609	53	2.609	60
ET HF 2L	1.754	36	2.58	48	2.58	54
ET2L	1.754	37	2.58	50	2.58	57
ET2L + CE	2.609	38	2.609	53	2.609	60

In Table 1 we report the number of detected joint GRB-GW events for each GRB catalog (fiducial, extended, and very extended) by all the detector configurations that we have considered. These numbers are valid for both the underlying cosmologies that we have analyzed. We adopt a detection threshold of  $\text{SNR} \geq 8$  as in Ref. [44]. From Table 1 one can easily extract useful information to understand what will be presented in Section 3. One can notice that combining more than one 3G detector in a network sensibly improves the number of detections, allowing to catch the GW counterpart of practically all injected events, even the ones at the highest redshift (see also Appendix B). Note also that the duty cycle influences the number of detected events<sup>6</sup>, while the detector sensitivity (*i.e.*, the PSD) primarily affects the uncertainty in GW parameter estimation, impacting the cosmological constraints (see Section 3). Finally, we stress how properly accounting for the impact of peculiar velocities at low redshift, even at the level of a single event, significantly improves the accuracy on the inferred cosmological parameters. Having a network of N detectors increases the number of detectable events (compared to having N-1 detectors) thanks to the combined duty cycles. However, the quality of the  $d_L$  posterior provided by improved detector sensitivities is more critical for an accurate cosmological analysis than the sheer number of events. This is well demonstrated by the LVK configuration, which includes three detectors. While this setup offers a more favorable duty cycle, it lacks sufficient sensitivity. Consequently, as we will discuss in Section 3, the LVK configuration provides very weak cosmological constraints.

---

<sup>6</sup>In all our analyses we set the duty cycle of the GW detectors to 85%. The number of missed events decreases when combining more detectors, because it is statistically more probable that they are active together.

## 2.4 Mock MM data with different underlying cosmologies

Assuming an isotropic and homogeneous Universe described by a flat FLRW metric, the first Friedmann equation reads

$$\frac{H^2(z)}{H_0^2} = \Omega_{m,0}(1+z)^3 + \Omega_{r,0}(1+z)^4 + (1 - \Omega_{m,0} - \Omega_{r,0}) f_{\text{DE}}(z) , \quad (2.3)$$

where  $\Omega_i = 8\pi G\rho_i/3H_0^2 = \rho_i/\rho_{0,\text{cr}}$  is the fractional energy density of the  $i$ -th component, the subscript “0” denotes its present value (at  $z = 0$ ) and  $\rho_{0,\text{cr}}$  is the critical energy density today. Under the flatness condition, we can define  $\Omega_{\text{DE},0} = 1 - \Omega_{m,0} - \Omega_{r,0}$  and consequently

$$f_{\text{DE}}(z) = \rho_{\text{DE}}(z)/\rho_{\text{DE},0} . \quad (2.4)$$

The quantity  $f_{\text{DE}}(z)$  defines the redshift evolution of the DE. From the conservation of the stress-energy tensor  $f_{\text{DE}}$  can be expressed as an integral of the DE Equation of State (EoS)  $w(z) \equiv p_{\text{DE}}/\rho_{\text{DE}}c^2$ , namely:

$$f_{\text{DE}}(z) = \exp \left\{ 3 \int_0^z \frac{1+w(z')}{1+z'} dz' \right\} = \exp \left\{ 3 \int_0^z [1+w(z')] d \ln(1+z') \right\} . \quad (2.5)$$

Within the standard  $\Lambda$ CDM model, DE is assumed to be a cosmological constant, *i.e.*  $w(z) = -1$ , that leads to  $f_{\text{DE}} = 1$ . Note that  $f_{\text{DE}}(z)$  is an *effective* quantity capable of capturing in a model-independent fashion a wide variety of alternatives to a cosmological constant behaviour in Eq. (2.3), such as time-evolving DE, the effective energy density of modified gravity, or any additional degree of freedom contributing to the expansion that does not evolve over time in the same way as matter. Taking the logarithm and differentiating both sides of Eq. (2.5) we find the expression for the *effective* EoS parameter

$$w(z) = \frac{1}{3}(1+z) \frac{d \ln f_{\text{DE}}(z)}{dz} - 1 . \quad (2.6)$$

In this work, we consider a simple beyond- $\Lambda$ CDM model, the PEDE model, where DE has no effective presence in the past ( $z \gtrsim 2$ ) and it phenomenologically emerges at the late times [85, 86]. The PEDE model has zero extra-degrees of freedom compared to the standard  $\Lambda$ CDM model. Within PEDE, the redshift evolution of the DE EoS (Eq. 2.6) is given by

$$w^{\text{PEDE}}(z) = -\frac{1}{3 \ln(10)} (1 + \tanh\{\log_{10}(1+z)\}) - 1 , \quad (2.7)$$

which, using Eq. (2.5), becomes

$$f_{\text{DE}}(z) = 1 - \tanh\{\log_{10}(1+z)\} . \quad (2.8)$$

For the purposes of this work, we generated several sets of mock MM data corresponding to various GW detector configurations, assuming two different cosmological scenarios:

- the first model (MOD1) assumes  $\Lambda$ CDM as underlying cosmology with background parameters set to the default CLASS values [82], *i.e.*,  $\theta_c^{\Lambda\text{CDM}} = \{H_0 = 67.81 \text{ km Mpc}^{-1}\text{s}^{-1}, \Omega_m = 0.309\}$ .

- the second model (MOD2) assumes an underlying PEDE cosmology with the best-fit cosmological parameters to *Planck*2018+eBOSS+Pantheon+ data [10, 118, 119], namely  $\theta_c^{\text{PEDE}} = \{H_0 = 70.3 \text{ km Mpc}^{-1}\text{s}^{-1}, \Omega_m = 0.295\}$ .

Note that both MOD1 and MOD2 are best-fit models to the same data sets, despite the underlying DE models being significantly different. This represents the most extreme case of degeneracy in light of current data. In light of the recent DESI results [87, 88, 120], which points toward a late-time emergent DE, a PEDE-like model could in principle rule out the cosmological constant hypothesis with decisive statistical significance.

## 2.5 Non-parametric modeling of DE beyond $\Lambda$

GP regression has been extensively used in the literature to reconstruct smooth functions from noisy data, without the need to assume a parametric form [*e.g.* 121–128, for a non-exhaustive list] (see also [99, 129–133] for some applications in the context of GW cosmology). In this work, following Refs. [80, 83] we reconstruct the time-evolution of  $f_{\text{DE}}(z)$  through GPs, by modelling it as follows:

$$f_{\text{DE}}(z) \sim \mathcal{GP}(\bar{f}(z) = 1, K = k(\sigma_f, \ell_f)) , \quad (2.9)$$

where  $\bar{f}(z)$  is the mean function of a multivariate Gaussian distribution and  $K$  is the covariance function between two points  $k(x_i, x_j)$ , known as a *kernel* in the GP literature [134]. We choose to work with a squared-exponential kernel of the form

$$k(x_i, x_j; \sigma_f, \ell_f) = \sigma_f^2 \exp\left(-\frac{(x_i - x_j)^2}{2\ell_f^2}\right) , \quad (2.10)$$

where  $\sigma_f$  and  $\ell_f$  are hyperparameters determining the amplitude of the deviations from the mean function  $\bar{f}$  and the typical correlation length, respectively. As discussed in Refs. [83, 125, 128], the posterior distributions of the hyperparameters  $\sigma_f$  and  $\ell_f$  carry valuable information on the mean function at hand (a cosmological constant,  $\Lambda$ , in this case). While we do not delve into the details of GP regression in this work<sup>7</sup>, we briefly discuss the differences between our approach and conventional analyses (see [127] for a thorough comparison). A key quantity in GP regression is the log-marginal likelihood (LML), given by

$$\ln \mathcal{L} = -\frac{1}{2}[\mathbf{r}^T \mathbf{K}^{-1} \mathbf{r} + \ln |\mathbf{K}| + N \ln(2\pi)] , \quad (2.11)$$

where  $\mathbf{r} = \mathbf{y} - \mathbf{y}^{\text{data}}$  is the residual vector,  $\mathbf{\Sigma}$  is the data covariance and  $\mathbf{K} = \mathbf{\Sigma} + k(\sigma_f, \ell_f)$  is the full covariance. Unlike conventional GP approaches, which rely on the optimization of the hyperparameters such that the LML in Eq. (2.11) is maximized, we instead do *forward-modeling* and draw a sample of  $f_{\text{DE}}$  from Eq. (2.9) at each point in parameter space  $(\Omega_m, H_0, \sigma_f, \ell_f)$  and compute the likelihood of the data. This effectively allows us to marginalize over the space of realizations numerically<sup>8</sup> and obtain posterior distributions on  $f_{\text{DE}}(z)$  in a non-parametric manner. While this approach can be computationally time-consuming, it allows us to consistently combine different probes (such as SNIa and GW distance measurements) and break the degeneracies between different cosmological parameters.

<sup>7</sup>We refer the reader to the usual reference [134] and [80, 83, 127] for more details on the GP method.

<sup>8</sup>This “forward modeling” approach has been shown to be equivalent to the conventional (posterior) GPR method in [127].

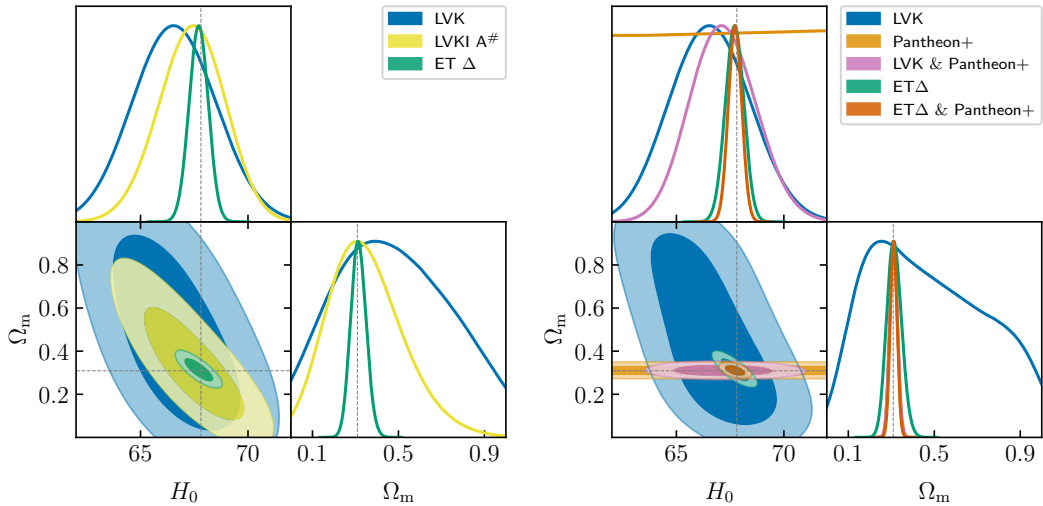


**Figure 2.**  $\Lambda$ CDM constraints (1- and 2- $\sigma$  C.L.) on  $H_0$  and  $\Omega_m$  obtained by fitting an underlying  $\Lambda$ CDM cosmology (MOD1). (*Left*) Comparison between LVK (O5) (blue) with 8 events, LVKI A# (yellow) with 16 events and ET $\Delta$  (green) with 36 events. (*Right*) LVK (O5) and ET $\Delta$  as in the left panel. We over-plot the constraints obtained with the Pantheon+ data set alone (orange) and in a joint analysis with LVK (O5) (pink) and ET $\Delta$  (dark orange). Dashed lines refer to the injected cosmology used to produce the mock GRB-GW data.

### 3 Cosmological constraints

In this Section we will present the constraints on the two cosmological scenarios described in Subsection 2.4 – MOD1 ( $\Lambda$ CDM) and MOD2 (PEDE) – obtained by means of extensive MCMC analyses with the `MontePython-v3`<sup>9</sup> sampler [89, 90] in its default Metropolis-Hastings mode and `Cobaya`<sup>10</sup> [91], interfaced with a modified version of `CLASS` [80, 82].

In both our  $\Lambda$ CDM and PEDE analyses we scan the parameter space defined by the standard set of two background parameters, namely the CDM abundance  $\Omega_{\text{cdm}}$ , and the Hubble parameter  $H_0$ . We fix the remaining ones – the baryon abundance  $\Omega_b$ , the tilt and amplitude of the primordial power spectrum ( $n_s$ ,  $A_s$ ) and the optical depth at reionization  $\tau_{\text{reio}}$  – to the best fit values from *Planck*2018 [10]. In addition, we perform a series of MCMC analyses exploring the Chevallier-Polarski-Linder (CPL) parameterization of the DE EoS [135, 136], *i.e.*,  $w(a) = w_0 + w_a(1 - a)$ , where  $w_0$  and  $w_a$  are the two extra free parameters with respect to  $\Lambda$ CDM and PEDE. Finally, we scan the parameter space defined in Subsection 2.5, where the DE sector is described in a model-independent fashion by the two GP hyperparameters  $\sigma_f$  and  $\ell_f$ . We have adopted the following uniform priors:  $H_0 \in [50, 90]$  km s<sup>-1</sup> Mpc<sup>-1</sup>,  $\Omega_m \in [0, 1]$ ,  $w_0 \in [-2, 0]$ ,  $w_a \in [-5, 2]$ ,  $\sigma_f \in [10^{-4}, 5]$ ,  $\ell_f \in [10^{-2}, 10]$ . As the results presented here are based on the specific priors used in our analyses, note that – in some of our GW-only analyses – the parameter  $w_a$  reaches the lower bound of its prior range. We verified that expanding the prior ranges weakens the constraints on the CPL parameters. However, this also opens up the  $H_0$ - $\Omega_m$  parameter space in a region that is entirely ruled out by external data such as SNIa data from Pantheon+ . This ensures that all our conclusions

<sup>9</sup>[https://github.com/brinckmann/montepython\\_public](https://github.com/brinckmann/montepython_public)

<sup>10</sup><https://github.com/CobayaSampler/cobaya>

are prior-independent. Our prior choice on  $w_0$  and  $w_a$  is in fact more conservative compared to that adopted by the DESI collaboration [87].

The relation between each set of free cosmological parameters  $\theta_c$  and the luminosity distance is given by

$$d_L(z, \theta_c) = c (1 + z) \int_0^z \frac{dz'}{H(z, \theta_c)} \quad (3.1)$$

Through our MCMC analyses we minimize a likelihood  $\mathcal{L}(d|\theta_c)$  that is a generalization of a  $\chi^2$  function, that encompasses all the non-Gaussian features of the  $d_L$  posterior distribution:

$$\ln \mathcal{L}(d|\theta_c) = \sum_i^{N_{\text{events}}} \mathcal{K}_{\text{GW}}^i(d_L(\theta_c)) \quad (3.2)$$

where  $N_{\text{events}}$  depends on the choice of data set and detector configuration (see Tab. 1), and  $\mathcal{K}_{\text{GW}}^i$  is the KDE interpolation of the  $i$ -th posterior. We consider the MCMC chains to be converged when the Gelman-Rubin criterion [137] satisfies  $R - 1 < 0.01$ .

Besides the large set of joint GRB-GW mock data sets resulting from the detector configurations that we have just illustrated, for some of the runs we make use of the following additional complementary data:

- the catalog of uncalibrated SNIa from Pantheon+, spanning redshifts  $0.01 < z < 2.3$  [119]. In this paper, we always use mock Pantheon+ data generated distributing the distance modulus according to the underlying cosmology that we want to test (MOD1 or MOD2) while retaining the original Pantheon+ uncertainties. This is done to ensure to not mix real data (for which the underlying cosmology is unknown) with artificially generated ones. The only case when we use the actual Pantheon+ data set is when combining the latter with the real BAO data set (for further details see Subsection 3.2);
- the BAO measurements from 6dFGS at  $z = 0.106$  [138], SDSS DR7 at  $z = 0.15$  [139], BOSS DR12 at  $z = 0.38, 0.51$  and  $0.61$  [140], and the joint constraints from eBOSS DR14 Lyman- $\alpha$  auto-correlation at  $z = 2.34$  [141] and cross-correlation at  $z = 2.35$  [142]. In the following we use these data to calibrate the Pantheon+ real data set. Where it is specified, we combine BAO with a Gaussian prior on the sound horizon at the baryon drag epoch ( $r_{s,\text{drag}}$ ). This is done to have more reliable contours due to the addition of a piece of information coming from the CMB epoch;
- the forecast for DESI constraining power is based on the use of the full data set from the 5-year mission. We assume a sky coverage of  $14,000 \text{ deg}^2$ , as described in [143]. Hereafter we dubbed this mock data set as DESI(Y5).
- the SH<sub>0</sub>ES catalog of SNIa at redshift  $z \leq 0.01$ , calibrated through direct distance ladder method based on Cepheid variables [144].

We present constraints on MOD1 and MOD2 in this fashion: in Subsection 3.1 we compare the the 2G and the 3G GW detector capabilities; Subsection 3.2 is dedicated to investigate the potential of 3G detector configurations in constraining a MOD1 Universe and a MOD2 Universe; in Subsections 3.3 and 3.4 we discuss constraints obtained with our model-independent reconstruction method, on MOD1 and MOD2, respectively.

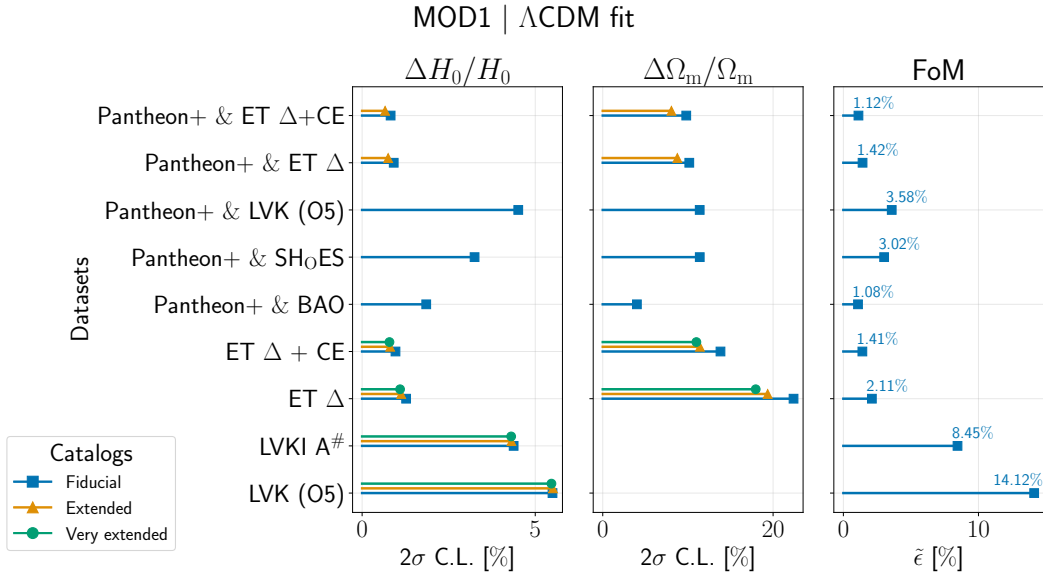


**Figure 3.** Whisker plot reporting the  $2\sigma$  relative uncertainties on  $H_0$  and  $\Omega_m$ , as well as the corresponding FoMs, obtained by fitting an underlying MOD1 cosmology assuming  $\Lambda$ CDM. For some of the cases, we report the results for the three different GRB catalogs. In the main text, we refer only to the fiducial catalog. We do not show the error bars larger than  $\gtrsim 100\%$ . The complete version of this plot is in Appendix C.

To quantify the constraining capabilities of the various combinations of data sets and detector combinations, we refer to a Figure of Merit (FoM) quantity [145] defined as:

$$\text{FoM}_X = [\det \mathcal{C}_X(\theta_c)]^{-1/2} \quad (3.3)$$

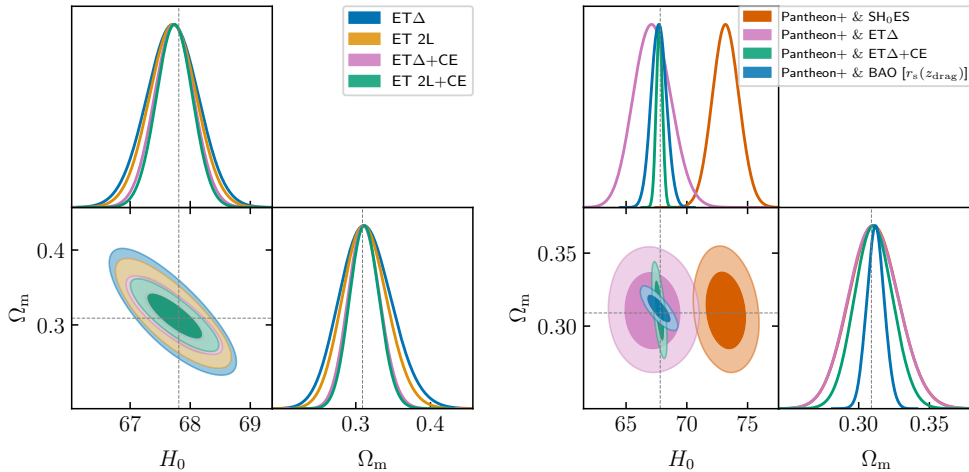


**Figure 4.**  $\Lambda$ CDM constraints (1- and 2- $\sigma$  C.L.) on the  $H_0$  and  $\Omega_m$  obtained by fitting MOD1 (dashed lines). (*Left*) Comparison among the ET $\Delta$ (+CE) and ET2L(+CE) configurations. (*Right*) Focus on ET $\Delta$  and LVK jointly analyzed with uncalibrated SNIa data. These are compared with BAO and SH<sub>0</sub>ES data sets.

where  $X$  stands for the detector configuration (*e.g.*  $X=\text{ET}\Delta+\text{CE}$  or  $X=\text{PP}+\text{BAO}$ ) and  $\mathcal{C}_X(\theta_c)$  is the covariance matrix extracted from the MCMC chains. The higher is the FoM, the higher is the constraining power over the set of cosmological parameters ( $\theta_c$ ). We now introduce a *reference* FoM,  $\text{FoM}_\epsilon^{\text{ref}}$ , that embodies the capability of a set of fully uncorrelated parameter estimates, *i.e.* with a diagonal covariance matrix. Given a set of reference cosmological values  $\bar{\theta}_c$ , we associate  $\text{FoM}_\epsilon^{\text{ref}}$  to the relative uncertainty  $\epsilon \equiv \sigma_{\theta_c}/\bar{\theta}_c$  we want to accomplish. In the  $H_0 - \Omega_m$  plane we can write

$$\text{FoM}_\epsilon^{\text{ref}} = \left[ \det \begin{pmatrix} \sigma_{H_0}^2 & 0 \\ 0 & \sigma_{\Omega_m}^2 \end{pmatrix} \right]^{-1/2} = \left[ \det \begin{pmatrix} \epsilon^2 \bar{H}_0^2 & 0 \\ 0 & \epsilon^2 \bar{\Omega}_m^2 \end{pmatrix} \right]^{-1/2} = \frac{1}{\epsilon^2 \bar{H}_0 \bar{\Omega}_m} \quad (3.4)$$

This provides an intuitive method to obtain the FoM of a specific detector configuration  $X$  relative to a reference FoM by setting a reference value for  $\epsilon$ . For example, setting  $\epsilon = 1\%$  establishes the reference FoM as a fixed value for comparison. If the investigated  $\text{FoM}_X$  is similar to the reference one, it indicates that the  $X$  detector configuration is approaching a 1% equivalent precision for both the cosmological parameters. We can invert Eq. (3.4) to find

$$\epsilon = \sqrt{\frac{1}{\text{FoM}_\epsilon^{\text{ref}} \bar{H}_0 \bar{\Omega}_m}} \quad (3.5)$$

We now introduce a practical way to quantify the precision achieved by a specific configuration  $X$ , *i.e.* the effective relative uncertainty  $\tilde{\epsilon}_X$ , defined as

$$\tilde{\epsilon}_X = \sqrt{\frac{1}{\text{FoM}_X \bar{H}_0 \bar{\Omega}_m}}. \quad (3.6)$$

We stress that  $\tilde{\epsilon}_X$  does not identify the true statistical uncertainty. Rather, it represents a useful proxy to compare the capabilities of different detectors. In this specific case study, this metric is straightforward and cannot be misinterpreted because the parameter degeneracies remain unchanged. This makes it an optimal method for comparing the significance of different detector configurations. We report the actual  $2\sigma$  relative uncertainties on the relevant cosmological parameter in Appendix C and the whisker plots throughout the main text.

### 3.1 Comparison between 2G and 3G GW detectors

In this Section we compare the performances of 2G and 3G GW detectors. Unless otherwise stated, we always assume that the analysis is performed with the fiducial GRB catalog. We show and compare results obtained with different catalogs in Appendix A. We discuss only the MOD1 mock data-set and the  $\Lambda$ CDM reconstruction. As similar considerations can be done for other fitting models, we discuss further cases in Appendix B. The uncertainty in the cosmological parameters are the  $2\sigma$  relative uncertainties obtained from the MCMC chains (*e.g.*,  $\Delta H_0/H_0 = 2\sigma_{H_0}/H_0$ )<sup>11</sup>. We quote as FoM the value of  $\tilde{\epsilon}$  obtained adopting the prescription given by Eq. (3.6).

In the left panel of Figure 2 we show the constraints extracted from the LVK (O5), LVKI A<sup>#</sup> and ET $\Delta$  analyses. For LVK, we find a 5.5% uncertainty on  $H_0$  and a 4.4% for LVKI A<sup>#</sup>, while ET $\Delta$  stands at 1.3% accuracy. Concerning  $\Omega_m$ , one can clearly see that both in the LVK and LVKI A<sup>#</sup> cases it is practically unconstrained, *i.e.*, with a relative uncertainty  $\gtrsim 100\%$ . The FoMs summarize these considerations:  $\tilde{\epsilon}_{\text{LVK}} = 14.1\%$ ,  $\tilde{\epsilon}_{\text{LVKIA}^\#} = 8.4\%$  and

<sup>11</sup>We adopt a different convention with respect to Ref. [95]



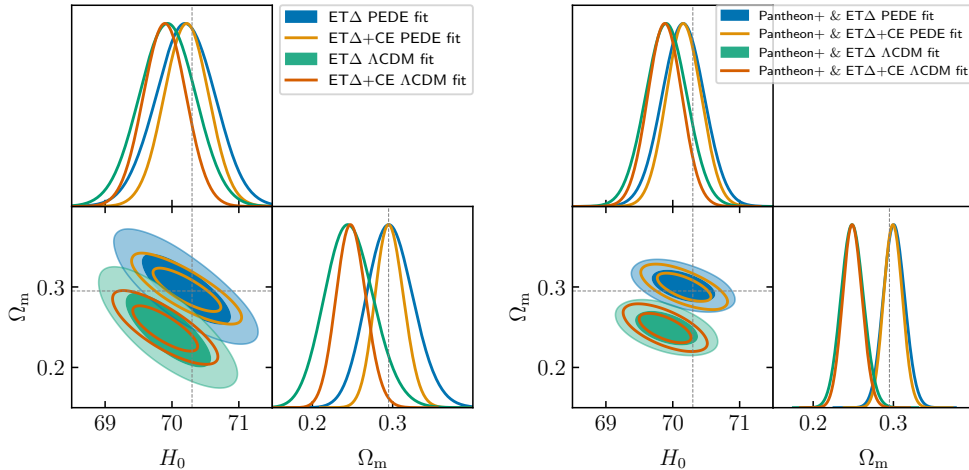


**Figure 5.** PEDE (blue and orange) and  $\Lambda$ CDM (green and dark orange) constraints on  $H_0$  and  $\Omega_m$  obtained by fitting a PEDE cosmology (MOD2). (*Left*) Comparison between  $ET\Delta$  and  $ET\Delta+CE$ . (*Right*) Joint analyses of the configurations used in the left panel with uncalibrated SNIa data.

$\tilde{\epsilon}_{ET\Delta} = 2.1\%$ . These numbers and the relative uncertainties on the cosmological parameters are reported in Figure 3 (but see also Appendix C). To overcome the issue of an unconstrained  $\Omega_m$ , as it is due to the limited redshift coverage of 2G detectors, it is worth performing a joint analysis with a tracer of  $H(z)$  at  $z \gtrsim 1$ , such as the uncalibrated SNIa data catalog from Pantheon+. These explore the regime where the  $\{d_L - z\}$  relation is influenced by the  $\Omega_m$  and  $\Omega_{DE}$  values. We show the results of the joint GW+SNIa analyses in the right panel of Figure 2. In other words, as the  $z_{\max}$  reached by 2G detectors like LVK is  $\approx 0.25$ , they can only constrain the Taylor expansion at low redshift of Eq. (2.3) (*i.e.*, the Hubble’s law). Therefore, for LVK, the addition of Pantheon+ data does improve the constraints on  $\Omega_m$  down to 11% with just 8 GW events. Note that the resulting FoM ( $\tilde{\epsilon}_{PP+LVK} = 3.6\%$ ) is still higher than the one from 3G detectors alone, as also shown in Figure 3. From Figure 2 it is clear that 3G detectors, being able to observe a larger volume, are themselves a good tracer of  $H(z)$  up to  $z_{\max} \approx 3$ . However, one can appreciate the enhanced constraining capabilities provided by the addition of Pantheon+ even when combined with 3G GW data. The corresponding FoM is  $\tilde{\epsilon}_{PP+ET\Delta} = 1.4\%$ , to be compared with  $\tilde{\epsilon}_{ET\Delta} = 2.1\%$ . We finally notice that the closest MM events, for which 3G detectors would provide the lowest uncertainty in the  $d_L$  estimation (see the orange curve in Figure 1), are the ones for which the peculiar velocity is the dominant component of the uncertainty. Such an ever-present source of uncertainty at low redshift could be mitigated by a better modeling of the host galaxy peculiar motion. In Appendix C we show a comparison with the ideal case of no peculiar velocities, namely without the correction that we introduced in Section 2.1.

### 3.2 Comparison among different 3G GW detectors

In this Section we focus our discussion on comparing the performances of different configurations of 3G GW detector networks, with and without additional external SNIa data from Pantheon+. To begin with, we present the results of the reconstruction of an underlying  $\Lambda$ CDM cosmology (MOD1) with parameters  $\theta_c^{\Lambda\text{CDM}} = \{H_0 = 67.81 \text{ km Mpc}^{-1}\text{s}^{-1}, \Omega_m = 0.309\}$ . We do not explicitly show the case of a PEDE fitting model over MOD1 because this

is completely similar to carry out a  $\Lambda$ CDM fit on MOD2, that is the second case that we discuss in detail in this Section.

In the left panel of Figure 4 we compare the ET $\Delta$ , ET2L, ET $\Delta$ +CE and ET2L+CE configurations. A full comparison of all the configurations examined in this paper is available in Appendix C (Table 3 and Figure 24). From the left panel of Figure 4 we notice that the ET2L configuration performs better than ET $\Delta$ , both alone and in a network with CE. For ET $\Delta$  (ET2L) we obtain an uncertainty on  $H_0$  of 1.3% (1.2%), on  $\Omega_m$  of 22% (19%) and a FoM of 2.1% (1.9%). Notice also that the addition of CE shrinks the contours, improving the constraining power with respect to ET alone in either of its configurations, reaching a sub-percent level precision on  $H_0$ . This results in a highly similar FoM in the two cases: 1.4% for ET $\Delta$ +CE and 1.3% for ET2L+CE. The improvement observed in the latter two configurations can be attributed to the factors briefly mentioned at the end of Subsection 2.3. Specifically, these improvements result from the combined effect of the duty cycle and the increased sensitivity of the network with the introduction of the CE observatory.

In the right panel of Figure 4, we present the results obtained by combining the Pantheon+ data set with LVK and ET $\Delta$ . These results are compared to the current measurements of  $H_0$  and  $\Omega_m$  from Pantheon+ data calibrated with both SH<sub>0</sub>ES and BAO. In the analysis with SH<sub>0</sub>ES, both the mock GW and mock Pantheon+ data sets are generated with the same MOD1 underlying cosmology, and jointly analyzed to accurately reconstruct  $\Omega_m$ . On the contrary, actual BAO data are combined with the actual Pantheon+ data set. This strategy, outlined in Subsection 2.4, enables a fair visual comparison between current and future experiments<sup>12</sup>. As shown by the contours in the right panel of Figure 4, combining current SNIa data with GWs yields constraining capabilities similar to those provided by both BAO. We underline that the BAO constraints on  $\Omega_m$  outperform the ones from GW data, while the contrary happens for the estimates on  $H_0$ , resulting in comparable FoMs for the two cases, namely  $\tilde{\epsilon}_{\text{PP+BAO}} = 1.1\%$  and  $\tilde{\epsilon}_{\text{PP+ET}\Delta} = 1.4\%$ . As testified by the tightness of the contours that we report, GW observations from future interferometers are a promising way to finally unambiguously set the  $H_0$  (or cosmic calibrator) tension debate [22, 24, 146–148]. From Figure 3 we notice that the extended catalog (containing 53 events, rather than 38, in the ET $\Delta$ +CE configuration) consistently provides more precise limits, while using the very extended catalog (60 events) does not significantly improve the constraints. The improvement is in fact primarily driven by the inclusion of high- $z$  GRBs, rather than by the larger statistics. However, since such improvement is always of the same order, we stick to discussing only the results obtained with the fiducial catalog. We refer the reader to Appendix A for a comprehensive comparison among all catalogs.

We now discuss the MOD2 underlying cosmology, that we produced considering a conservative set of parameters for the PEDE scenario, namely  $\theta_c^{\text{PEDE}} = \{H_0 = 70.3 \text{ km Mpc}^{-1}\text{s}^{-1}, \Omega_m = 0.295\}$ . As explained in Section 2.4, these fiducial values correspond to the best-fit parameters from a joint analysis with Pantheon+, BAO data from eBOSS, and *Planck* 2018 CMB data. In Figure 5 we compare constraints obtained by fitting MOD2 with PEDE and with  $\Lambda$ CDM, for ET $\Delta$  (filled contours) and ET $\Delta$ +CE (empty contours), with and without Pantheon+ (left and right panel, respectively). One can easily see that the size of the contours are similar. In fact, the ET $\Delta$  FoMs for PEDE and  $\Lambda$ CDM are  $\tilde{\epsilon}_{\text{ET}\Delta} = 1.9\%$  and  $\tilde{\epsilon}_{\text{ET}\Delta} = 2.0\%$ , respectively. As stated before, we underline that the

<sup>12</sup>Note that, even when combining real data with mock data, the FoM reflecting the constraining power would remain unchanged. This is because the precision is not influenced by whether the injected cosmological parameters are correctly recovered.

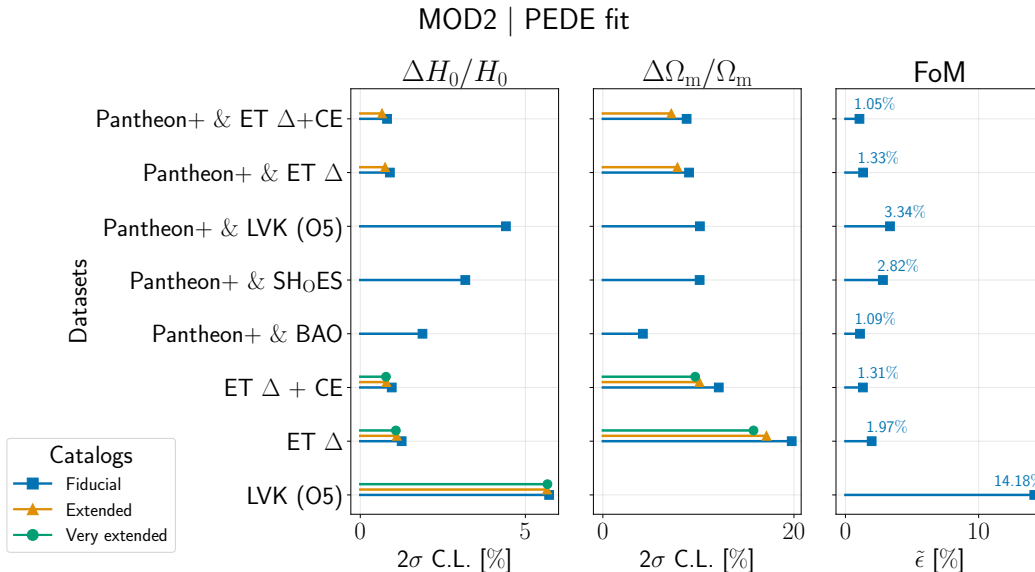


**Figure 6.** Whisker plot reporting the  $2\sigma$  relative uncertainties on  $H_0$  and  $\Omega_m$ , as well as the corresponding FoMs, obtained by fitting an underlying MOD2 cosmology assuming PEDE. The absence of line is related to an uncertainty greater than  $\gtrsim 100\%$ . The complete version of this plot is in Appendix C.

network of ET $\Delta$  and CE outperforms the ET $\Delta$  alone, for both the fitting cosmologies. The difference becomes even less evident in the joint analysis with Pantheon+ (right panel). The value of the FoMs for ET $\Delta$  are  $\tilde{\epsilon}_{\text{PP+ET}\Delta} = 1.3\%$  and  $\tilde{\epsilon}_{\text{PP+ET}\Delta} = 1.4\%$ , for PEDE and  $\Lambda$ CDM respectively. These two GW detector configurations give similar constraints on  $H_0$ , whereas ET $\Delta$ +CE is a factor 1.6 better in constraining  $\Omega_m$  (see Table 6). This can be attributed to the ability of the ET $\Delta$ +CE configuration to detect GRBs at higher redshifts compared to the ET $\Delta$  configuration alone. The FoM of ET $\Delta$  is indeed roughly a factor 2 larger than the one of ET $\Delta$ +CE ( $\tilde{\epsilon}_{\text{ET}\Delta} = 2\%$  and  $\tilde{\epsilon}_{\text{ET}\Delta+\text{CE}} = 1.3\%$ ). As expected, the addition of Pantheon+ data drives the  $H_0$  and  $\Omega_m$  constraints to become very similar, so that the FoMs in this case read  $\tilde{\epsilon}_{\text{PP+ET}\Delta} = 1.3\%$  and  $\tilde{\epsilon}_{\text{PP+ET}\Delta+\text{CE}} = 1.0\%$ . We report the list of FoMs and uncertainties discussed in this Section in Figure 6, while the full list is shown in Appendix C (Table 6 and Figure 27).

Notice that, even though MOD1 and MOD2 are characterized by relatively similar phenomenologies, when MOD2 is fitted within  $\Lambda$ CDM, we do not retrieve the injected values of the cosmological parameters. This is due to the fact that  $\Lambda$ CDM is not able to reproduce the phenomenology of a dynamical DE described by the  $w(z)$  evolution (Eq. (2.7)). Therefore, the net effect of wrongly assuming  $\Lambda$ CDM as a fitting model is a shift in the inferred values of  $\Omega_m$  and  $H_0$  towards values lower than the injected ones. Such a shift clearly points toward a crucial fact: assuming an arbitrary model to fit data under an unknown underlying cosmology might produce biased results. From the left panel of Figure 5 it is apparent that in the ET $\Delta$  configuration such biases are present but not statistically significant, whereas in the most constraining case of ET $\Delta$ +CE the shift between  $\Lambda$ CDM and PEDE contours is larger than  $2\sigma$ . Analogous considerations apply to the joint GW+SNIa analysis (right panel). We explicitly checked that the same issue occurs when PEDE is fitted on the MOD1 mock data set. In the next Subsections 3.3 and 3.4 we will show how to overcome this problem by means

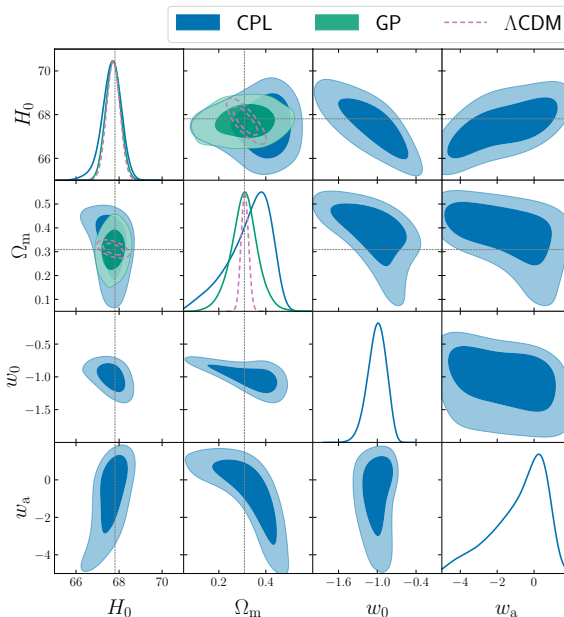


**Figure 7.** CPL (blue), GP (green) and  $\Lambda$ CDM (empty pink) constraints on  $H_0$ ,  $\Omega_m$ ,  $w_0$  and  $w_a$  obtained by fitting a PEDE cosmology (MOD2). (*Upper corner*) Contour comparison for ET $\Delta$  alone. (*Lower corner*) Contour comparison for ET $\Delta$  joint analysis with uncalibrated SNIa data. The 1-dimensional posterior refers to the lower corner plot.

of model-independent reconstruction techniques.

### 3.3 Model-independent reconstruction of a $\Lambda$ CDM Universe (MOD1)

In this Section we focus on the comparison of parametric (CPL) and non-parametric (GP) fitting methods over MOD1. When comparing GP with CPL, besides  $H_0$  and  $\Omega_m$ , we show the constraints on the DE EoS parameters,  $w_0$  and  $w_a$ . Only when discussing the GP results alone, we show the constraints on the GP hyperparameters  $\sigma_f$  and  $\ell_f$  (in logarithmic scale for visualization purposes). In the case of MOD1 we focus on the results for ET $\Delta$  and its combination with Pantheon+, while a fully comprehensive set of results can be found in Appendix C (Tables 4, 5, and Figures 25, 26). From Figure 7, as expected, one can see that the constraining power on  $H_0$  and  $\Omega_m$  from both GP and CPL is lower with respect to the cases presented in Subsection 3.2, due to the larger parameter space explored. In particular, the upper corner plot displays the constraints for ET $\Delta$ , while the lower corner one shows the combination of Pantheon+ with ET $\Delta$ . The one-dimensional marginalized posteriors refer to the lower corner plot, *i.e.*, to the most constraining configuration. We compare the CPL, GP and  $\Lambda$ CDM fitting models. As just stated, having more freedom, both CPL and GP perform worse in terms of constraining power with respect to the  $\Lambda$ CDM fit. Nonetheless, both of them are able to recover the injected cosmology. In the case of ET $\Delta$ , the CPL constraint on  $H_0$  is 2.6%, while the one given by GP is 1.5%. For what concerns  $\Omega_m$ , we get a relative uncertainty of 61% in CPL, and of 58% for GP. The FoMs are  $\tilde{\epsilon}_{\text{ET}\Delta} = 6.3\%$  and  $\tilde{\epsilon}_{\text{ET}\Delta} = 4.6\%$ , for CPL and GP respectively. Thus, we can conclude that the agnostic reconstruction of GP outperforms the standard parametric CPL approach. The difference between the two is a factor  $\sim 1.3$ .

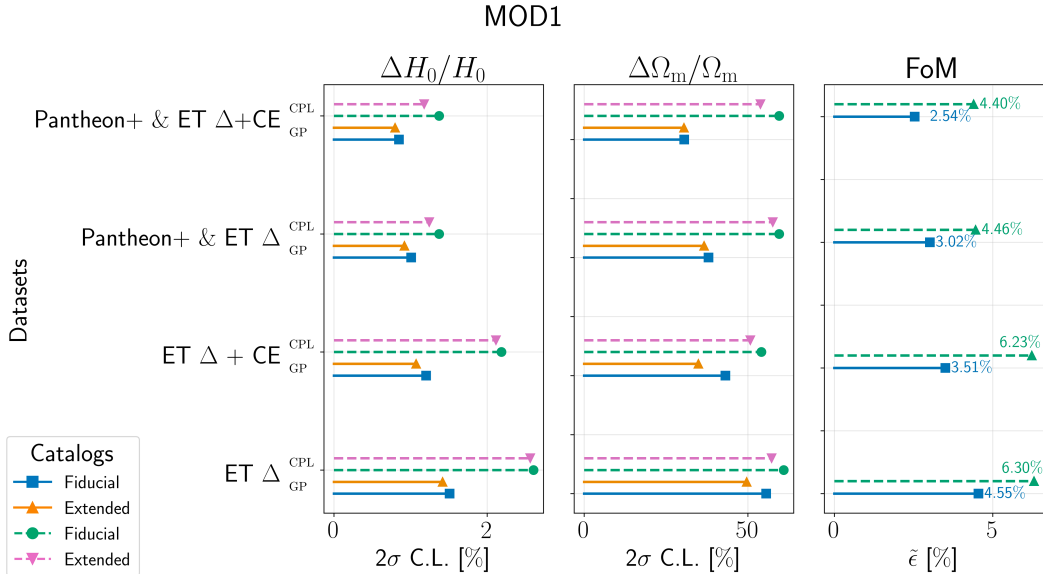


**Figure 8.** Whisker plot reporting the  $2\sigma$  relative uncertainties on  $H_0$  and  $\Omega_m$ , as well as the corresponding FoMs, obtained by fitting an underlying MOD1 cosmology. We compare the CPL (dashed lines) and GP (solid lines) estimates for fiducial and extended catalogs. The FoMs are reported only for the fiducial catalog.

The constraining capability and eventually the FoM further improve when we include Pantheon+, as the additional constraint on  $\Omega_m$  allows to better constrain the DE evolution. The tightening of the contours translates into more precise estimates of both  $H_0$  and  $\Omega_m$ . The  $H_0$  ( $\Omega_m$ ) uncertainties are 1.4% (60%) and 1.0% (40%) for CPL and GP respectively. The FoMs are  $\tilde{\epsilon}_{PP+ET\Delta} = 4.5\%$  for CPL and  $\tilde{\epsilon}_{PP+ET\Delta} = 3.0\%$  for GP. The precision of the GP constraints in this case improves over CPL by a factor  $\sim 1.5$ . In Figure 8 we report a comprehensive comparison of the CPL and GP relative uncertainties and FoMs.

We now discuss the GP reconstruction of the function  $f_{DE}(z)$ , as shown in the upper panel Figure 9, obtained by marginalizing over the two cosmological parameters ( $H_0$  and  $\Omega_m$ ) and the two hyperparameters ( $\sigma_f$  and  $\ell_f$ ). The  $f_{DE}$  reconstruction is perfectly in agreement with the MOD1 underlying model (reported as a dashed black line in the plots), for the entire redshift range spanned by our data.<sup>13</sup> The colored line represents the best-fit reconstruction, while the shaded areas around it are the 1- and 2- $\sigma$  contours. We show the reconstruction performed for ET $\Delta$ , ET $\Delta$ +CE, both with and without Pantheon+. As explained in Subsection 2.5 we have adopted an untrained GP procedure [80, 83]. For this reason, the  $f_{DE}$  is well-inferred even where no data points are present. As reflected by the FoM quoted above, the more the cosmological probes are constraining, the more the  $f_{DE}$  uncertainty decreases. However, all of them show a worsening of the uncertainties at  $z > 1$ , reflecting the uncertainty associated with the GRB-GW mock catalogs. The main limitation preventing a more precise inference of the DE phenomenology is given by the poor estimates of the  $d_L$  parameter at high- $z$ . A larger number of GRBs at higher  $z$  with respect to the ones currently available would significantly reduce the uncertainties on the reconstructed  $f_{DE}$ . This is clearly visible

<sup>13</sup>This was expected, as the GP mean function corresponds to the true underlying cosmology used to generate the data. We will show that the method is able to recover the true cosmology even when the latter differs from the GP mean function in the next Subsection.

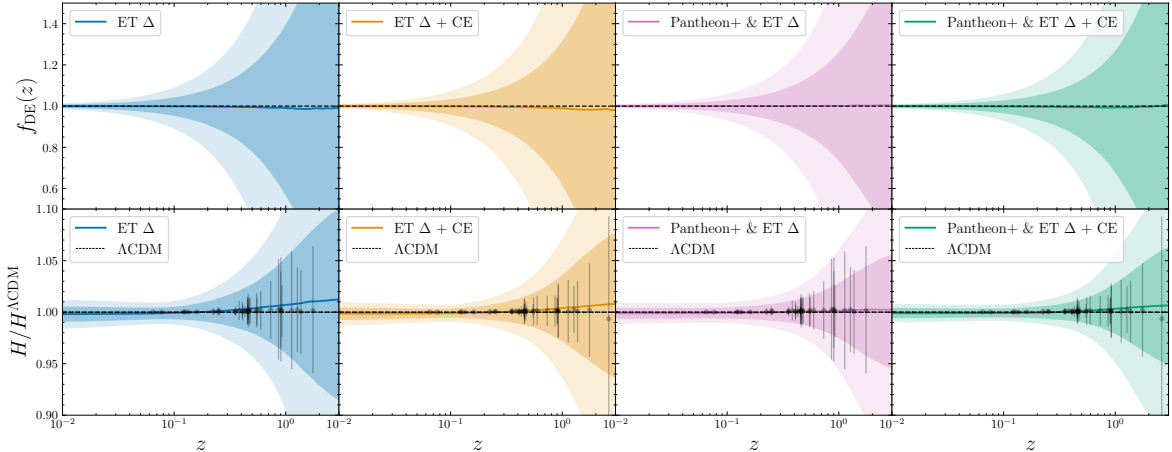


**Figure 9.** Marginalized posterior distributions on  $f_{\text{DE}}(z)$  and  $H(z)/H^{\Lambda\text{CDM}}$  obtained with GP for an underlying MOD1 Universe. The dashed lines show the  $\Lambda\text{CDM}$  behaviour of  $f_{\text{DE}}(z)$  and  $H(z)/H^{\Lambda\text{CDM}}$ . The colored solid lines show the best-fit GP reconstruction of those functions while the contours around the solid lines are the C.L. at 1- and 2- $\sigma$ . From left to right we display the ET $\Delta$  (+CE) configuration and the same but including the Pantheon+ mock data set (last two plots). These results are relative to the fiducial GRB catalog.

by looking at how the FoMs get smaller, for all detector configurations, when the extended GRB catalog is used instead of the fiducial one (see Table 5). A similar discussion can be done regarding the reconstructed Hubble parameter  $H(z)$ , normalized to the MOD1  $\Lambda\text{CDM}$  fiducial expansion rate, displayed in the lower panels of Figure 9. The results reflect the ones seen for  $f_{\text{DE}}$ : the most constraining configuration is given by Pantheon+ joint with ET $\Delta$ +CE. The data points and error bars are derived by propagating the uncertainties from the  $d_L$  posterior, which was estimated using our GW detector simulator, assuming the same underlying cosmology injected to generate the mock data.

### 3.4 Model-independent reconstruction of a PEDE Universe (MOD2)

In this Subsection we discuss the results obtained with CPL and GP on the GRB-GW mock data set generated assuming PEDE (MOD2). We report the results of the ET $\Delta$  and ET $\Delta$ +CE configurations in the left and right panels of Figure 10, respectively. We show the contours for all the fitting models considered in this work, *i.e.* CPL, GP,  $\Lambda\text{CDM}$  and PEDE. In Figure 10, the results are displayed as in Subsection 3.3: the corner plot in the upper part contains the results with GW data alone, while the lower part is dedicated to the joint analysis with Pantheon+. As already stated in Subsection 3.2, the  $\Lambda\text{CDM}$  and PEDE fits are comparable in terms of precision, but the  $\Lambda\text{CDM}$  fit clearly presents a bias in the inferred cosmological parameters. In fact, the injected values of  $H_0$  and  $\Omega_m$  lie outside the 2- $\sigma$  contours of  $\Lambda\text{CDM}$ . In the case of the ET $\Delta$ +Pantheon+ joint analysis (left panel of Figure 10) we report a relative uncertainty on  $H_0$  of 1.0% (1.6%) for GP (CPL). For  $\Omega_m$  the uncertainty of the parametric and non-parametric fits are comparable: 40% (42%) for GP (CPL) (see Figure 11). The FoM is  $\tilde{\epsilon}_{\text{PP+ET}\Delta} = 3.9\%$  in the CPL case, while it is  $\tilde{\epsilon}_{\text{PP+ET}\Delta} = 3.1\%$  in the case of GP. These results correspond to a GP reconstruction that is a factor 1.3 better than CPL. The same trend is present also for the ET $\Delta$  configuration alone (left panel of Figure 10, upper corner). In the right panel of Figure 10 we instead show the result of the ET $\Delta$ +CE configuration. We again confirm the enhanced constraining power of this configuration with respect to the ET $\Delta$

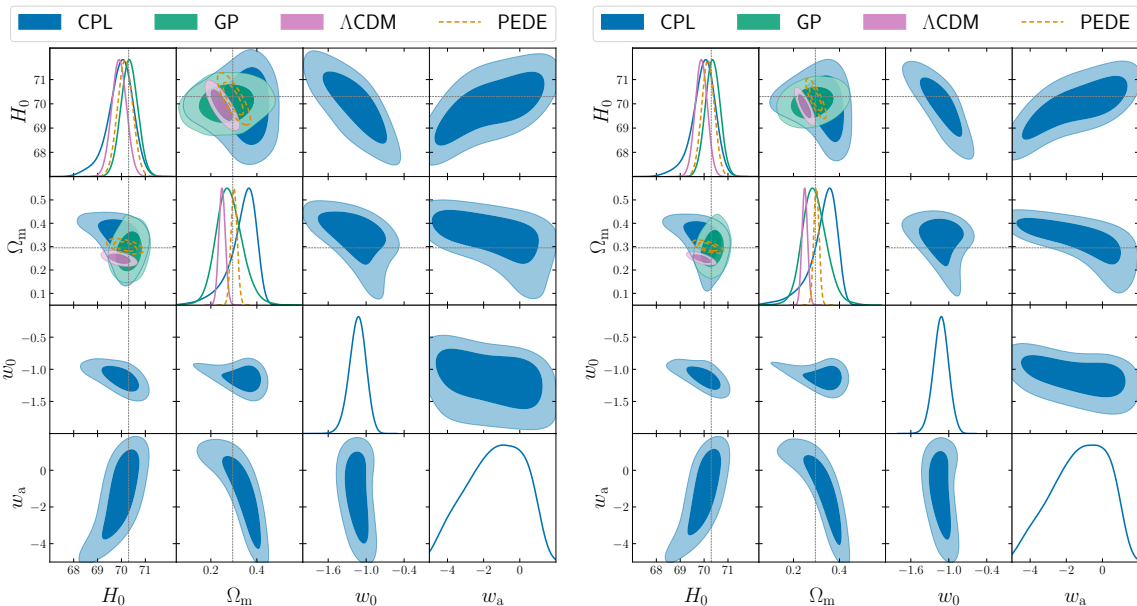


**Figure 10.** CPL (blue), GP (green),  $\Lambda$ CDM (pink) and PEDE (empty yellow) constraints on  $H_0$ ,  $\Omega_m$ ,  $w_0$  and  $w_a$  obtained by fitting a PEDE cosmology (MOD2). (*Left*) (*Upper corner*) Contour comparison for ET $\Delta$  alone. (*Lower corner*) Contour comparison for ET $\Delta$  joint analysis with uncalibrated SNIa data. (*Right*) Same as the left panel but for the ET $\Delta$ +CE network. The 1-dimensional posterior refer to the lower corner plot.

one. The relative uncertainty on  $H_0$  is 0.9% (1.4%) in the GP (CPL) case. The reconstructed values of  $\Omega_m$  are again comparable for the two reconstructions, giving an uncertainty of 37% (43%) for GP (CPL). This gives us a FoM of  $\tilde{\epsilon}_{\text{PP+ET}\Delta+\text{CE}} = 3.8\%$  for CPL and of  $\tilde{\epsilon}_{\text{PP+ET}\Delta+\text{CE}} = 2.8\%$ . In other words, GP again outperforms CPL by a factor 1.3. The full set of results is available in Appendix C (Tables 7, 8, and Figures 28, 29). For completeness, in Figure 12 we present constraints obtained with the GP fit over MOD2 for ET $\Delta$  and ET $\Delta$ +CE, both with and without the Pantheon+ data set. Note that we require the GP samples to satisfy  $f_{\text{DE}}(z=0) \equiv 1$  by definition. This condition, combined with the relatively large correlation lengths  $\log \ell_f \sim 2$  favored by the data, leads to a narrowing of uncertainty around  $z=0$ . At the same time, it allows for relatively large deviations from the mean function, with  $\log \sigma_f \sim 1$ , as long as these deviations occur outside the range probed by the data. This behavior is evident in the posteriors shown in Figure 12.

In Figure 13, we present the reconstructed DE density  $f_{\text{DE}}(z)$  and corresponding expansion history  $H(z)$  normalized to the  $\Lambda$ CDM one. The dashed line refers to the  $\Lambda$ CDM model evolution (MOD1,  $f_{\text{DE}} = 1$ ), while the red solid line reflects the underlying cosmology of the mock data (MOD2). The configurations shown are increasingly more constraining from left to right. In the case of Pantheon+ and ET $\Delta$ +CE joint analysis, we see that the reconstructed cosmology is in perfect agreement with the one used for generating the mock data. In this case, the  $f_{\text{DE}} = 1$  line lies on the edge of the 1- $\sigma$  contours. In the lower panel, we note a deviation from the reference  $H(z)$  behaviour set by MOD1 in the  $0.01 < z < 0.2$  region. However, this is expected because it is driven by the difference in the injected parameters ( $H_0$  and  $\Omega_m$ ) between MOD1 and MOD2.

The limitations to a more refined reconstruction are primarily given by having only 38

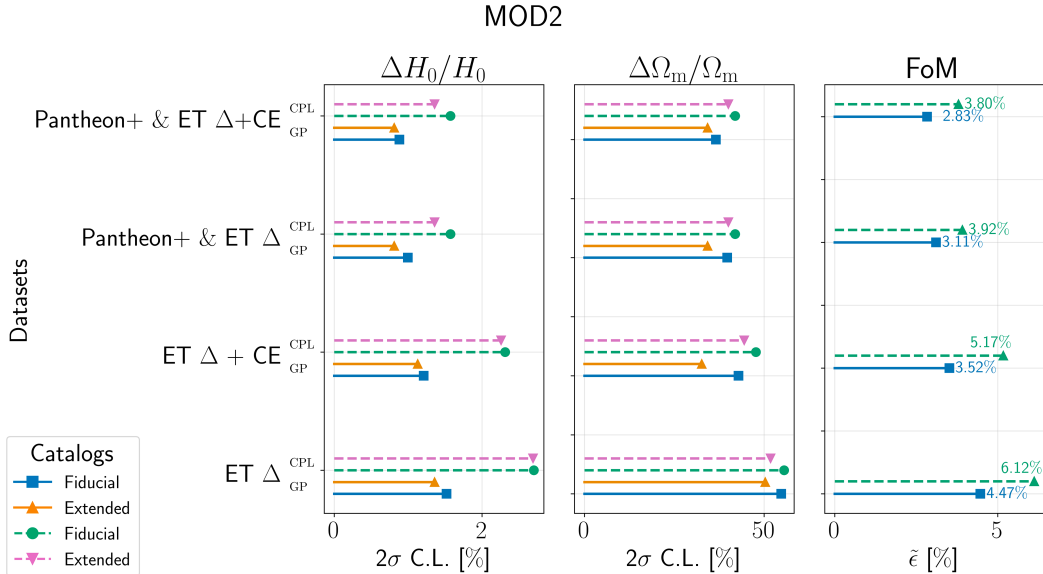


**Figure 11.** Whisker plot reporting the  $2\sigma$  relative uncertainties on  $H_0$  and  $\Omega_m$ , as well as the corresponding FoMs, obtained by fitting an underlying MOD2 cosmology. We compare the CPL (dashed lines) and GP (solid lines) estimates for fiducial and extended catalogs. The FoMs are reported only for the fiducial catalog.

GRB-GW data points, with a sparse representation at high redshifts, as well as by MOD2 being very similar to  $\Lambda$ CDM in terms of free parameters and phenomenology. In other words – although not statistically significant – these constraints are quite promising, as demonstrated by their tightening when the fiducial GRB catalog is replaced by the extended one (see Appendix C). It is important to note that the  $f_{\text{DE}}$  reconstruction typically aligns with the  $\Lambda$ CDM value at  $z \gtrsim 2.5$ . This behavior is intrinsic to the pipeline, which assumes that our Universe should resemble an Einstein-de Sitter model during the matter-dominated era. Indeed, not only do the error bars increase in size, but also the DE contribution becomes negligible at those redshifts where the Universe is matter dominated.

As a final remark, we note that the observational set-up considered in this context is conservative, as we are using a much smaller sample of EM counterparts compared to what will be available in the era of 3G detectors. A large number of KNe, from ten to several hundreds, are expected to be detected in association with GW signals [149]. Cosmological measurements from KN detection can be considered complementary to those of GRBs. Although the number of detections per year is higher, the redshifts achieved are limited to the relatively close Universe ( $z \lesssim 0.3$ ). Furthermore, unlike the present work on GRBs, the number of KN detections has large uncertainties as it is based on population synthesis datasets and poor constraints on local BNS merger rates. Another aspect to take into account is that our realistic scenario is based on the number of GRB detections by current detectors. Innovative projects are expected to be operative at the time of next generation GW detectors, for example cube-satellite constellations such as HERMES which will detect hundreds short GRBs per year [150], and observatories such as THESEUS which will detect smaller numbers (order of few tens short GRBs per year) but with an extremely good sky-localization to drive the ground-based follow-up to obtain their redshift [67, 102, 151]. Wide field-of-view (FoV) X-ray telescopes such as Einstein Probe [152], THESEUS-SXI [102], Gamov [153] are expected



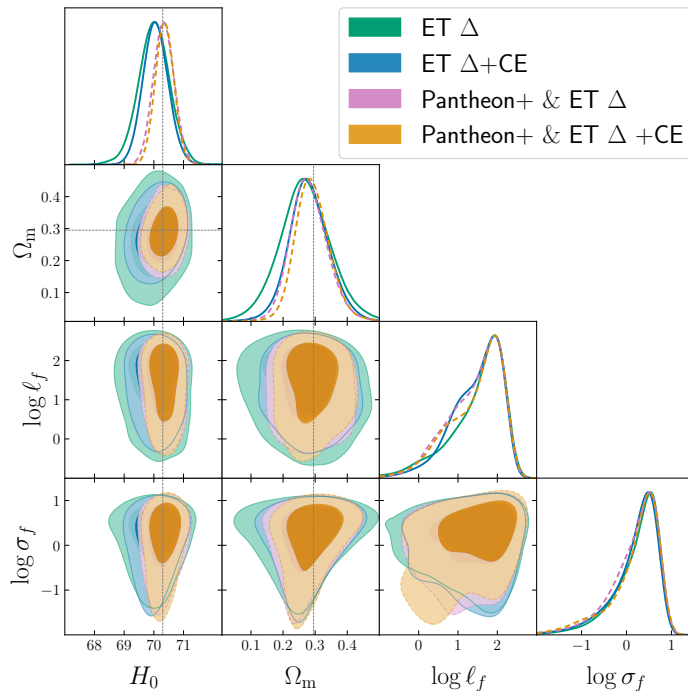


**Figure 12.** GP constraints (1- and 2- $\sigma$  C.L.) on the physical parameters  $H_0$  and  $\Omega_m$ , and the hyperparameters  $\log\sigma_f$  and  $\log\ell_f$  obtained by fitting MOD2 (dashed lines). We report the contours for ET $\Delta$  and ET $\Delta$ +CE with and without Pantheon+.

to detect a non-negligible fraction of BNS mergers observed off-axis, whose relativistic jets are not pointing to us to have a detectable  $\gamma$ -ray emission [67]. Instruments such as the wide FoV Vera Rubin Observatory [154] will be fully operational allowing efficient follow-up campaigns even for GW-GRB events that are not perfectly localised. Operating together with telescopes such as the Extremely Large Telescope [155, 156] or project such as the Wide Field Spectroscopic Telescope [157] will enhance host galaxy identification and redshift measurements.

In addition, we are combining and confronting GW data with currently operating SNIa and BAO surveys, whose performances will soon be surpassed by a large extent from new generation surveys such as DESI, Euclid and Nancy Grace Roman Space Telescope. We will focus on this topic in the following Subsection.

### 3.5 Future prospects

We now discuss cosmological constraints obtained by jointly analyzing the MM data sets presented in this work with mock data from next-generation BAO surveys such as DESI(Y5). As discussed in Subsection 3.4, integrating next-generation cosmological surveys with data from 3G detectors will yield even more precise insights into the nature of DE, possibly identifying potential deviations from the standard  $\Lambda$ CDM model. It is important to note that even the results presented in the present Subsection remain somewhat conservative, as we have not yet accounted for expected improvements in detecting GRBs and other EM counterparts providing the redshift of the sources. Such advancements will sensibly enhance the precision of our constraints, meaning that our current findings may still be underestimating the true potential of future observations.

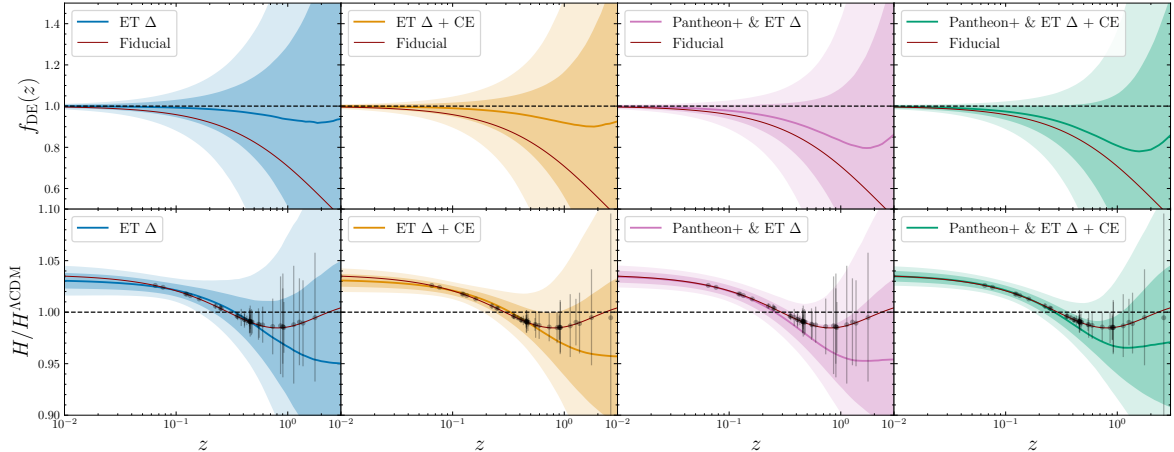


**Figure 13.** Marginalized posterior distributions on  $f_{\text{DE}}(z)$  and  $H(z)/H^{\Lambda\text{CDM}}$  obtained with GP for an underlying MOD2 Universe. The dashed lines show the  $\Lambda\text{CDM}$  behaviour of  $f_{\text{DE}}(z)$  and  $H(z)/H^{\Lambda\text{CDM}}$ . The colored solid lines show the best-fit GP reconstruction of those functions while the contours around the solid lines are the C.L. at 1- and 2- $\sigma$ . The red solid line report the fiducial cosmology with which the data are generated. The data themselves are reported in black in the  $H(z)/H^{\Lambda\text{CDM}}$  panel. From left to right we display the ET $\Delta$  (+CE) configuration and the same but including the Pantheon+ mock data set (last two plots). These results are relative to the fiducial GRB catalog.

In Figure 14 we compare the reconstruction capabilities of  $f_{\text{DE}}(z)$  and  $H(z)$  for ET $\Delta$  and DESI(Y5), both alone and in combination (details on the data generation are provided in Section 2). As in the previous Subsections, we show in the upper panels the reconstructed  $f_{\text{DE}}$ , while the corresponding  $H(z)/H^{\Lambda\text{CDM}}$  is displayed in the lower panels, normalized to the MOD1 expansion history. The underlying PEDE cosmology injected to generate the data (MOD2) is shown as a red solid line. In the left panel we show the constraints provided by ET $\Delta$  alone. In the middle panel we highlight the constraints provided by DESI(Y5), focusing solely on BAO measurements. In the right panel we show the results of the joint analysis of the two. The latter analysis explicitly shows that the  $f_{\text{DE}}$  GP reconstruction can distinguish deviations from  $\Lambda\text{CDM}$  cosmology with precision greater than  $2\sigma$ , within the  $0.06 \lesssim z \lesssim 0.7$  range. As already stated, the deviation from  $\Lambda\text{CDM}$  at low redshift is driven by the difference in the injected parameters ( $H_0$  and  $\Omega_m$ ) between MOD1 and MOD2. It is interesting to notice that neither ET $\Delta$  nor DESI(Y5) alone cannot distinguish the dynamical DE evolution in the intermediate region ( $0.06 \lesssim z \lesssim 0.7$  range). On the other hand, focusing on the  $H(z)$  estimates, one can clearly notice that the combination of ET $\Delta$ +DESI(Y5) is capable of distinguishing the  $\Lambda\text{CDM}$  departure at more than  $2\sigma$  level in the range  $0.6 \lesssim z \lesssim 1$ . As a result, the  $f_{\text{DE}}$  reconstruction is also very precise, clearly demonstrating the crucial role that will be played in the future by multi-probe model-independent approaches to disentangle different DE phenomenologies, even when almost fully degenerate one to another.

## 4 Summary and conclusions

In this work we presented cosmological constraints obtained by employing GRB-GW MM data. We constructed a catalog of GRB data observed in the past two decades by *Fermi*-GBM and *Swift*-BAT/XRT/UVOT. The use of real EM data prevents uncertainties associated

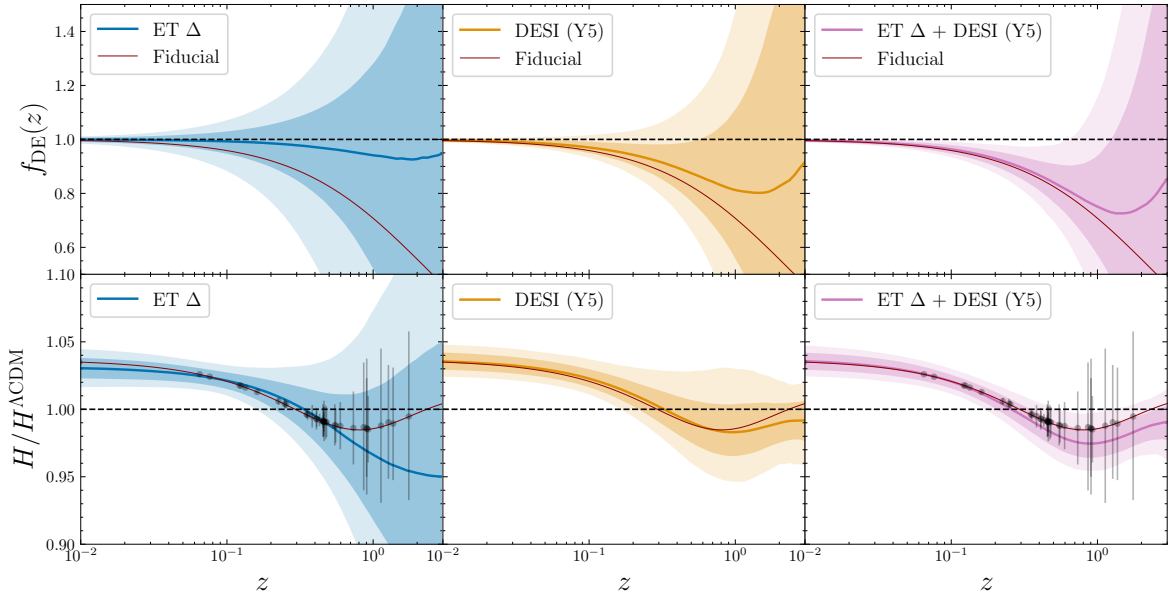


**Figure 14.** Marginalized posterior distributions on  $f_{\text{DE}}(z)$  and  $H(z)/H^{\Lambda\text{CDM}}$  obtained with GP for an underlying MOD2 Universe. The dashed lines show the  $\Lambda\text{CDM}$  behaviour of  $f_{\text{DE}}(z)$  and  $H(z)/H^{\Lambda\text{CDM}}$ . The colored solid lines show the best-fit GP reconstruction of those functions while the contours around the solid lines are the C.L. at 1- and 2- $\sigma$ . The GW data themselves are reported in black in the  $H(z)/H^{\Lambda\text{CDM}}$  panel. From left to right we display the ET $\Delta$ , DESI (Y5) and the combination of the two. These results are relative to the fiducial GRB catalog.

with BNS populations generated by population synthesis codes. We assumed that all GRB in our catalogs are merger-driven events, thus associated to a GW counterpart. The latter is analyzed in the context of the next 2G and 3G GW detectors. We carried out an extensive analysis both alone, and in combination with currently available BAO and uncalibrated SNIa data, as well as next-generation simulated ones.

To accomplish this, we devised a new numerical tool that is able to output the posterior distribution of the MM events luminosity distance taking into account the correction for the host galaxies' peculiar velocity. The GW parameter estimation is made possible by the use of `GWFish`, a GW parameter estimation tool based on a recently introduced prior-informed Fisher matrix approach [92]. The latest version of `GWFish` guarantees a more precise analysis with respect to standard Fisher matrix analyses, as it includes the physical priors of the GW parameters. The posteriors obtained through this procedure are then fitted using a KDE interpolation. As a final step, we developed a likelihood function to analyze the full KDE posterior generated by our pipeline, in order to extract cosmological constraints by means of a comprehensive set of MCMC analyses.

In the following, we outline our main results:

- we showed that even the more advanced configuration of 2G GW detectors (LVK(O5) and LVKI A<sup>#</sup>) will not be able to provide competitive cosmological constraints with BNS data alone. However, the joint analysis with the Pantheon+ data set provides comparable precision compared to that of current BAO data and calibrated SNIa (SH<sub>0</sub>ES). A good metric for this comparison is the  $\Lambda\text{CDM}$  fit over MOD1, which has a FoM approximately  $\tilde{\epsilon} \sim 3\%$ . 3G GW detectors provide instead outstanding constraints com-

pared to 2G detectors. We recap the uncertainties on the cosmological parameters and the relative FoM for the  $\Lambda$ CDM fit over MOD1 of LVK+Pantheon+ (8 GW events), ET $\Delta$  (36 GW events), and ET $\Delta$ +Pantheon+ (38 GW events), in this order: for  $\Delta H_0/H_0$  we have 4.5%, 1.3% and 0.9%; for  $\Delta\Omega_m/\Omega_m$  we get 11%, 22% and 10%; the relative FoM are 3.6%, 2.1% and 1.4%;

- we compared different 3G detector configurations and identified three key findings: (i) the ET non-cryogenic configuration, dubbed HF, provides cosmological constraints very similar to the full cryogenic configuration; (ii) the constraining capabilities of the ET2L are better than those coming from ET $\Delta$ ; (iii) adding CE to the network further improves the constraining power mostly due to the better overall sensitivity;
- we explicitly showed that fitting the data with an incorrect cosmological model could lead to misinterpretations of the underlying physics. This biased reconstruction can occur even when choosing a conservative alternative cosmology, as demonstrated in our analysis of the PEDE scenario (MOD2). The latter model has a very similar phenomenology with respect to the  $\Lambda$ CDM best fit to *Planck* 2018 data. Despite this, the fit of  $\Lambda$ CDM over MOD2 leads to an incorrect reconstruction. When the analysis is carried out with ET $\Delta$ +CE, it reveals a statistically significant bias ( $> 2\sigma$ ) even in the absence of Pantheon+ data;
- we assessed the constraining capabilities of non-parametric methods (GP) against standard parametric ones (CPL). Both CPL and GP always recover the injected cosmology. However, GP systematically provides better constraints with respect to CPL. In the case of MOD2, the constraints of GP are from 1.2 to 1.5 times tighter than CPL. For the ET $\Delta$ +CE+Pantheon+ configuration, the GP (CPL) provides the following constraints: for  $\Delta H_0/H_0$  we have 0.88% (1.4%); for  $\Delta\Omega_m/\Omega_m$  we get 37% (43%); the relative FoM is 2.8% (3.8%). Our model-independent approach is significantly more robust and less prone to biases in reconstructing the underlying cosmology;
- we explored the potential for joint analysis of next-generation GW data sets and future cosmological probes. By the time ET becomes operational, more precise data on  $\Omega_m$  will be available from sources such as SNIa observations from the Vera Rubin Observatory, Nancy Grace Roman Space Telescope, and BAO measurements from DESI (Y5) [158–161]. In particular, our analysis with DESI(Y5) indicates that the  $f_{DE}$  GP reconstruction can identify deviations from  $\Lambda$ CDM cosmology with a precision greater than  $2\sigma$  in the redshift range  $0.06 \lesssim z \lesssim 0.7$ ;
- we emphasized that obtaining significant insights into cosmology using bright sirens necessitates future generations of GW interferometers to be complemented by high-energy satellites capable of precise sky localization, similar to the combined efforts of *Fermi* and *Swift*. Additionally, a robust follow-up effort to ensure the redshift determination of events is crucial. As demonstrated by the improvements seen with the extended GRB catalog, even a few high-redshift data points can significantly enhance the constraining power. In the case of GP, the use of the extended catalog results in a 7.7% increase in precision for the ET $\Delta$ +CE + Pantheon+ case.

All our results are obtained under the most conservative assumptions. With just 38 GRBs with known redshift – that could be achieved in 4-5 years by an instrument such as THESEUS

– our method of analysis will enable to pinpoint at the percent level deviations from the  $\Lambda$ CDM expansion history. Furthermore, the methods and tools presented in this paper are highly flexible, so that they can easily be adapted to incorporate data catalogs from many other tracers of the distance-redshift relation. Upon publication of this paper, the devised likelihood pipelines will be publicly released, alongside all the mock data catalogs used in this work. The repository will be regularly updated with new catalogs coming from different  $H(z)$  tracers, such as, for instance, BBHs cross-correlated with LSS data<sup>14</sup>.

## Acknowledgements and data availability

We are very thankful to Biswajit Banerjee, Jan Harms, Samanta Macera, Simone Mastrogiovanni, Alessio Mei, Costantino Pacilio for useful discussions. We would also like to acknowledge all the participants to the [ModIC 2024 workshop](#) for the fruitful interdisciplinary exchange of ideas. In particular, we thank Eric V. Linder for helpful input on the treatment of peculiar velocities. We are thankful to the INFN Section, the University, and the Observatory of Cagliari (Sardinia) for their hospitality during the development of this project. Marica Branchesi acknowledges financial support from the Italian Ministry of University and Research (MUR) for the PRIN grant METE under contract no. 2020KB33TP. We also acknowledge the Director and the Computing and Network Service of Laboratori Nazionali del Gran Sasso (LNGS-INFN), and the high-performance computing cluster Seondeok at the Korea Astronomy and Space Science Institute. We acknowledge the use of `Matplotlib` [163], `NumPy` [164], `SciPy` [165], `AstroPy` [166]. The results of our analyses are fully reproducible by making use of publicly available catalogs of GRB archival data from [BRIGHT](#), [MPE GRB catalog](#), [GRBweb](#).

## A Full catalog of merger-driven GRBs with known redshift (circa 2024)

This Appendix is dedicated to a comparison of the results obtained considering different GRB catalogs classified according to their  $P_{cc}$ . The full catalog of GRBs considered in this work is presented in Table 2. As illustrated in the main text, we follow Ref. [66] and we provide three catalogs: the *fiducial* catalog (containing only those events with  $P_{cc} \leq 0.02$ ), the *extended* catalog (events with  $P_{cc} \leq 0.10$ ), and the *very extended* catalog ( $P_{cc} \leq 0.20$ ).

Concerning the GRB emission, its prompt  $\gamma$ /hard X-ray signal is emitted on-axis, beamed with an angle  $|\theta| \lesssim 10^\circ$  [67, 167], and followed by an optical/soft X-ray afterglow off-axis emission. The observational strategy to attribute a redshift to a GRB source is the following: the GRB event is firstly detected by a wide-field high-energy telescope, such as *Fermi*-GBM or *Swift*-BAT. The reconstructed sky localization ( $\approx$  arcmin) is then passed to a focusing instrument like *Swift*-XRT/UVOT, that constrain the GRB position with  $\approx$  arcsec precision, following the GRB afterglow emission [168]. The resulting sky position is finally passed to ground-based deep-field optical surveys, in order to identify the GRB host galaxy and measure its redshift, with a given uncertainty. The redshift of GRBs can also be determined using optical or near-infrared spectroscopy of their afterglow emission. In the local Universe ( $z \lesssim 0.6$ ) the off-axis GRB prompt emission [169] will provide the main contribution to the observed events, as clearly shown in [44]. On the contrary, the off-axis emission of GRBs

<sup>14</sup>Note that the likelihood in Eq. (3.2), while perfectly suitable to fit mock GW data as in this work, might lead to biased results when applied to real GW data (due *e.g.* to selection biases) [162]. Designing a likelihood encompassing all these effects is beyond the scope of this paper.

at higher redshift is too faint to be detected. In general, not knowing a priori the true value of the GRB inclination angle is a crucial source of uncertainty, due to its intrinsic degeneracy with the luminosity distance  $d_L$  [170, 171], and consequently with  $H_0$ . Therefore, the prior choice on the inclination angle can in principle bias the  $H_0$  estimate. This problem can be addressed properly as explained in Refs. [148, 172, 173]. Our results, however, are completely unaffected: our pipeline effectively removes this degeneracy, ensuring that any shift from the true  $H_0$  value is not due to this issue. We always have explicitly checked that the inferred  $H_0$  is consistent with the injected one. An additional source of uncertainty is related to the GRB-host galaxy association, and typically parameterized via the so-called probability of chance coincidence ( $P_{cc}$ ), that encodes the probability of a wrong association [174]. In Figure 15 we display this information as a function of  $z$  and categorizing the GRBs in our data set.

In Figure 16 we display the comparison of the constraining capabilities of the three different catalog of mock data for a fixed detector configuration. We show the ET $\Delta$  and the ET2L configurations in the case of a  $\Lambda$ CDM fit over MOD1 mock data. The difference in the constraining power is mainly present between the fiducial and the extended catalogs and must be sought in the addition of three GRB events at  $z > 2$  (Figure 15). We quote the following FoM for the ET $\Delta$  configuration:  $\tilde{\epsilon}_f = 2.1\%$   $\tilde{\epsilon}_e = 1.8\%$   $\tilde{\epsilon}_{ve} = 1.7\%$  for fiducial extended and very extended, respectively. More details can be found in Appendix C, Figure 24 and Table 3. We can see that the additional information given by more extended catalogs will not drastically change the results. This is a clear sign on how important are the high  $z$  GRBs for constraining the expansion history of the Universe. We report the same type of analysis in the case of a CPL fit over MOD1 mock data. This is shown in Figure 17. We quote the following FoM for the ET $\Delta$  configuration:  $\tilde{\epsilon}_f = 6.3\%$   $\tilde{\epsilon}_e = 6.1\%$   $\tilde{\epsilon}_{ve} = 5.9\%$ . The details are reported in Appendix C, Figure 25 and Table 4. We can observe that the CPL constraints do not significantly improve from one catalog to another. Finally, Figure 18 shows the GP fit over MOD1 mock data for the fiducial and extend catalogs. We quote the following FoM for the ET $\Delta$  configuration:  $\tilde{\epsilon}_f = 4.6\%$   $\tilde{\epsilon}_e = 4.2\%$ . We can appreciate a good improvement from the fiducial to the extended catalog and a general shrink of the contours with respect to CPL. The details are reported in Appendix C, Figure 26 and Table 5. We suggest the reader to refer to the main text for a more detailed illustration of the analysis implications.

**Table 2.** Full catalog of 61 GRBs from BNS mergers measured by *Fermi*-GBM and *Swift*-BAT/XRT with an uncertainty  $< 7\%$ . The event marked with a \* was discovered by HETE-2 [175]. The GRBs are sorted in chronological order. The first column contains the GRB name. The second column contains the GRB type.  $T_0$  represents the UTC time of the event trigger. R.A. and DEC. are the two angles specifying the sky position, namely right ascension and declination, respectively. The  $T_{90}$  column refers to the *Swift*-BAT/*Fermi*-GBM time interval over which 90% of the gamma-ray emission is measured. The  $z$  column contains the redshift of the objects. The catalog association column refers to the three different catalog used in this paper and it is directly connected to the  $P_{cc}$  column, representing the probability of chance coincidence from [66]. Events marked with an apex  $a$ , although having  $T_{90} \gtrsim 2$  s, are also classified as sGRB, accordingly to Refs. [66, 176]. Redshifts marked with an apex  $p$  are determined through photometry.

GRB name	GRB class	$T_0$ [UTC]	R.A. [deg]	DEC. [deg]	$T_{90}$ [s]	$z$	Catalog association	$P_{cc}$
GRB050509B	sGRB	4:00:19	189.06	28.98	0.073	0.23	fiducial	5e-3
GRB050709A	sGRB*	22:36:37	23.03	-38.99	0.070	0.16	fiducial	3e-3
GRB050724A	sGRB+E.E.	12:34:09	246.18	-27.54	98	0.25	fiducial	2e-5
GRB050813A	sGRB	6:45:10	241.99	11.25	0.45	0.72	very extended	2e-1
GRB051221A	sGRB <sup>p</sup>	5:46:21	330.17	-57.61	1.3	2.6	extended	4e-2
GRB051221A	sGRB	1:51:16	328.70	16.89	1.4	0.55	fiducial	5e-5
GRB060614A	sGRB+E.E.	12:43:49	320.88	-53.03	110	0.13	fiducial	3e-4
GRB060801A	sGRB	12:16:15	213.01	16.98	0.49	1.1	fiducial	2e-2
GRB061006A	sGRB+E.E.	16:45:51	111.03	-79.20	130	0.46	fiducial	4e-4
GRB061210A	sGRB+E.E.	12:20:39	144.52	15.61	85	0.41	fiducial	2e-2
GRB070429B	sGRB	3:09:04	328.02	-38.83	0.47	0.90	fiducial	3e-3
GRB070714B	sGRB+E.E.	4:59:29	57.84	28.30	64.0	0.92	fiducial	5e-3
GRB070724A	sGRB	10:53:50	27.81	-18.59	0.40	0.46	fiducial	8e-4
GRB070809A	sGRB	19:22:17	203.77	-22.12	1.3	0.47	fiducial	6e-3
GRB071227A	sGRB	20:13:47	58.13	-55.98	1.8	0.38	fiducial	1e-2
GRB080123A	sGRB+E.E.	4:21:57	338.94	-64.90	110	0.50	very extended	1.1e-1
GRB080905A	sGRB	11:58:54	287.67	-18.88	0.96	0.12	fiducial	1e-2
GRB090426A	sGRB	12:48:47	189.08	32.99	1.2	2.6	fiducial	1.5e-4
GRB090510A	sGRB	0:22:59	333.55	-26.58	0.96	0.90	fiducial	8e-3
GRB090515A	sGRB	4:45:09	164.15	14.44	0.036	0.40	extended	5e-2
GRB100117A	sGRB	21:06:19	11.27	-1.59	0.26	0.92	fiducial	7e-5
GRB100206A	sGRB	13:30:05	47.16	13.16	0.18	0.41	fiducial	2e-2
GRB100625A	sGRB	18:32:27	15.80	-39.09	0.24	0.45	extended	4e-2
GRB101219A	sGRB	2:31:29	74.59	-2.54	0.60	0.72	extended	6e-2
GRB101224A	sGRB	5:27:13	285.92	45.71	1.7	0.45	fiducial	1.5e-2
GRB111117A	sGRB	12:13:41	12.70	23.02	0.43	2.2	extended	2.4e-2
GRB120305A	sGRB	19:37:30	47.54	28.49	0.10	0.23	extended	5.3e-2
GRB121226A	sGRB <sup>p</sup>	19:09:43	168.64	-30.41	1.0	1.4	fiducial	1.9e-2
GRB130515A	sGRB <sup>p</sup>	1:21:17	283.44	-54.28	0.26	0.80	extended	8.1e-2
GRB130603B	sGRB	15:49:14	172.20	17.07	0.18	0.36	fiducial	2e-3
GRB130822A	sGRB	15:54:17	27.92	-3.21	0.04	0.15	extended	8.6e-2
GRB131004A	sGRB	21:41:03	296.11	-2.96	1.2	0.72	extended	5.5e-2
GRB140129B	sGRB	12:51:09	326.76	26.21	1.4	0.43	fiducial	8.7e-4
GRB140622A	sGRB	9:36:04	317.17	-14.42	0.13	0.96	very extended	1e-1
GRB140903A	sGRB	15:00:30	238.01	27.60	0.30	0.35	fiducial	6.2e-5
GRB140930B	sGRB	19:41:42	6.35	24.29	0.84	1.5	extended	2.1e-2
GRB141212A	sGRB	12:14:01	39.12	18.15	0.3	0.60	fiducial	2.9e-4
GRB150101B	sGRB	15:23:00	188.02	-10.93	0.08	0.13	fiducial	4.8e-4
GRB150120A	sGRB <sup>a</sup>	2:57:46	10.32	33.99	3.3	0.46	fiducial	1.9e-3
GRB150728A	sGRB	12:51:11	292.23	33.92	0.83	0.46	fiducial	1.8e-2
GRB150831A	sGRB	10:34:09	221.02	-25.63	1.2	1.2	extended	3.7e-2
GRB160624A	sGRB	11:27:01	30.19	29.64	0.38	0.48	extended	3.7e-2
GRB160821B	sGRB	22:29:13	279.98	62.39	1.1	0.16	extended	4.4e-2
GRB161001A	sGRB <sup>a</sup>	1:05:16	71.92	-57.26	2.6	0.67	extended	4.5e-2
GRB161104A	sGRB	9:42:26	77.89	-51.46	0.10	0.79	very extended	6e-2
GRB170127B	sGRB	15:13:28	19.98	-30.36	1.7	2.3	extended	9.8e-2
GRB170428A	sGRB	9:13:38	330.08	26.92	0.20	0.45	fiducial	6.7e-3
GRB170728A	sGRB	6:53:28	58.89	12.18	1.3	1.5	very extended	2.2e-1
GRB170728B	sGRB+E.E.	23:03:18	237.98	70.12	47.7	1.27	fiducial	8.3e-3
GRB170817A	GRB+KN	12:41:06	13.16	-23.38	2.6	0.010	fiducial	4.9e-4
GRB180805B	sGRB	13:02:36	25.78	-17.49	0.96	0.66	extended	4.2e-2
GRB181123B	sGRB	5:33:03	184.37	14.60	0.26	1.75	fiducial	4.4e-3
GRB191019A	SNless 1GRB	15:12:33	340.02	-17.33	64	0.25	fiducial	-
GRB200219A	sGRB <sup>p</sup>	7:36:45	342.64	-59.12	1.2	0.48	fiducial	2.2e-3
GRB200522A	sGRB	11:41:34	5.68	-0.28	0.62	0.55	fiducial	3.5e-5
GRB201221D	sGRB	23:06:34	171.06	42.14	0.14	1.05	very extended	1.2e-1
GRB210323A	sGRB	22:02:14	317.95	25.37	0.96	0.73	fiducial	1.3e-2
GRB210919A	sGRB	0:28:33	80.25	1.31	0.16	0.24	very extended	1.3e-1
GRB211023B	sGRB	21:05:52	170.31	39.14	1.3	0.86	fiducial	4.7e-3
GRB211211A	GRB+KN	13:09:59	212.29	27.89	34	0.076	fiducial	1.4e-2
GRB230307A	GRB+KN	15:44:05	60.82	-75.38	35	0.065	fiducial	-

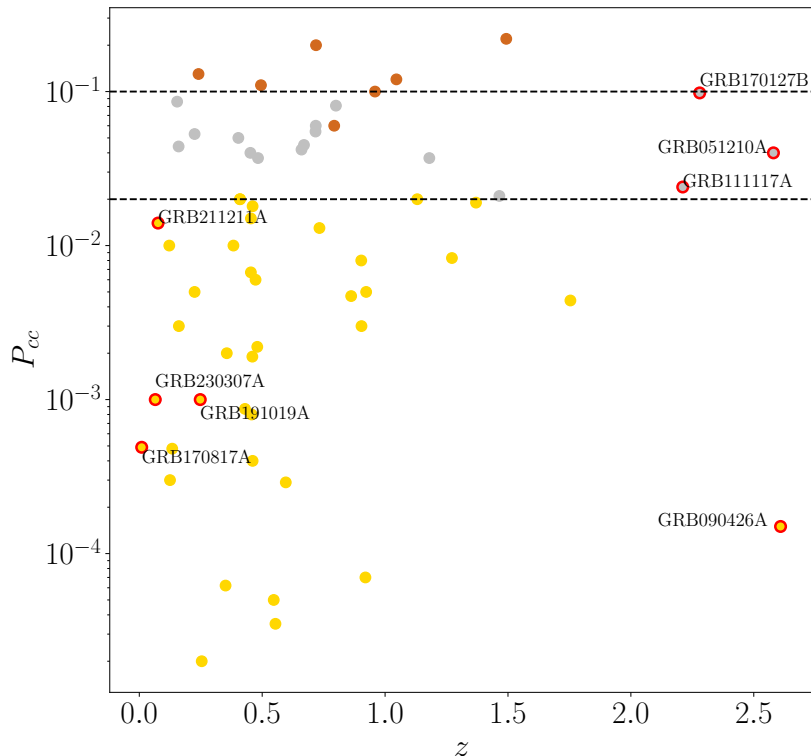


**Figure 15.** The probability of chance coincidence distribution (see main text) as a function of redshift. GRB datapoints are organized by color following [66] categorization. The points under the lower dashed line represent our fiducial 38 events catalog. The ones residing under the upper dashed line compose the extended 54 events catalog. All together they compose the very extended 61 event catalog. In the left part we have circled some of the most important GRBs like the three associated to a KN event and the SNless long GRB. In the right part we can find the furthest GRB event of our catalog at  $z = 2.609$  and three GRB that, even if associated with a small  $P_{cc}$  value, can be crucial in the high- $z$  region to constrain the expansion history.

## B Full comparison among GW detector configurations

This Appendix is dedicated to comparing the results obtained from an extensive analysis of all GW detector configurations. In this cases, we focus on the fiducial GRB catalog. The Appendix is structured as follows: we present the results for the  $\Lambda$ CDM, CPL and GP fitting models over a MOD1 Universe. For each scenario, we provide a comparison of contours between 2G and 3G detectors (if not already shown in the main text), along with an analysis involving combinations of Pantheon+ and GW detectors, as well as various configurations of 3G detectors.

In Figure 19 we compare different configuration for a  $\Lambda$ CDM fit over MOD1. A clear improvement respect with LVK+Pantheon+ joint analysis can be perceived. We can observe some general features: the ET2L configuration performs better than the ET $\Delta$  ( $\tilde{\epsilon}_{\text{ET}\Delta} = 2.1\%$   $\tilde{\epsilon}_{\text{ET2L}} = 1.9\%$ ). The HF configurations present comparable results respect with their full cryogenic configurations (left panel of Figure 19). In the case of ET $\Delta$ (2L) the uncertainty on  $H_0$  is 1.3%(1.2%) while the ETHF $\Delta$ (2L) configuration obtain 1.7%(1.4%). The difference increases in the case of  $\Omega_m$  constraints: ET $\Delta$ (2L) the uncertainty on  $\Omega_m$  is 22%(19%) while the



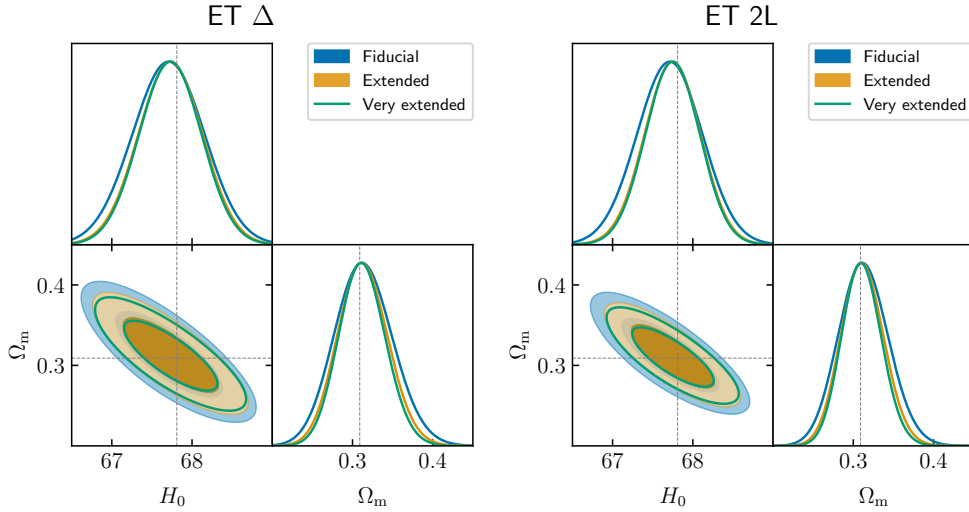


**Figure 16.**  $\Lambda$ CDM constraints (1- and 2- $\sigma$  C.L.) on the relevant cosmological parameters, obtained by fitting the underlying MOD1 cosmology. Comparison on the constrains obtained by the three GRB catalogs with ET $\Delta$  (*left*) and ET2L (*right*).

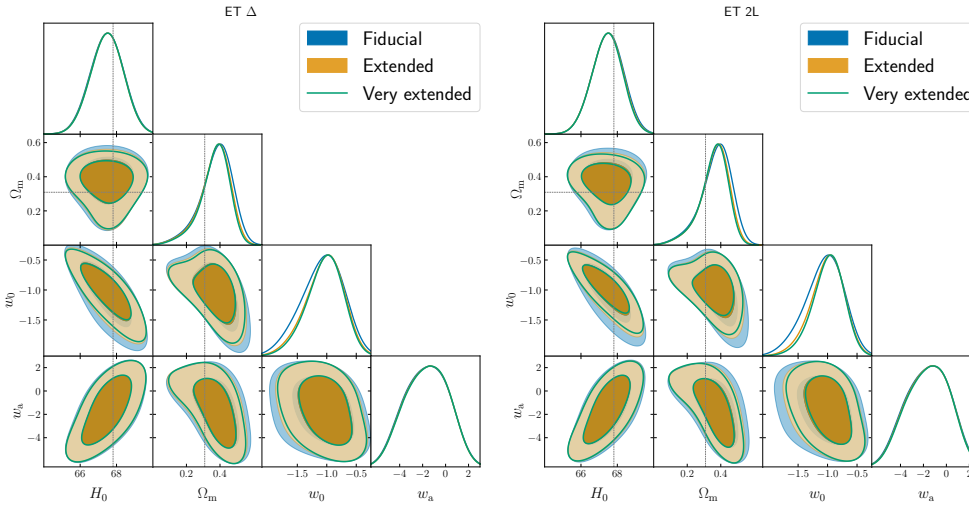


**Figure 17.** CPL constraints (1- and 2- $\sigma$  C.L.) on the relevant cosmological parameters, obtained by fitting the underlying MOD1 cosmology. Comparison on the constrains obtained by the three GRB catalogs with ET $\Delta$  (*left*) and ET2L (*right*).

ETHF $\Delta$ (2L) configuration obtain 33%(25%). The FoM are  $\tilde{\epsilon}_{\text{ETHF}\Delta} = 2.9\%$   $\tilde{\epsilon}_{\text{ETHF}2\text{L}} = 2.3\%$ . In the right panel of Figure 19 we report the comparison with and without the CE detector. The FoM improves as follows  $\tilde{\epsilon}_{\text{ET}\Delta+\text{CE}} = 1.4\%$   $\tilde{\epsilon}_{\text{ET}2\text{L}+\text{CE}} = 1.3\%$ . The all set of results is presented in Appendix C, Figure 24 and Table 3

In Figure 20 we show the constraints obtained by fitting CPL over the MOD1 data set. In the left panel we can see again how 3G detector outperform 2G detectors. We report the FoM of the three showed configurations, namely  $\tilde{\epsilon}_{\text{LVK}} = 16\%$   $\tilde{\epsilon}_{\text{LVKIA}\#} = 12\%$   $\tilde{\epsilon}_{\text{ET}\Delta} = 6.3\%$ . In the right panel instead, we show the results obtained with the Pantheon+ combination. We report an improvement quantified by the FoM as follows:  $\tilde{\epsilon}_{\text{PP+LVK}} = 8.3\%$ ,  $\tilde{\epsilon}_{\text{PP+ET}\Delta} = 4.5\%$ .

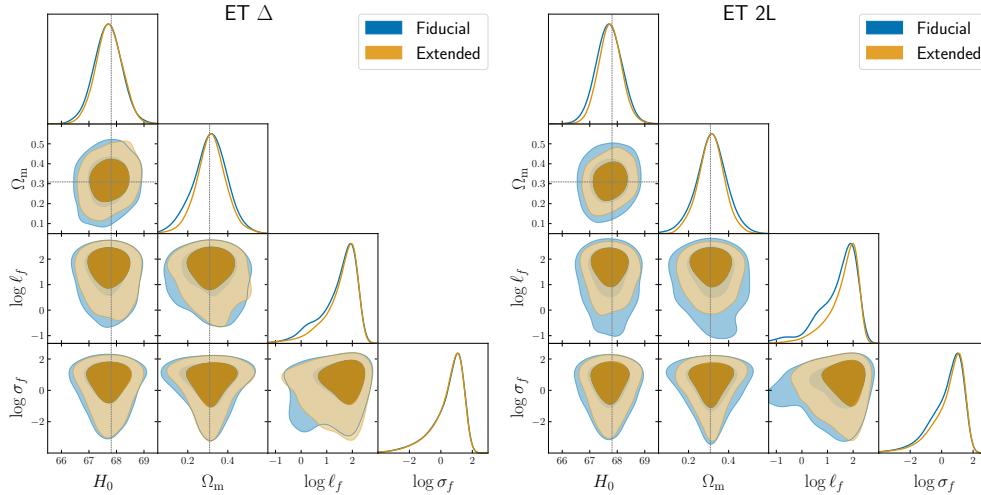


**Figure 18.** GP constraints (1- and 2- $\sigma$  C.L.) on the relevant cosmological parameters, obtained by fitting the underlying MOD1 cosmology. Comparison on the constrains obtained by the three GRB catalogs with ET $\Delta$  (*left*) and ET2L (*right*).

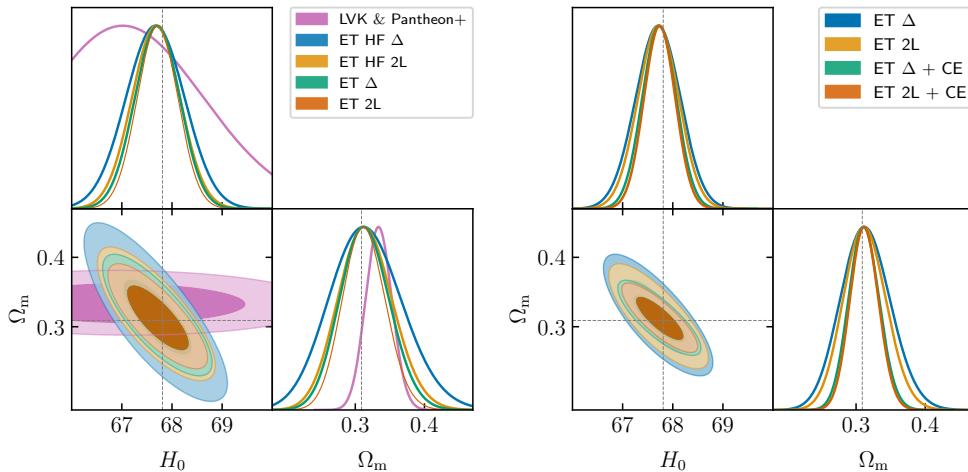


**Figure 19.**  $\Lambda$ CDM constraints (1- and 2- $\sigma$  C.L.) on the relevant cosmological parameters, obtained by fitting the underlying MOD1 cosmology. (*Left*) Comparison of the cosmological constraints obtained by LVK+Pantheon+, the ET HF  $\Delta$ /2L and ET $\Delta$ /2L configurations. (*Right*) The comparison between ET $\Delta$ /2L and ET $\Delta$ /2L + CE.

Note the following interesting fact, in the right panel of Figure 20: in the  $w_0$ - $\Omega_m$  space the contours of ET $\Delta$ +Pantheon+ and LVK+Pantheon+ are equal. This means that the use of the Pantheon+ SNIa data set is driving the choice of  $w_0$  as a consequence of the better constraint on  $\Omega_m$ . The full  $2\sigma$  uncertainty on  $H_0$ ,  $\Omega_m$  and  $w_0$  are show in Figure 25 and Table 4 of Appendix C. We do not report the uncertainty on  $w_a$  because they derive unconstrained values for all the detector configurations and GRB catalogs.

In Figure 21, we delve into a comparison of various GW detector configurations. It is worth emphasizing once again the slight advantage of ET2L over ET $\Delta$ . However, with respect to the  $\Lambda$ CDM fit on MOD1, transitioning to the CPL scenario reveals a noticeable decline

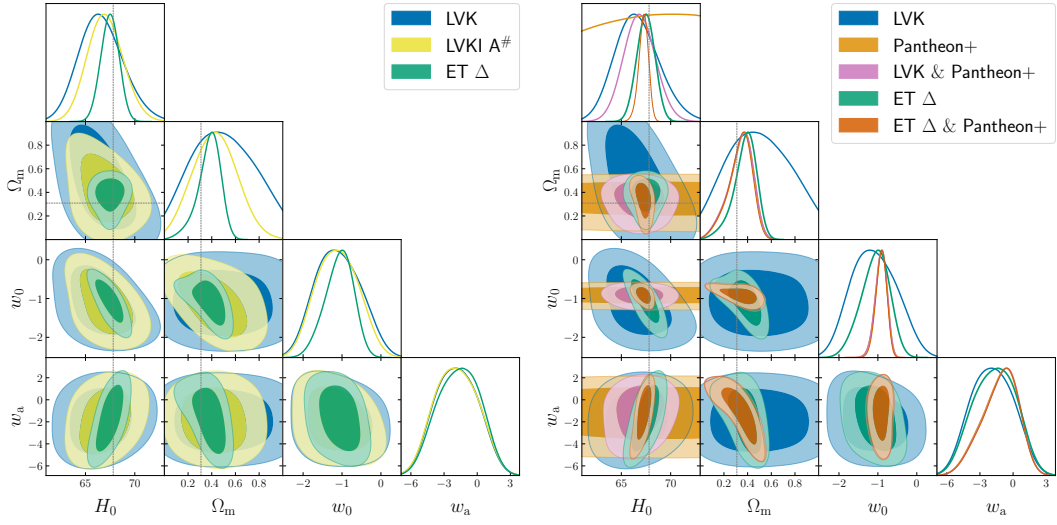


**Figure 20.** CPL constraints (1- and 2- $\sigma$  C.L.) on relevant cosmological parameters, obtained by fitting the underlying MOD1 cosmology. (*Left*) Comparison between LVK (O5) (blue) and ET $\Delta$  (green). (*Right*) As in the left panel but over-plotting the constraints obtained with the Pantheon+ data set alone (orange) and in a joint analysis with LVK (O5) (pink).

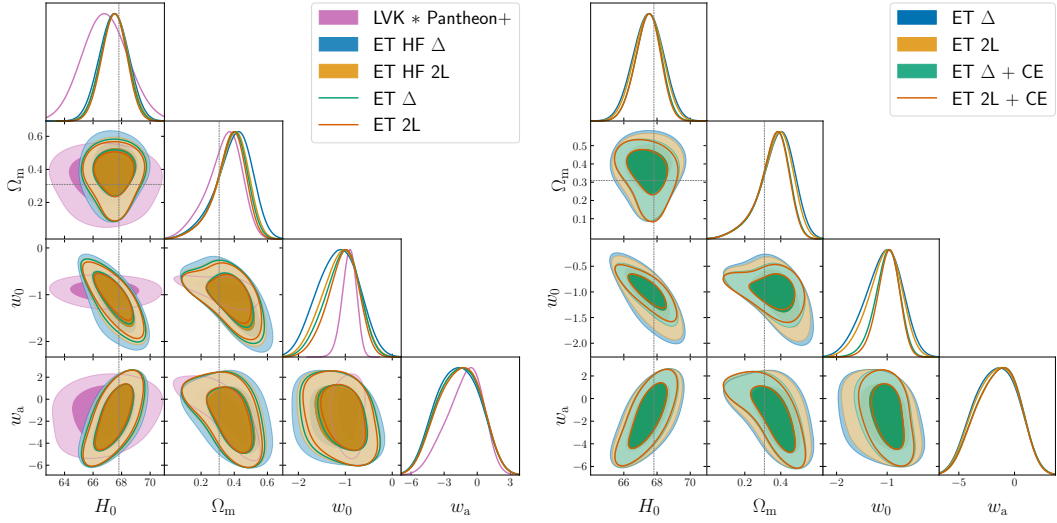


**Figure 21.** CPL constraints (1- and 2- $\sigma$  C.L.) on the relevant cosmological parameters, obtained by fitting the underlying MOD1 cosmology. (*Left*) Comparison of the cosmological constraints obtained by LVK+Pantheon+, the ET HF  $\Delta$ /2L and ET $\Delta$ /2L configurations. (*Right*) The comparison between ET $\Delta$ /2L and ET $\Delta$ /2L + CE.

in constraining power, attributed to the wider parameter space explored. The relative FoMs read:  $\tilde{\epsilon}_{\text{ETHF}\Delta} = 7.1\%$ ,  $\tilde{\epsilon}_{\text{ET}\Delta} = 6.3\%$ ,  $\tilde{\epsilon}_{\text{ET}\Delta+\text{CE}} = 6.2\%$  and  $\tilde{\epsilon}_{\text{ETHF}2\text{L}} = 6.5\%$ ,  $\tilde{\epsilon}_{\text{ET}2\text{L}} = 6.0\%$ ,  $\tilde{\epsilon}_{\text{ET}2\text{L}+\text{CE}} = 5.3\%$

Finally, we report the GP comparison among GW detectors with a MOD1 underlying cosmology. In the left panel of Figure 22 we report 2G and 3G detector comparison. The FoMs for the configurations reported in the Figure reads  $\tilde{\epsilon}_{\text{LVK}} = 14.5\%$   $\tilde{\epsilon}_{\text{LVKIA}\#} = 10.6\%$

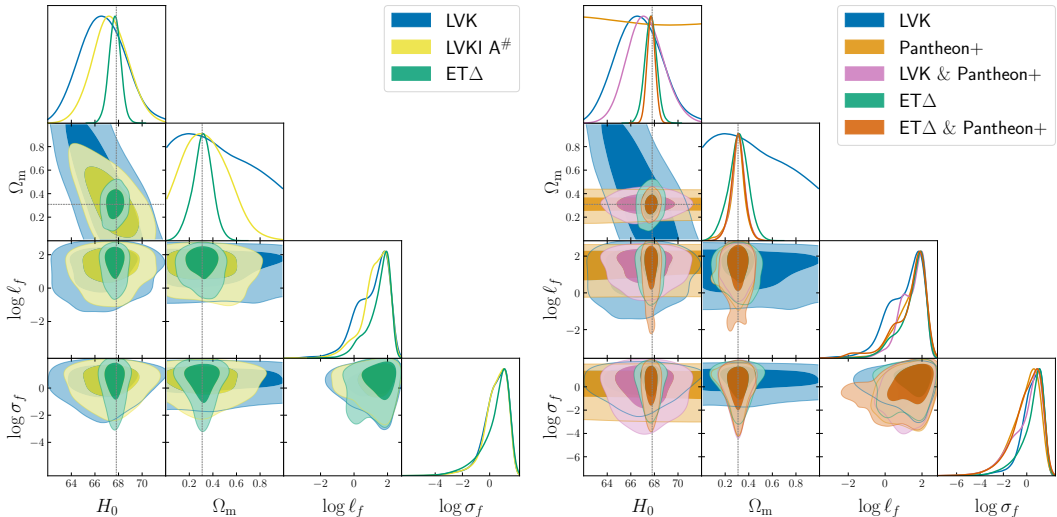


**Figure 22.** GP constraints (1- and 2- $\sigma$  C.L.) on relevant cosmological parameters, obtained by fitting the underlying MOD1 cosmology. (*Left*) Comparison between LVK (O5) (blue) and ET $\Delta$  (green). (*Right*) As in the left panel but over-plotting the constraints obtained with the Pantheon+ data set alone (orange) and in a joint analysis with LVK (O5) (pink).

$\tilde{\epsilon}_{\text{ET}\Delta} = 4.6\%$ . In the left panel of Figure 22 we report the Pantheon+ calibration with GW. The resulting FoMs are  $\tilde{\epsilon}_{\text{PP+LVK}} = 6.7\%$ ,  $\tilde{\epsilon}_{\text{PP+ET}\Delta} = 3.0\%$ . The comparison among 3G detectors different configurations is instead reported in Figure 23. The associated FoMs read  $\tilde{\epsilon}_{\text{ET}\Delta} = 4.6\%$ ,  $\tilde{\epsilon}_{\text{ET}\Delta+\text{CE}} = 3.5\%$  and  $\tilde{\epsilon}_{\text{ET}2\text{L}} = 4.2\%$ ,  $\tilde{\epsilon}_{\text{ET}2\text{L}+\text{CE}} = 3.4\%$ . We disclose a consistent improvement with respect to CPL, as already underlined in the main text. The complete results are reported in Appendix C, Figure 26 and Table 5.

## C Further tables and plots

This Appendix is dedicated to display plots and tables accompanying or completing the results found in the main text and the previous appendices. We report the results for the  $\Lambda$ CDM, CPL and GP fit over MOD1 in Figures 24, 25 and 26, respectively. The condensed numbers associated to these can be found in Tables 3, 4 and 5. The same is done for MOD2 in Figures 27, 28, 29 and Tables 6, 7 and 8.

In Figure 30 we present the  $H_0$ - $\Omega_m$  contours from a  $\Lambda$ CDM fit on MOD1, using the ET $\Delta$ +CE configuration. This figure illustrates how the constraints vary by adjusting the redshift threshold applied for the peculiar velocity correction, as discussed in Subsection 2.1. It is evident that the contours cease to expand when the threshold is set at  $z \sim 0.15$ , which is why we selected this threshold for use throughout the paper. Notably, neglecting the proper peculiar velocity correction would result in significantly smaller contours compared to those that include the correction. In Figure 31 we compare different BNS mass distributions, specifically examining the ET $\Delta$  configuration for the fiducial catalog. The uniform distribution refers to a dataset generated by uniformly sampling BNS masses in the range of 1.1 to 2.1  $M_\odot$ . In contrast, the Gaussian distribution represents a dataset generated by drawing masses from a normal distribution with a mean of 1.33  $M_\odot$  and a standard deviation of 0.09  $M_\odot$  [149]. The differences in the constraints are minimal and primarily driven by different

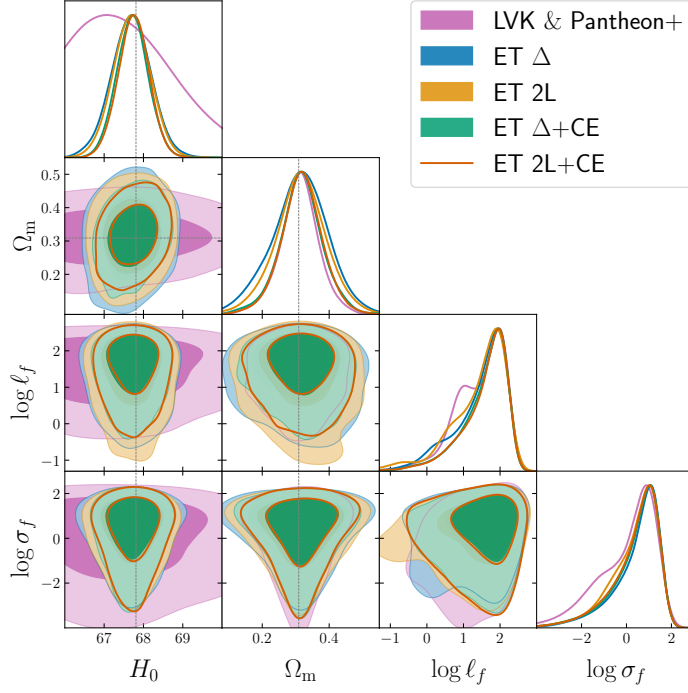


**Figure 23.** GP constraints (1- and 2- $\sigma$  C.L.) on the relevant cosmological parameters, obtained by fitting the underlying MOD1 cosmology. (*Left*) Comparison of the cosmological constraints obtained by LVK+Pantheon+, the ET HF  $\Delta$ /2L and ET $\Delta$ /2L configurations. (*Right*) The comparison between ET $\Delta$ /2L and ET $\Delta$ /2L + CE.

**Table 3.** MOD1 |  $\Lambda$ CDM fit

Data set	Fiducial			Extended			Very extended		
	$\frac{\Delta H_0}{H_0}$	$\frac{\Delta \Omega_m}{\Omega_m}$	$\tilde{\epsilon}$	$\frac{\Delta H_0}{H_0}$	$\frac{\Delta \Omega_m}{\Omega_m}$	$\tilde{\epsilon}$	$\frac{\Delta H_0}{H_0}$	$\frac{\Delta \Omega_m}{\Omega_m}$	$\tilde{\epsilon}$
Pantheon+ & BAO	0.019	0.04	0.011	–	–	–	–	–	–
Pantheon+ & SH <sub>0</sub> ES	0.032	0.11	0.03	–	–	–	–	–	–
Pantheon+ & LVK (O5)	0.045	0.11	0.036	–	–	–	–	–	–
Pantheon+ & ET $\Delta$	0.0091	0.1	0.014	0.0082	0.098	0.0086	–	–	–
Pantheon+ & ET $\Delta$ +CE	0.0075	0.088	0.011	0.0066	0.081	0.0072	–	–	–
LVK (O5)	0.055	1.8	0.14	0.055	1.8	0.14	0.055	1.8	0.14
LVKI A#	0.044	1.1	0.084	0.043	1.1	0.08	0.043	1.0	0.078
ET HF $\Delta$	0.017	0.33	0.029	0.015	0.29	0.025	0.015	0.28	0.025
ET $\Delta$	0.013	0.22	0.021	0.011	0.19	0.018	0.011	0.18	0.017
ET $\Delta$ + CE	0.0096	0.14	0.014	0.0081	0.11	0.012	0.0079	0.11	0.011
ET HF 2L	0.014	0.25	0.023	0.012	0.22	0.02	0.012	0.2	0.019
ET2L	0.012	0.19	0.019	0.0098	0.17	0.016	0.0096	0.15	0.015
ET2L + CE	0.0088	0.13	0.013	0.0075	0.11	0.011	0.0073	0.1	0.01

number of detected events. In the case of the Gaussian mass distribution, the number of detected events is reduced to 33, compared to 36 events for the uniform distribution.

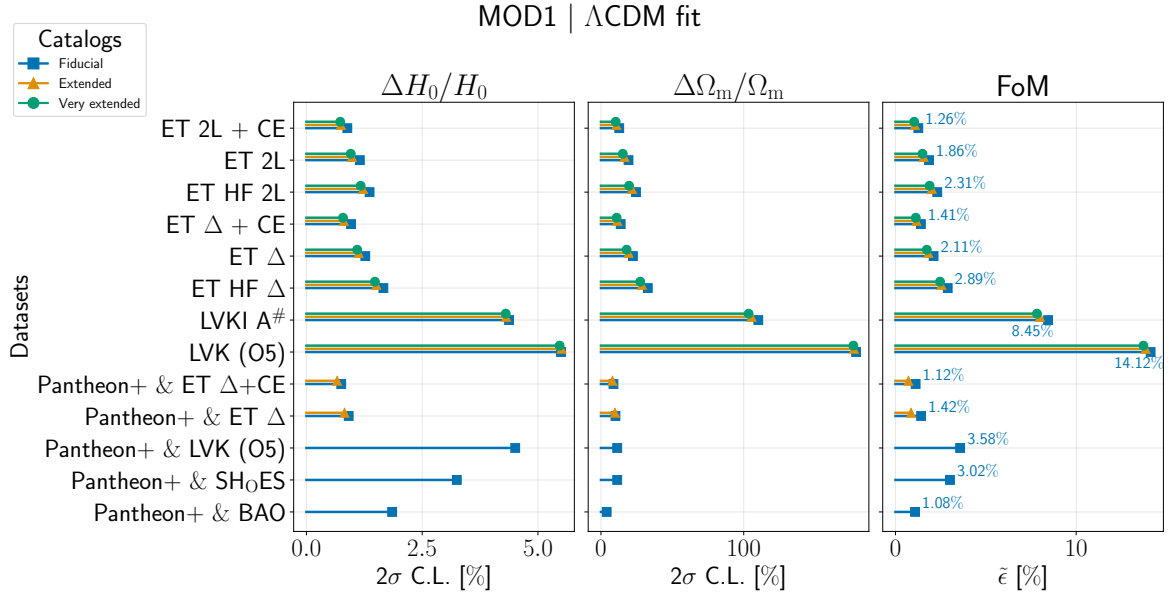


**Figure 24.**  $\Lambda$ CDM  $2\sigma$  relative error on  $H_0$  and  $\Omega_m$  for an underlying MOD1 cosmology. The last panel presents the relative FoM. The associated values can be found Table 3.

**Table 4.** MOD1 | CPL fit

Data set	Fiducial				Extended				Very extended			
	$\frac{\Delta H_0}{H_0}$	$\frac{\Delta \Omega_m}{\Omega_m}$	$\frac{\Delta w_0}{w_0}$	$\tilde{\epsilon}$	$\frac{\Delta H_0}{H_0}$	$\frac{\Delta \Omega_m}{\Omega_m}$	$\frac{\Delta w_0}{w_0}$	$\tilde{\epsilon}$	$\frac{\Delta H_0}{H_0}$	$\frac{\Delta \Omega_m}{\Omega_m}$	$\frac{\Delta w_0}{w_0}$	$\tilde{\epsilon}$
Pantheon+ & LVK (O5)	0.046	0.61	0.31	0.083	–	–	–	–	–	–	–	–
Pantheon+ & ET $\Delta$	0.014	0.6	0.29	0.045	0.013	0.59	0.28	0.044	–	–	–	–
Pantheon+ & ET $\Delta$ +CE	0.012	0.58	0.26	0.044	0.012	0.54	0.24	0.039	–	–	–	–
LVK (O5)	0.064	1.8	1.1	0.16	0.064	1.7	1.1	0.15	0.064	1.7	1.1	0.15
LVKI A#	0.051	1.2	1.0	0.12	0.051	1.1	1.0	0.12	0.051	1.1	1.0	0.12
ET HF $\Delta$	0.029	0.69	0.84	0.071	0.029	0.66	0.79	0.069	0.029	0.65	0.78	0.068
ET $\Delta$	0.026	0.61	0.7	0.063	0.026	0.57	0.62	0.061	0.026	0.55	0.6	0.059
ET $\Delta$ + CE	0.022	0.54	0.47	0.062	0.021	0.51	0.39	0.051	0.021	0.5	0.38	0.05
ET HF 2L	0.027	0.62	0.74	0.065	0.027	0.59	0.68	0.062	0.026	0.56	0.64	0.061
ET2L	0.025	0.59	0.64	0.06	0.024	0.54	0.55	0.057	0.024	0.53	0.52	0.056
ET2L + CE	0.021	0.54	0.42	0.053	0.021	0.5	0.37	0.049	0.02	0.5	0.36	0.049

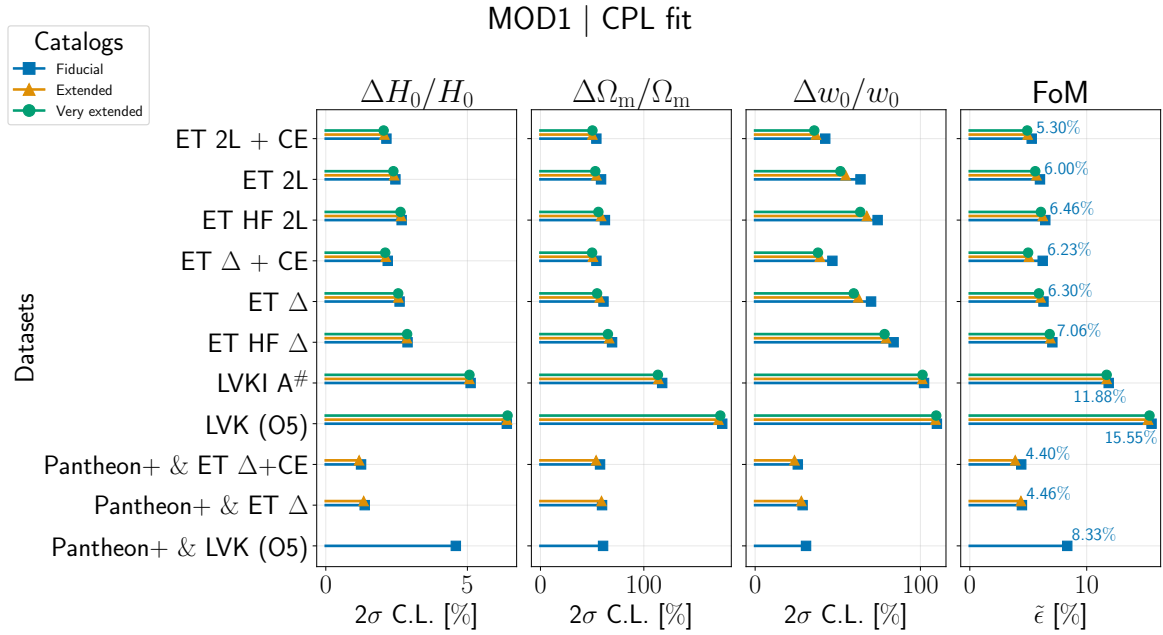


**Figure 25.** CPL  $2\sigma$  relative error on  $H_0$ ,  $\Omega_m$  and  $w_0$  for an underlying MOD1 cosmology. The last panel presents the relative FoM. The associated values can be found Table 4.

**Table 5.** MOD1 | GP fit

Data set	Fiducial			Extended		
	$\frac{\Delta H_0}{H_0}$	$\frac{\Delta \Omega_m}{\Omega_m}$	$\tilde{\epsilon}$	$\frac{\Delta H_0}{H_0}$	$\frac{\Delta \Omega_m}{\Omega_m}$	$\tilde{\epsilon}$
Pantheon+ & LVK(O5)	0.044	0.4	0.067	0.041	0.4	0.064
Pantheon+ & ET $\Delta$	0.0097	0.4	0.03	0.0089	0.38	0.029
Pantheon+ & ET $\Delta$ + CE	0.0082	0.32	0.025	0.0077	0.32	0.024
Pantheon+ & ET 2L	0.009	0.41	0.031	0.0083	0.37	0.027
Pantheon+ & ET 2L + CE	0.008	0.35	0.026	0.0074	0.31	0.024
LVK(O5)	0.055	1.8	0.15	0.057	1.8	0.14
LVKI A#	0.044	1.3	0.11	0.043	1.3	0.1
ET $\Delta$	0.015	0.58	0.046	0.014	0.52	0.042
ET $\Delta$ + CE	0.012	0.45	0.035	0.01	0.37	0.031
ET 2L	0.014	0.53	0.042	0.012	0.45	0.036
ET 2L + CE	0.011	0.43	0.034	0.0098	0.38	0.029

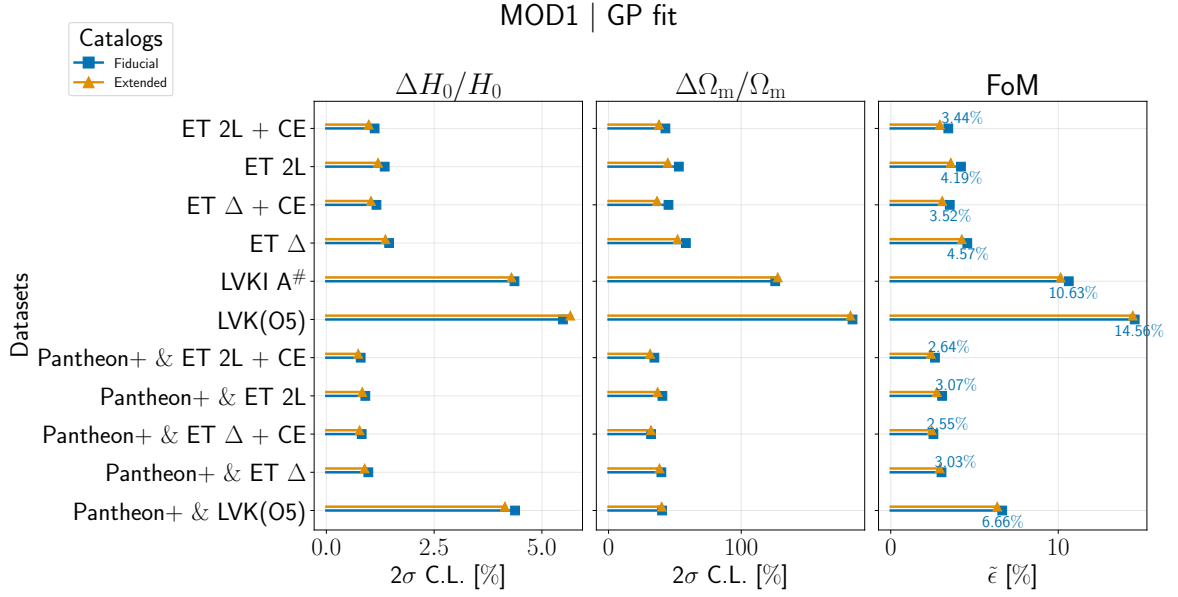


**Figure 26.** GP  $2\sigma$  relative error on  $H_0$  and  $\Omega_m$  for an underlying MOD1 cosmology. The last panel presents the relative FoM. The associated values can be found Table 5.

**Table 6.** MOD2 | PEDE fit

Data set	Fiducial			Extended			Very extended		
	$\frac{\Delta H_0}{H_0}$	$\frac{\Delta \Omega_m}{\Omega_m}$	$\tilde{\epsilon}$	$\frac{\Delta H_0}{H_0}$	$\frac{\Delta \Omega_m}{\Omega_m}$	$\tilde{\epsilon}$	$\frac{\Delta H_0}{H_0}$	$\frac{\Delta \Omega_m}{\Omega_m}$	$\tilde{\epsilon}$
Pantheon+ & BAO	0.019	0.04	0.012	–	–	–	–	–	–
Pantheon+ & SH <sub>0</sub> ES	0.032	0.1	0.028	–	–	–	–	–	–
Pantheon+ & LVK (O5)	0.044	0.1	0.033	–	–	–	–	–	–
Pantheon+ & ET $\Delta$	0.009	0.09	0.013	0.0081	0.088	0.0087	–	–	–
Pantheon+ & ET $\Delta$ +CE	0.0075	0.078	0.011	0.0066	0.072	0.0073	–	–	–
LVK (O5)	0.057	1.8	0.14	0.057	1.8	0.14	0.057	1.8	0.14
LVKI A#	0.044	0.98	0.079	0.043	0.94	0.075	0.042	0.92	0.073
ET HF $\Delta$	0.016	0.28	0.026	0.015	0.25	0.023	0.015	0.24	0.023
ET $\Delta$	0.013	0.2	0.02	0.011	0.17	0.017	0.011	0.16	0.016
ET $\Delta$ + CE	0.0095	0.12	0.013	0.0079	0.1	0.011	0.0078	0.097	0.01
ET HF 2L	0.013	0.22	0.021	0.012	0.19	0.018	0.011	0.17	0.018
ET2L	0.011	0.17	0.017	0.0096	0.14	0.014	0.0093	0.13	0.014
ET2L + CE	0.0088	0.11	0.012	0.0074	0.096	0.01	0.0072	0.092	0.0097



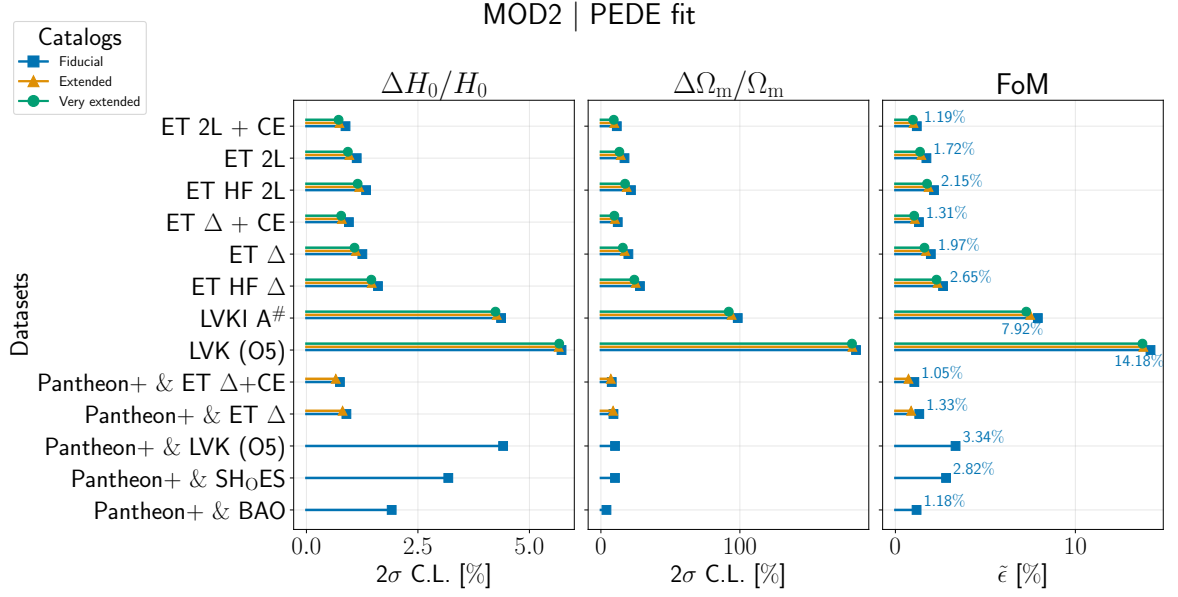


**Figure 27.** PEDE  $2\sigma$  relative error on  $H_0$  and  $\Omega_m$  for an underlying MOD2 cosmology. The last panel presents the relative FoM. The associated values can be found Table 6.

**Table 7.** MOD2 | CPL fit

Data set	Fiducial				Extended				Very extended			
	$\frac{\Delta H_0}{H_0}$	$\frac{\Delta \Omega_m}{\Omega_m}$	$\frac{\Delta w_0}{w_0}$	$\tilde{\epsilon}$	$\frac{\Delta H_0}{H_0}$	$\frac{\Delta \Omega_m}{\Omega_m}$	$\frac{\Delta w_0}{w_0}$	$\tilde{\epsilon}$	$\frac{\Delta H_0}{H_0}$	$\frac{\Delta \Omega_m}{\Omega_m}$	$\frac{\Delta w_0}{w_0}$	$\tilde{\epsilon}$
Pantheon+ & LVK (O5)	0.045	0.45	0.28	0.071	–	–	–	–	–	–	–	–
Pantheon+ & ET $\Delta$	0.016	0.42	0.26	0.039	0.015	0.43	0.26	0.039	–	–	–	–
Pantheon+ & ET $\Delta$ +CE	0.014	0.43	0.24	0.038	0.014	0.4	0.22	0.035	–	–	–	–
LVK (O5)	0.064	1.8	1.1	0.16	0.064	1.8	1.1	0.16	0.064	1.8	1.1	0.16
LVKI A#	0.051	1.1	0.97	0.12	0.05	1.1	0.96	0.11	0.05	1.1	0.95	0.11
ET HF $\Delta$	0.03	0.65	0.76	0.069	0.029	0.62	0.73	0.068	0.029	0.62	0.72	0.067
ET $\Delta$	0.027	0.56	0.64	0.061	0.027	0.52	0.58	0.059	0.027	0.5	0.55	0.058
ET $\Delta$ + CE	0.023	0.48	0.44	0.052	0.023	0.44	0.38	0.049	0.023	0.41	0.37	0.046
ET HF 2L	0.028	0.58	0.68	0.063	0.028	0.52	0.61	0.06	0.027	0.51	0.59	0.059
ET2L	0.026	0.53	0.58	0.058	0.025	0.48	0.51	0.055	0.025	0.48	0.48	0.054
ET2L + CE	0.023	0.48	0.41	0.051	0.022	0.44	0.36	0.047	0.022	0.44	0.35	0.047

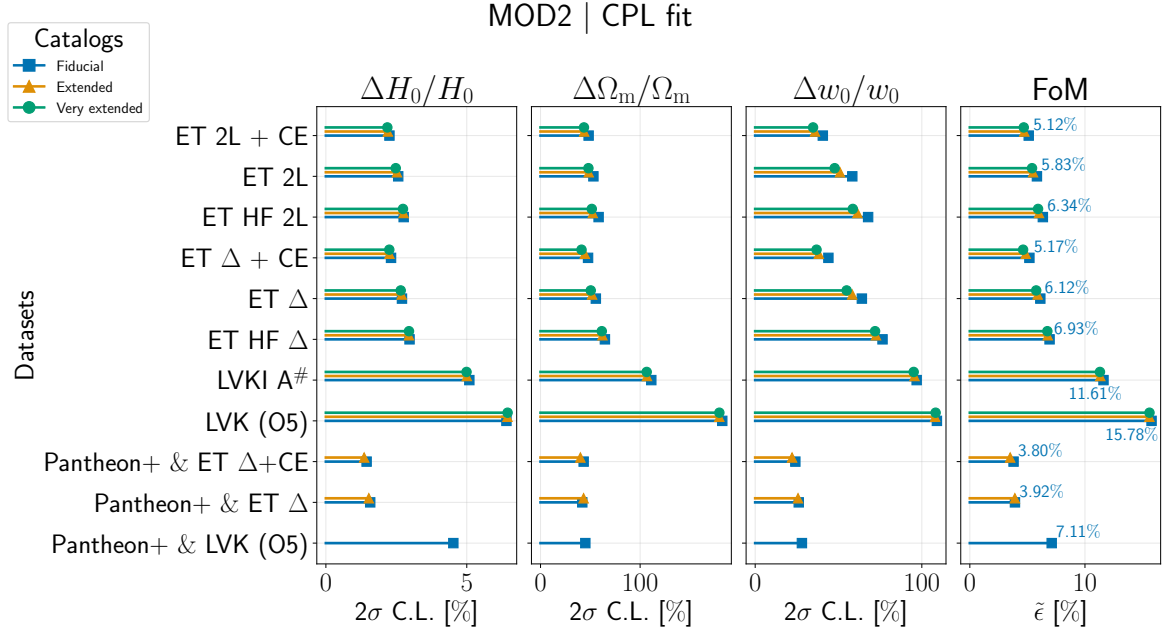


**Figure 28.** CPL  $2\sigma$  relative error on  $H_0$ ,  $\Omega_m$  and  $w_0$  for an underlying MOD2 cosmology. The last panel presents the relative FoM. The associated values can be found Table 7.

**Table 8.** MOD2 | GP fit

Data set	Fiducial			Extended		
	$\frac{\Delta H_0}{H_0}$	$\frac{\Delta \Omega_m}{\Omega_m}$	$\tilde{\epsilon}$	$\frac{\Delta H_0}{H_0}$	$\frac{\Delta \Omega_m}{\Omega_m}$	$\tilde{\epsilon}$
Pantheon+ & ETΔ	0.01	0.4	0.031	0.0095	0.4	0.03
Pantheon+ & ETΔ + CE	0.0088	0.37	0.028	0.0081	0.34	0.026
Pantheon+ & ET2L	0.0095	0.4	0.031	0.0088	0.4	0.028
Pantheon+ & ET2L + CE	0.0087	0.35	0.027	0.0078	0.35	0.025
ETΔ	0.015	0.55	0.045	0.014	0.5	0.04
ETΔ + CE	0.012	0.43	0.035	0.011	0.33	0.03
ET2L	0.014	0.5	0.041	0.013	0.45	0.036
ET2L + CE	0.012	0.45	0.037	0.0099	0.31	0.027

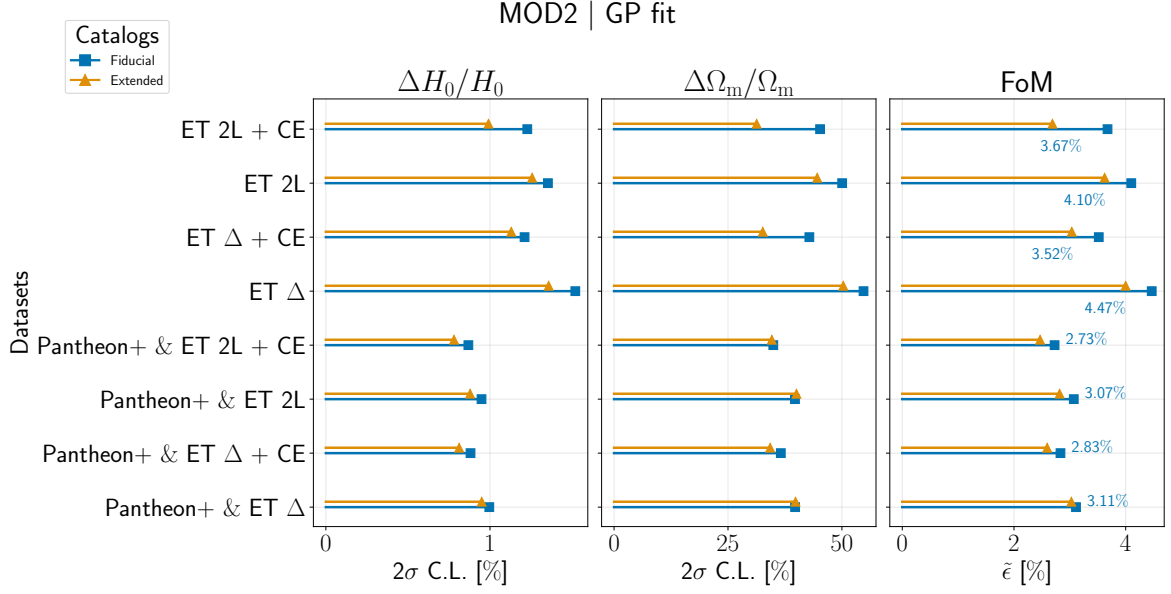


**Figure 29.** GP  $2\sigma$  relative error on  $H_0$  and  $\Omega_m$  for an underlying MOD2 cosmology. The last panel presents the relative FoM. The associated values can be found Table 8.

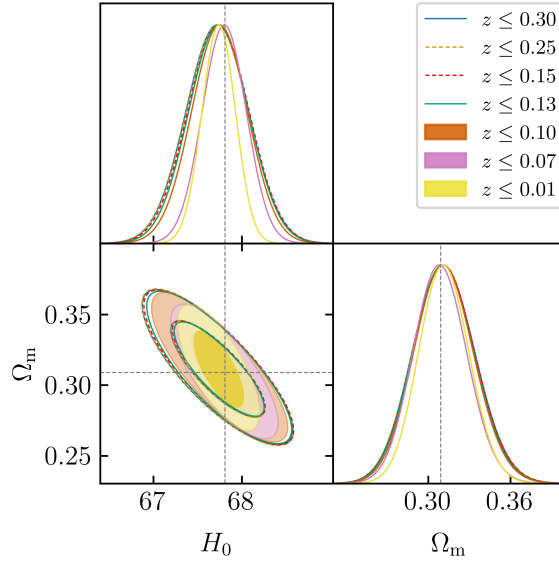


**Figure 30.** Comparison among different thresholds for the peculiar velocity analysis. These contours are all derived from fitting  $\Lambda$ CDM over the MOD1 fiducial data set using the ET $\Delta$ +CE configuration. The filled contours are obtained as follows: the first contour incorporates the correction for only the closest GRB, the second smallest contour includes corrections for the two closest GRBs, and the third contour accounts for the three closest GRBs. Observe that the constraints become stable when  $z > 0.15$ .

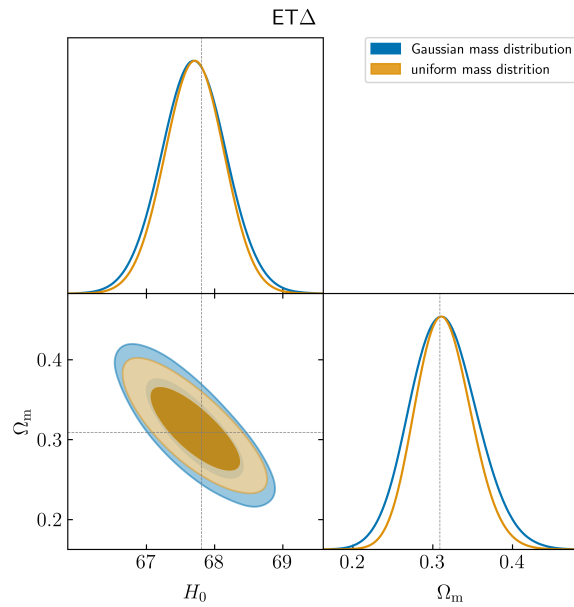


**Figure 31.** Comparison among different neutron star mass distributions. We show the case for ET $\Delta$  and the fiducial catalog. The uniform distribution refers to a catalog generated with  $\mathcal{U}(1.1, 2.1)M_{\odot}$ . The Gaussian distribution refer instead to a catalog generated drawing masses from a normal distribution  $\mathcal{N}(1.33, 0.09)M_{\odot}$ .

## References

- [1] SUPERNOVA COSMOLOGY PROJECT collaboration, S. Perlmutter et al., *Measurements of  $\Omega$  and  $\Lambda$  from 42 high redshift supernovae*, *Astrophys. J.* **517** (1999) 565–586, [[astro-ph/9812133](#)].
- [2] SUPERNOVA SEARCH TEAM collaboration, A. G. Riess et al., *Observational evidence from supernovae for an accelerating universe and a cosmological constant*, *Astron. J.* **116** (1998) 1009–1038, [[astro-ph/9805201](#)].
- [3] A. G. Riess et al., *Type Ia Supernova Distances at Redshift  $> 1.5$  from the Hubble Space Telescope Multi-cycle Treasury Programs: The Early Expansion Rate*, *Astrophys. J.* **853** (2018) 126, [[1710.00844](#)].
- [4] G. E. Addison, D. J. Watts, C. L. Bennett, M. Halpern, G. Hinshaw and J. L. Weiland, *Elucidating  $\Lambda$ CDM: Impact of Baryon Acoustic Oscillation Measurements on the Hubble Constant Discrepancy*, *Astrophys. J.* **853** (2018) 119, [[1707.06547](#)].
- [5] SDSS collaboration, D. J. Eisenstein et al., *Detection of the Baryon Acoustic Peak in the Large-Scale Correlation Function of SDSS Luminous Red Galaxies*, *Astrophys. J.* **633** (2005) 560–574, [[astro-ph/0501171](#)].
- [6] W. J. Percival, S. Cole, D. J. Eisenstein, R. C. Nichol, J. A. Peacock, A. C. Pope et al., *Measuring the Baryon Acoustic Oscillation scale using the SDSS and 2dFGRS*, *Mon. Not. Roy. Astron. Soc.* **381** (2007) 1053–1066, [[0705.3323](#)].
- [7] V. Poulin, T. L. Smith, R. Calderón and T. Simon, *On the implications of the ‘cosmic calibration tension’ beyond  $H_0$  and the synergy between early- and late-time new physics*, [2407.18292](#).
- [8] D. Camarena and V. Marra, *On the use of the local prior on the absolute magnitude of Type Ia supernovae in cosmological inference*, [2101.08641](#).
- [9] J. L. Bernal, L. Verde and A. G. Riess, *The trouble with  $H_0$* , *JCAP* **10** (2016) 019, [[1607.05617](#)].
- [10] PLANCK collaboration, N. Aghanim et al., *Planck 2018 results. VI. Cosmological parameters*, *Astron. Astrophys.* **641** (2020) A6, [[1807.06209](#)].
- [11] L. Knox and M. Millea, *Hubble constant hunter’s guide*, *Phys. Rev. D* **101** (2020) 043533, [[1908.03663](#)].
- [12] LIGO SCIENTIFIC, VIRGO collaboration, B. P. Abbott et al., *Observation of Gravitational Waves from a Binary Black Hole Merger*, *Phys. Rev. Lett.* **116** (2016) 061102, [[1602.03837](#)].
- [13] S. Mastrogiovanni, C. Karathanasis, J. Gair, G. Ashton, S. Rinaldi, H.-Y. Huang et al., *Cosmology with Gravitational Waves: A Review*, *Annalen Phys.* **536** (2024) 2200180.
- [14] B. Abbott et al., *GW170817: Observation of Gravitational Waves from a Binary Neutron Star Inspiral*, *Phys. Rev. Lett.* **119** (Oct, 2017) 161101.
- [15] B. F. Schutz, *Determining the Hubble constant from gravitational wave observations*, *Nature* **323** (Sept., 1986) 310–311.
- [16] S. Mastrogiovanni, K. Leyde, C. Karathanasis, E. Chassande-Mottin, D. A. Steer, J. Gair et al., *On the importance of source population models for gravitational-wave cosmology*, *Phys. Rev. D* **104** (2021) 062009, [[2103.14663](#)].
- [17] S. Mastrogiovanni, D. Laghi, R. Gray, G. C. Santoro, A. Ghosh, C. Karathanasis et al., *Joint population and cosmological properties inference with gravitational waves standard sirens and galaxy surveys*, *Phys. Rev. D* **108** (2023) 042002, [[2305.10488](#)].

- [18] LIGO SCIENTIFIC, VIRGO, 1M2H, DARK ENERGY CAMERA GW-E, DES, DLT40, LAS CUMBRES OBSERVATORY, VINROUGE, MASTER collaboration, B. P. Abbott et al., *A gravitational-wave standard siren measurement of the Hubble constant*, *Nature* **551** (2017) 85–88, [[1710.05835](#)].
- [19] G. Scelfo, M. Spinelli, A. Raccanelli, L. Boco, A. Lapi and M. Viel, *Gravitational waves  $\times$  HI intensity mapping: cosmological and astrophysical applications*, *JCAP* **01** (2022) 004, [[2106.09786](#)].
- [20] M. Moresco et al., *Unveiling the Universe with emerging cosmological probes*, *Living Rev. Rel.* **25** (2022) 6, [[2201.07241](#)].
- [21] R. Gray et al., *Joint cosmological and gravitational-wave population inference using dark sirens and galaxy catalogues*, *JCAP* **12** (2023) 023, [[2308.02281](#)].
- [22] H.-Y. Chen, M. Fishbach and D. E. Holz, *A two per cent Hubble constant measurement from standard sirens within five years*, *Nature* **562** (2018) 545–547, [[1712.06531](#)].
- [23] R. Gray et al., *Cosmological inference using gravitational wave standard sirens: A mock data analysis*, *Phys. Rev. D* **101** (2020) 122001, [[1908.06050](#)].
- [24] N. Muttoni, D. Laghi, N. Tamanini, S. Marsat and D. Izquierdo-Villalba, *Dark siren cosmology with binary black holes in the era of third-generation gravitational wave detectors*, *Phys. Rev. D* **108** (2023) 043543, [[2303.10693](#)].
- [25] G. Dályá, G. Galgóczi, L. Dobos, Z. Frei, I. S. Heng, R. Macas et al., *GLADE: A galaxy catalogue for multimessenger searches in the advanced gravitational-wave detector era*, *Mon. Not. Roy. Astron. Soc.* **479** (2018) 2374–2381, [[1804.05709](#)].
- [26] G. Dályá et al., *GLADE+ : an extended galaxy catalogue for multimessenger searches with advanced gravitational-wave detectors*, *Mon. Not. Roy. Astron. Soc.* **514** (2022) 1403–1411, [[2110.06184](#)].
- [27] LIGO SCIENTIFIC, VIRGO, VIRGO collaboration, B. P. Abbott et al., *A Gravitational-wave Measurement of the Hubble Constant Following the Second Observing Run of Advanced LIGO and Virgo*, *Astrophys. J.* **909** (2021) 218, [[1908.06060](#)].
- [28] A. Finke, S. Foffa, F. Iacovelli, M. Maggiore and M. Mancarella, *Cosmology with LIGO/Virgo dark sirens: Hubble parameter and modified gravitational wave propagation*, *JCAP* **08** (2021) 026, [[2101.12660](#)].
- [29] LIGO SCIENTIFIC, VIRGO, KAGRA collaboration, R. Abbott et al., *Constraints on the Cosmic Expansion History from GWTC–3*, *Astrophys. J.* **949** (2023) 76, [[2111.03604](#)].
- [30] DES, LIGO SCIENTIFIC, VIRGO collaboration, M. Soares-Santos et al., *First Measurement of the Hubble Constant from a Dark Standard Siren using the Dark Energy Survey Galaxies and the LIGO/Virgo Binary–Black-hole Merger GW170814*, *Astrophys. J. Lett.* **876** (2019) L7, [[1901.01540](#)].
- [31] DES collaboration, A. Palmese et al., *A statistical standard siren measurement of the Hubble constant from the LIGO/Virgo gravitational wave compact object merger GW190814 and Dark Energy Survey galaxies*, *Astrophys. J. Lett.* **900** (2020) L33, [[2006.14961](#)].
- [32] A. Palmese, C. R. Bom, S. Mucesh and W. G. Hartley, *A Standard Siren Measurement of the Hubble Constant Using Gravitational-wave Events from the First Three LIGO/Virgo Observing Runs and the DESI Legacy Survey*, *Astrophys. J.* **943** (2023) 56, [[2111.06445](#)].
- [33] V. Alfradique et al., *A dark siren measurement of the Hubble constant using gravitational wave events from the first three LIGO/Virgo observing runs and DELVE*, *Mon. Not. Roy. Astron. Soc.* **528** (2024) 3249–3259, [[2310.13695](#)].

- [34] DESI collaboration, W. Ballard et al., *A Dark Siren Measurement of the Hubble Constant with the LIGO/Virgo Gravitational Wave Event GW190412 and DESI Galaxies*, *Res. Notes AAS* **7** (2023) 250, [[2311.13062](#)].
- [35] J. M. Ezquiaga and D. E. Holz, *Spectral Sirens: Cosmology from the Full Mass Distribution of Compact Binaries*, *Phys. Rev. Lett.* **129** (2022) 061102, [[2202.08240](#)].
- [36] W. M. Farr, M. Fishbach, J. Ye and D. Holz, *A Future Percent-Level Measurement of the Hubble Expansion at Redshift 0.8 With Advanced LIGO*, *Astrophys. J. Lett.* **883** (2019) L42, [[1908.09084](#)].
- [37] S. Afroz and S. Mukherjee, *Prospect of Precision Cosmology and Testing General Relativity using Binary Black Holes- Galaxies Cross-correlation*, [2407.09262](#).
- [38] S. Mukherjee, A. Krolewski, B. D. Wandelt and J. Silk, *Cross-correlating dark sirens and galaxies: constraints on  $H_0$  from GWTC-3 of LIGO-Virgo-KAGRA*, [2203.03643](#).
- [39] C. C. Diaz and S. Mukherjee, *Mapping the cosmic expansion history from LIGO-Virgo-KAGRA in synergy with DESI and SPHEREx*, *Mon. Not. Roy. Astron. Soc.* **511** (2022) 2782–2795, [[2107.12787](#)].
- [40] S. Mukherjee, B. D. Wandelt, S. M. Nissanke and A. Silvestri, *Accurate precision Cosmology with redshift unknown gravitational wave sources*, *Phys. Rev. D* **103** (2021) 043520, [[2007.02943](#)].
- [41] A. Maselli, S. Marassi and M. Branchesi, *Binary white dwarfs and decihertz gravitational wave observations: From the Hubble constant to supernova astrophysics*, *Astron. Astrophys.* **635** (2020) A120, [[1910.00016](#)].
- [42] C. Yan, W. Zhao and Y. Lu, *On using inspiraling supermassive binary black holes in the pta frequency band as standard sirens to constrain dark energy*, *The Astrophysical Journal* **889** (2020) 79.
- [43] M. Bailes et al., *Gravitational-wave physics and astronomy in the 2020s and 2030s*, *Nature Rev. Phys.* **3** (2021) 344–366.
- [44] M. Branchesi et al., *Science with the Einstein Telescope: a comparison of different designs*, *JCAP* **07** (2023) 068, [[2303.15923](#)].
- [45] M. Evans et al., *A Horizon Study for Cosmic Explorer: Science, Observatories, and Community*, [2109.09882](#).
- [46] LGWA collaboration, J. Harms et al., *Lunar Gravitational-wave Antenna*, *Astrophys. J.* **910** (2021) 1, [[2010.13726](#)].
- [47] A. Cozzumbo, B. Mestichelli, M. Mirabile, L. Paiella, J. Tissino and J. Harms, *Opportunities and limits of lunar gravitational-wave detection*, [2309.15160](#).
- [48] LISA COSMOLOGY WORKING GROUP collaboration, P. Auclair et al., *Cosmology with the Laser Interferometer Space Antenna*, *Living Rev. Rel.* **26** (2023) 5, [[2204.05434](#)].
- [49] A. Sesana, A. Vecchio and M. Volonteri, *Gravitational waves from resolvable massive black hole binary systems and observations with Pulsar Timing Arrays*, *Mon. Not. Roy. Astron. Soc.* **394** (2009) 2255, [[0809.3412](#)].
- [50] Y. Wang and S. D. Mohanty, *Pulsar Timing Array Based Search for Supermassive Black Hole Binaries in the Square Kilometer Array Era*, *Phys. Rev. Lett.* **118** (2017) 151104, [[1611.09440](#)].
- [51] B. Abbott et al., *Gravitational waves and gamma-rays from a binary neutron star merger: Gw170817 and grb 170817a*, *Astrophys. J. Lett.* **848** (2017) L13, [[1710.05834](#)].

- [52] A. Goldstein et al., *An Ordinary Short Gamma-Ray Burst with Extraordinary Implications: Fermi-GBM Detection of GRB 170817A*, *Astrophys. J. Letters* **848** (Oct., 2017) L14, [[1710.05446](#)].
- [53] V. Savchenko et al., *INTEGRAL Detection of the First Prompt Gamma-Ray Signal Coincident with the Gravitational-wave Event GW170817*, *Astrophys. J. Letters* **848** (Oct., 2017) L15, [[1710.05449](#)].
- [54] S. Ascenzi, G. Oganesyan, M. Branchesi and R. Ciolfi, *Electromagnetic counterparts of compact binary mergers*, *J. Plasma Phys.* **87** (2021) 845870102, [[2011.04001](#)].
- [55] T. Piran, *The physics of gamma-ray bursts*, *Rev. Mod. Phys.* **76** (2004) 1143–1210, [[astro-ph/0405503](#)].
- [56] I. Bartos, P. Brady and S. Marka, *How Gravitational-wave Observations Can Shape the Gamma-ray Burst Paradigm*, *Class. Quant. Grav.* **30** (2013) 123001, [[1212.2289](#)].
- [57] R. Ciolfi, *Short gamma-ray burst central engines*, *Int. J. Mod. Phys. D* **27** (2018) 1842004, [[1804.03684](#)].
- [58] B. Paczynski, *Are gamma-ray bursts in star forming regions?*, *Astrophys. J. Lett.* **494** (1998) L45, [[astro-ph/9710086](#)].
- [59] J. S. Bloom, S. R. Kulkarni and S. G. Djorgovski, *The Observed offset distribution of gamma-ray bursts from their host galaxies: A Robust clue to the nature of the progenitors*, *Astron. J.* **123** (2002) 1111–1148, [[astro-ph/0010176](#)].
- [60] A. J. Levan et al., *A long-duration gamma-ray burst of dynamical origin from the nucleus of an ancient galaxy*, *Nature Astron.* **7** (2023) 976–985, [[2303.12912](#)].
- [61] J. C. Rastinejad et al., *A kilonova following a long-duration gamma-ray burst at 350 Mpc*, *Nature* **612** (2022) 223–227, [[2204.10864](#)].
- [62] A. Mei et al., *Gigaelectronvolt emission from a compact binary merger*, *Nature* **612** (2022) 236–239, [[2205.08566](#)].
- [63] H.-J. Lü et al., *GRB 211227A as a Peculiar Long Gamma-Ray Burst from a Compact Star Merger*, *Astrophys. J. Lett.* **931** (2022) L23, [[2201.06395](#)].
- [64] P. Nuessle, J. L. Racusin and N. E. White, *GRB Progenitor Classification from Gamma-Ray Burst Prompt and Afterglow Observations*, [[2407.08857](#)].
- [65] E. Troja et al., *A nearby long gamma-ray burst from a merger of compact objects*, *Nature* **612** (2022) 228–231, [[2209.03363](#)].
- [66] W.-f. Fong et al., *Short GRB Host Galaxies. I. Photometric and Spectroscopic Catalogs, Host Associations, and Galactocentric Offsets*, *Astrophys. J.* **940** (2022) 56, [[2206.01763](#)].
- [67] S. Ronchini, M. Branchesi, G. Oganesyan, B. Banerjee, U. Dupletsa, G. Ghirlanda et al., *Perspectives for multimessenger astronomy with the next generation of gravitational-wave detectors and high-energy satellites*, *Astron. Astrophys.* **665** (2022) A97, [[2204.01746](#)].
- [68] DESI collaboration, A. Aghamousa et al., *The DESI Experiment Part I: Science, Targeting, and Survey Design*, [[1611.00036](#)].
- [69] EUCLID collaboration, Y. Mellier et al., *Euclid. I. Overview of the Euclid mission*, [[2405.13491](#)].
- [70] J. Rigby, P. M. et al., *The science performance of just as characterized in commissioning*, *Publications of the Astronomical Society of the Pacific* **135** (apr, 2023) 048001.
- [71] R. Braun, A. Bonaldi, T. Bourke, E. Keane and J. Wagg, *Anticipated Performance of the Square Kilometre Array – Phase 1 (SKA1)*, [[1912.12699](#)].



- [72] E. Belgacem, Y. Dirian, S. Foffa, E. J. Howell, M. Maggiore and T. Regimbau, *Cosmology and dark energy from joint gravitational wave-GRB observations*, *JCAP* **08** (2019) 015, [[1907.01487](#)].
- [73] P. Bull et al., *Beyond  $\Lambda$ CDM: Problems, solutions, and the road ahead*, *Phys. Dark Univ.* **12** (2016) 56–99, [[1512.05356](#)].
- [74] L. Perivolaropoulos and F. Skara, *Challenges for  $\Lambda$ CDM: An update*, *New Astron. Rev.* **95** (2022) 101659, [[2105.05208](#)].
- [75] E. Di Valentino, O. Mena, S. Pan, L. Visinelli, W. Yang, A. Melchiorri et al., *In the realm of the Hubble tension—a review of solutions*, *Class. Quant. Grav.* **38** (2021) 153001, [[2103.01183](#)].
- [76] E. Abdalla et al., *Cosmology intertwined: A review of the particle physics, astrophysics, and cosmology associated with the cosmological tensions and anomalies*, *JHEAp* **34** (2022) 49–211, [[2203.06142](#)].
- [77] N. Schöneberg, G. Franco Abellán, A. Pérez Sánchez, S. J. Witte, V. Poulin and J. Lesgourgues, *The  $H_0$  Olympics: A fair ranking of proposed models*, *Phys. Rept.* **984** (2022) 1–55, [[2107.10291](#)].
- [78] A. R. Khalife, M. B. Zanjani, S. Galli, S. Günther, J. Lesgourgues and K. Benabed, *Review of Hubble tension solutions with new SH0ES and SPT-3G data*, [2312.09814](#).
- [79] L. Verde, N. Schöneberg and H. Gil-Marín, *A tale of many  $H_0$* , [2311.13305](#).
- [80] R. Calderón, B. L’Huillier, D. Polarski, A. Shafieloo and A. A. Starobinsky, *Joint reconstructions of growth and expansion histories from stage-IV surveys with minimal assumptions: Dark energy beyond  $\Lambda$* , *Phys. Rev. D* **106** (2022) 083513, [[2206.13820](#)].
- [81] J. Lesgourgues, *The Cosmic Linear Anisotropy Solving System (CLASS) I: Overview*, [1104.2932](#).
- [82] D. Blas, J. Lesgourgues and T. Tram, *The Cosmic Linear Anisotropy Solving System (CLASS) II: Approximation schemes*, *JCAP* **1107** (2011) 034, [[1104.2933](#)].
- [83] R. Calderón, B. L’Huillier, D. Polarski, A. Shafieloo and A. A. Starobinsky, *Joint reconstructions of growth and expansion histories from stage-IV surveys with minimal assumptions. II. Modified gravity and massive neutrinos*, *Phys. Rev. D* **108** (July, 2023) 023504, [[2301.00640](#)].
- [84] THESEUS collaboration, G. Stratta et al., *THESEUS: a key space mission concept for Multi-Messenger Astrophysics*, *Adv. Space Res.* **62** (2018) 662–682, [[1712.08153](#)].
- [85] X. Li and A. Shafieloo, *A Simple Phenomenological Emergent Dark Energy Model can Resolve the Hubble Tension*, *Astrophys. J. Lett.* **883** (2019) L3, [[1906.08275](#)].
- [86] X. Li and A. Shafieloo, *Evidence for Emergent Dark Energy*, *Astrophys. J.* **902** (2020) 58, [[2001.05103](#)].
- [87] DESI collaboration, A. G. Adame et al., *DESI 2024 VI: Cosmological Constraints from the Measurements of Baryon Acoustic Oscillations*, [2404.03002](#).
- [88] DESI collaboration, R. Calderon et al., *DESI 2024: Reconstructing Dark Energy using Crossing Statistics with DESI DR1 BAO data*, [2405.04216](#).
- [89] B. Audren, J. Lesgourgues, K. Benabed and S. Prunet, *Conservative Constraints on Early Cosmology: an illustration of the Monte Python cosmological parameter inference code*, *JCAP* **1302** (2013) 001, [[1210.7183](#)].
- [90] T. Brinckmann and J. Lesgourgues, *MontePython 3: boosted MCMC sampler and other features*, [1804.07261](#).

- [91] J. Torrado and A. Lewis, *Cobaya: Code for Bayesian Analysis of hierarchical physical models*, *JCAP* **05** (2021) 057, [2005.05290].
- [92] U. Dupletsa, J. Harms, K. K. Y. Ng, J. Tissino, F. Santoliquido and A. Cozzumbo, *Validating Prior-informed Fisher-matrix Analyses against GWTC Data*, [2404.16103](#).
- [93] JWST collaboration, A. J. Levan et al., *Heavy-element production in a compact object merger observed by JWST*, *Nature* **626** (2024) 737–741, [2307.02098].
- [94] D. Lazzati, R. Perna, B. P. Gompertz and A. J. Levan, *GRB 191019A: A Short Gamma-Ray Burst in Disguise from the Disk of an Active Galactic Nucleus*, *Astrophys. J. Lett.* **950** (2023) L20, [2303.12935].
- [95] E. Belgacem, Y. Dirian, S. Foffa and M. Maggiore, *Modified gravitational-wave propagation and standard sirens*, *Phys. Rev. D* **98** (2018) 023510, [1805.08731].
- [96] W. Zhao, C. Van Den Broeck, D. Baskaran and T. G. F. Li, *Determination of Dark Energy by the Einstein Telescope: Comparing with CMB, BAO and SNIa Observations*, *Phys. Rev. D* **83** (2011) 023005, [1009.0206].
- [97] T. M. Davis and M. I. Scrimgeour, *Deriving accurate peculiar velocities (even at high redshift)*, *Mon. Not. Roy. Astron. Soc.* **442** (2014) 1117–1122, [1405.0105].
- [98] H.-Y. Chen, J. M. Ezquiaga and I. Gupta, *Cosmography with next-generation gravitational wave detectors*, *Class. Quant. Grav.* **41** (2024) 125004, [2402.03120].
- [99] P. Mukherjee, R. Shah, A. Bhaumik and S. Pal, *Reconstructing the Hubble parameter with future Gravitational Wave missions using Machine Learning*, **3**, 2023.
- [100] G. Iorio et al., *Compact object mergers: exploring uncertainties from stellar and binary evolution with SEVN*, [2211.11774](#).
- [101] F. Santoliquido, M. Mapelli, N. Giacobbo, Y. Bouffanais and M. C. Artale, *The cosmic merger rate density of compact objects: impact of star formation, metallicity, initial mass function, and binary evolution*, *MNRAS* **502** (Apr., 2021) 4877–4889, [2009.03911].
- [102] THESEUS collaboration, L. Amati et al., *The THESEUS space mission: science goals, requirements and mission concept*, *Exper. Astron.* **52** (2021) 183–218, [2104.09531].
- [103] U. Dupletsa, J. Harms, B. Banerjee, M. Branchesi, B. Goncharov, A. Maselli et al., *gwfish: A simulation software to evaluate parameter-estimation capabilities of gravitational-wave detector networks*, *Astron. Comput.* **42** (2023) 100671, [2205.02499].
- [104] C. Kalaghatgi, M. Hannam and V. Raymond, *Parameter estimation with a spinning multimode waveform model*, *Phys. Rev. D* **101** (2020) 103004, [1909.10010].
- [105] LIGO SCIENTIFIC, VIRGO collaboration, R. Abbott et al., *GWTC-2: Compact Binary Coalescences Observed by LIGO and Virgo During the First Half of the Third Observing Run*, *Phys. Rev. X* **11** (2021) 021053, [2010.14527].
- [106] KAGRA, VIRGO, LIGO SCIENTIFIC collaboration, R. Abbott et al., *GWTC-3: Compact Binary Coalescences Observed by LIGO and Virgo during the Second Part of the Third Observing Run*, *Phys. Rev. X* **13** (2023) 041039, [2111.03606].
- [107] Y. Huang, H.-Y. Chen, C.-J. Haster, L. Sun, S. Vitale and J. Kissel, *Impact of calibration uncertainties on Hubble constant measurements from gravitational-wave sources*, [2204.03614](#).
- [108] S. Mukherjee, G. Lavaux, F. R. Bouchet, J. Jasche, B. D. Wandelt, S. M. Nissanke et al., *Velocity correction for Hubble constant measurements from standard sirens*, *Astron. Astrophys.* **646** (2021) A65, [1909.08627].
- [109] H. Nimonkar and S. Mukherjee, *Dependence of peculiar velocity on the host properties of the gravitational wave sources and its impact on the measurement of Hubble constant*, *Mon. Not. Roy. Astron. Soc.* **527** (2023) 2152–2164, [2307.05688].

- [110] C. M. Hirata, D. E. Holz and C. Cutler, *Reducing the weak lensing noise for the gravitational wave Hubble diagram using the non-Gaussianity of the magnification distribution*, *Phys. Rev. D* **81** (2010) 124046, [[1004.3988](#)].
- [111] N. Tamanini, C. Caprini, E. Barausse, A. Sesana, A. Klein and A. Petiteau, *Science with the space-based interferometer eLISA. III: probing the expansion of the universe using gravitational wave standard sirens*, *J. Cosmology Astropart. Phys.* **2016** (Apr., 2016) 002, [[1601.07112](#)].
- [112] G. Ashton et al., *BILBY: A user-friendly Bayesian inference library for gravitational-wave astronomy*, *Astrophys. J. Suppl.* **241** (2019) 27, [[1811.02042](#)].
- [113] LIGO SCIENTIFIC collaboration, J. Aasi et al., *Advanced LIGO*, *Class. Quant. Grav.* **32** (2015) 074001, [[1411.4547](#)].
- [114] VIRGO collaboration, F. Acernese et al., *Advanced Virgo: a second-generation interferometric gravitational wave detector*, *Class. Quant. Grav.* **32** (2015) 024001, [[1408.3978](#)].
- [115] KAGRA collaboration, T. Akutsu et al., *Overview of KAGRA: Detector design and construction history*, *PTEP* **2021** (2021) 05A101, [[2005.05574](#)].
- [116] B. P. Abbott, R. Abbott, T. D. Abbott, S. Abraham, F. Acernese, K. Ackley et al., *Prospects for observing and localizing gravitational-wave transients with Advanced LIGO, Advanced Virgo and KAGRA*, *Living Reviews in Relativity* **23** (Sept., 2020) 3.
- [117] P. Fritschel, K. Kuns, J. Driggers, A. Effler, B. Lantz, D. et al., *Report from the LSC Post-O5 Study Group*, *Tech. Rep. T2200287 (LIGO)* (2022) .
- [118] eBOSS collaboration, M. Blomqvist et al., *Baryon acoustic oscillations from the cross-correlation of Ly $\alpha$  absorption and quasars in eBOSS DR14*, *Astron. Astrophys.* **629** (2019) A86, [[1904.03430](#)].
- [119] D. Brout et al., *The Pantheon+ Analysis: Cosmological Constraints*, *Astrophys. J.* **938** (2022) 110, [[2202.04077](#)].
- [120] DESI collaboration, K. Lodha et al., *DESI 2024: Constraints on Physics-Focused Aspects of Dark Energy using DESI DR1 BAO Data*, [2405.13588](#).
- [121] T. Holsclaw, U. Alam, B. Sansó, H. Lee, K. Heitmann, S. Habib et al., *Nonparametric reconstruction of the dark energy equation of state*, *Phys. Rev. D* **82** (Nov., 2010) 103502, [[1009.5443](#)].
- [122] T. Holsclaw, U. Alam, B. Sansó, H. Lee, K. Heitmann, S. Habib et al., *Nonparametric dark energy reconstruction from supernova data*, *Phys. Rev. Lett.* **105** (Dec, 2010) 241302.
- [123] A. Shafieloo, A. G. Kim and E. V. Linder, *Gaussian Process Cosmography*, *Phys. Rev. D* **85** (2012) 123530, [[1204.2272](#)].
- [124] M. Seikel, C. Clarkson and M. Smith, *Reconstruction of dark energy and expansion dynamics using gaussian processes*, *Journal of Cosmology and Astroparticle Physics* **2012** (June, 2012) 036–036.
- [125] A. Shafieloo, A. G. Kim and E. V. Linder, *Model independent tests of cosmic growth versus expansion*, *Phys. Rev. D* **87** (Jan., 2013) 023520, [[1211.6128](#)].
- [126] R. E. Keeley, S. Joudaki, M. Kaplinghat and D. Kirkby, *Implications of a transition in the dark energy equation of state for the  $H_0$  and  $\sigma_8$  tensions*, *JCAP* **12** (2019) 035, [[1905.10198](#)].
- [127] S.-g. Hwang, B. L’Huillier, R. E. Keeley, M. J. Jee and A. Shafieloo, *How to use GP: effects of the mean function and hyperparameter selection on Gaussian process regression*, *JCAP* **02** (2023) 014, [[2206.15081](#)].

- [128] R. Calderón, A. Shafieloo, D. K. Hazra and W. Sohn, *On the consistency of  $\Lambda$ CDM with CMB measurements in light of the latest Planck, ACT and SPT data*, *JCAP* **08** (2023) 059, [[2302.14300](#)].
- [129] E. Belgacem, S. Foffa, M. Maggiore and T. Yang, *Gaussian processes reconstruction of modified gravitational wave propagation*, *Phys. Rev. D* **101** (2020) 063505, [[1911.11497](#)].
- [130] R. E. Keeley, A. Shafieloo, B. L’Huillier and E. V. Linder, *Debiasing Cosmic Gravitational Wave Sirens*, *Mon. Not. Roy. Astron. Soc.* **491** (2020) 3983–3989, [[1905.10216](#)].
- [131] Y.-J. Li, Y.-Z. Wang, M.-Z. Han, S.-P. Tang, Q. Yuan, Y.-Z. Fan et al., *A Flexible Gaussian Process Reconstruction Method and the Mass Function of the Coalescing Binary Black Hole Systems*, *Astrophys. J.* **917** (2021) 33, [[2104.02969](#)].
- [132] P. Mukherjee and A. Mukherjee, *Assessment of the cosmic distance duality relation using Gaussian process*, *Mon. Not. Roy. Astron. Soc.* **504** (2021) 3938–3946, [[2104.06066](#)].
- [133] G. Ashton, *Gaussian processes for glitch-robust gravitational-wave astronomy*, *Mon. Not. Roy. Astron. Soc.* **520** (2023) 2983–2994, [[2209.15547](#)].
- [134] C. Rasmussen and C. Williams, *Gaussian Processes for Machine Learning*. Adaptive computation and machine learning series. University Press Group Limited, 2006.
- [135] M. Chevallier and D. Polarski, *Accelerating universes with scaling dark matter*, *International Journal of Modern Physics D* **10** (Apr., 2001) 213–223.
- [136] E. V. Linder, *Exploring the expansion history of the universe*, *Phys. Rev. Lett.* **90** (2003) 091301, [[astro-ph/0208512](#)].
- [137] A. Gelman and D. B. Rubin, *Inference from iterative simulation using multiple sequences*, *Statist. Sci.* **7** (11, 1992) 457–472.
- [138] F. Beutler, C. Blake, M. Colless, D. H. Jones, L. Staveley-Smith, L. Campbell et al., *The 6dF Galaxy Survey: Baryon Acoustic Oscillations and the Local Hubble Constant*, *Mon. Not. Roy. Astron. Soc.* **416** (2011) 3017–3032, [[1106.3366](#)].
- [139] A. J. Ross, L. Samushia, C. Howlett, W. J. Percival, A. Burden and M. Manera, *The clustering of the SDSS DR7 main Galaxy sample – I. A 4 per cent distance measure at  $z = 0.15$* , *Mon. Not. Roy. Astron. Soc.* **449** (2015) 835–847, [[1409.3242](#)].
- [140] BOSS collaboration, S. Alam et al., *The clustering of galaxies in the completed SDSS-III Baryon Oscillation Spectroscopic Survey: cosmological analysis of the DR12 galaxy sample*, *Mon. Not. Roy. Astron. Soc.* **470** (2017) 2617–2652, [[1607.03155](#)].
- [141] V. de Sainte Agathe et al., *Baryon acoustic oscillations at  $z = 2.34$  from the correlations of Ly $\alpha$  absorption in eBOSS DR14*, *Astron. Astrophys.* **629** (2019) A85, [[1904.03400](#)].
- [142] M. Blomqvist et al., *Baryon acoustic oscillations from the cross-correlation of Ly $\alpha$  absorption and quasars in eBOSS DR14*, *Astron. Astrophys.* **629** (2019) A86, [[1904.03430](#)].
- [143] DESI collaboration, A. Aghamousa et al., *The DESI Experiment Part I: Science, Targeting, and Survey Design*, [1611.00036](#).
- [144] A. G. Riess, S. Casertano, W. Yuan, L. M. Macri and D. Scolnic, *Large Magellanic Cloud Cepheid Standards Provide a 1% Foundation for the Determination of the Hubble Constant and Stronger Evidence for Physics beyond  $\Lambda$ CDM*, [1903.07603](#).
- [145] A. Albrecht et al., *Report of the Dark Energy Task Force*, [astro-ph/0609591](#).
- [146] N. Borghi, M. Mancarella, M. Moresco, M. Tagliacruzchi, F. Iacovelli, A. Cimatti et al., *Cosmology and Astrophysics with Standard Sirens and Galaxy Catalogs in View of Future Gravitational Wave Observations*, *Astrophys. J.* **964** (2024) 191, [[2312.05302](#)].

- [147] M. Mancarella, N. Borghi, S. Foffa, E. Genoud-Prachex, F. Iacovelli, M. Maggiore et al., *Gravitational-wave cosmology with dark sirens: state of the art and perspectives for 3G detectors*, *PoS ICHEP2022* (11, 2022) 127, [2211.15512].
- [148] M. Mancarella, F. Iacovelli, S. Foffa, N. Muttoni and M. Maggiore, *Accurate standard siren cosmology with joint gravitational-wave and  $\gamma$ -ray burst observations*, 2405.02286.
- [149] E. Loffredo et al., *Prospects for kilonovae detections with the next-generation multimessenger observatories*, 2410.XXXXX (in prep.).
- [150] G. Ghirlanda et al., *HERMES: Gamma Ray Burst and Gravitational Wave counterpart hunter*, *Astron. Astrophys.* **689** (2024) A175, [2405.17630].
- [151] R. Ciolfi et al., *Multi-messenger astrophysics with THESEUS in the 2030s*, *Exper. Astron.* **52** (2021) 245–275, [2104.09534].
- [152] W. Yuan, C. Zhang, Y. Chen, S. Sun, Y. Zhang, W. Cui et al., *Einstein Probe: Exploring the ever-changing X-ray Universe*, *Scientia Sinica Physica, Mechanica & Astronomica* **48** (Mar., 2018) 039502.
- [153] N. E. White, F. E. Bauer, W. Baumgartner, M. Bautz, E. Berger, B. Cenko et al., *The Gamow Explorer: a Gamma-Ray Burst Observatory to study the high redshift universe and enable multi-messenger astrophysics*, in *UV, X-Ray, and Gamma-Ray Space Instrumentation for Astronomy XXII* (O. H. Siegmund, ed.), vol. 11821 of *Society of Photo-Optical Instrumentation Engineers (SPIE) Conference Series*, p. 1182109, Aug., 2021. 2111.06497. DOI.
- [154] K. Breivik, A. J. Connolly, K. E. S. Ford, M. Jurić, R. Mandelbaum, A. A. Miller et al., *From Data to Software to Science with the Rubin Observatory LSST*, *arXiv e-prints* (Aug., 2022) arXiv:2208.02781, [2208.02781].
- [155] J. Liske, *Status of the European Extremely Large Telescope*, in *Thirty Meter Telescope Science Forum* (M. Dickinson and H. Inami, eds.), p. 52, July, 2014.
- [156] A. Marconi, M. Abreu, V. Adibekyan, V. Alberti, S. Albrecht, J. Alcaniz et al., *ANDES, the high resolution spectrograph for the ELT: science case, baseline design and path to construction*, in *Ground-based and Airborne Instrumentation for Astronomy IX* (C. J. Evans, J. J. Bryant and K. Motohara, eds.), vol. 12184 of *Society of Photo-Optical Instrumentation Engineers (SPIE) Conference Series*, p. 1218424, Aug., 2022. DOI.
- [157] WST collaboration, R. Bacon et al., *WST - Widefield Spectroscopic Telescope: motivation, science drivers and top level requirements for a new dedicated facility*, *Proc. SPIE Int. Soc. Opt. Eng.* **13094** (2024) 130941O, [2405.12518].
- [158] A. Mitra and E. V. Linder, *Cosmology requirements on supernova photometric redshift systematics for the rubin lsst and roman space telescope*, *Physical Review D* **103** (Jan., 2021) .
- [159] LSST DARK ENERGY SCIENCE collaboration, A. Mitra, R. Kessler, S. More and R. Hlozek, *Using Host Galaxy Photometric Redshifts to Improve Cosmological Constraints with Type Ia Supernovae in the LSST Era*, *Astrophys. J.* **944** (2023) 212, [2210.07560].
- [160] Y. Wang et al., *The High Latitude Spectroscopic Survey on the Nancy Grace Roman Space Telescope*, *Astrophys. J.* **928** (2022) 1, [2110.01829].
- [161] A. Mitra, I. Gómez-Vargas and V. Zarikas, *From Simulations to Reality: Dark Energy Reconstruction with Simulated SNIa data from the Vera C. Rubin Observatory*, 2402.18124.
- [162] R. Essick and M. Fishbach, *Ensuring Consistency between Noise and Detection in Hierarchical Bayesian Inference*, *Astrophys. J.* **962** (2024) 169, [2310.02017].
- [163] J. D. Hunter, *Matplotlib: A 2d graphics environment*, *Computing in Science & Engineering* **9** (2007) 90–95.

- [164] C. R. Harris, K. J. Millman, S. J. van der Walt, R. Gommers, P. Virtanen, D. Cournapeau et al., *Array programming with NumPy*, *Nature* **585** (Sept., 2020) 357–362.
- [165] P. Virtanen, R. Gommers, T. E. Oliphant, M. Haberland, T. Reddy, D. Cournapeau et al., *SciPy 1.0: Fundamental Algorithms for Scientific Computing in Python*, *Nature Methods* **17** (2020) 261–272.
- [166] Astropy Collaboration, A. M. Price-Whelan, P. L. Lim, N. Earl, N. Starkman, L. Bradley et al., *The Astropy Project: Sustaining and Growing a Community-oriented Open-source Project and the Latest Major Release (v5.0) of the Core Package*, *ApJ* **935** (Aug., 2022) 167, [2206.14220].
- [167] B. Banerjee et al., *Pre-merger alert to detect prompt emission in very-high-energy gamma-rays from binary neutron star mergers: Einstein Telescope and Cherenkov Telescope Array synergy*, *Astron. Astrophys.* **678** (2023) A126, [2212.14007].
- [168] B. Abbott et al., *Multi-messenger observations of a binary neutron star merger*, *Astrophys. J. Lett.* **848** (2017) L12.
- [169] S. Ascenzi, G. Oganessian, O. S. Salafia, M. Branchesi, G. Ghirlanda and S. Dall’Osso, *High-latitude emission from the structured jet of  $\gamma$ -ray bursts observed off-axis*, *Astron. Astrophys.* **641** (2020) A61, [2004.12215].
- [170] E. Chassande-Mottin, K. Leyde, S. Mastrogiovanni and D. A. Steer, *Gravitational wave observations, distance measurement uncertainties, and cosmology*, *Phys. Rev. D* **100** (2019) 083514, [1906.02670].
- [171] S. A. Usman, J. C. Mills and S. Fairhurst, *Constraining the Inclinations of Binary Mergers from Gravitational-wave Observations*, *Astrophys. J.* **877** (2019) 82, [1809.10727].
- [172] H.-Y. Chen, C. Talbot and E. A. Chase, *Mitigating the Counterpart Selection Effect for Standard Sirens*, *Phys. Rev. Lett.* **132** (2024) 191003, [2307.10402].
- [173] M. Müller, S. Mukherjee and G. Ryan, *Be careful in multi-messenger inference of the Hubble constant: A path forward for robust inference*, **2406.11965**.
- [174] J. S. Bloom, S. R. Kulkarni and S. G. Djorgovski, *The Observed Offset Distribution of Gamma-Ray Bursts from Their Host Galaxies: A Robust Clue to the Nature of the Progenitors*, *AJ* **123** (Mar., 2002) 1111–1148, [astro-ph/0010176].
- [175] G. R. Ricker, J. L. Atteia, G. B. Crew, J. P. Doty, E. E. Fenimore, M. Galassi et al., *The High Energy Transient Explorer (HETE): Mission and Science Overview*, in *Gamma-Ray Burst and Afterglow Astronomy 2001: A Workshop Celebrating the First Year of the HETE Mission* (G. R. Ricker and R. K. Vanderspek, eds.), vol. 662 of *American Institute of Physics Conference Series*, pp. 3–16, Apr., 2003. DOI.
- [176] A. E. Nugent et al., *Short GRB Host Galaxies. II. A Legacy Sample of Redshifts, Stellar Population Properties, and Implications for Their Neutron Star Merger Origins*, *Astrophys. J.* **940** (2022) 57, [2206.01764].